Robert Hager

Radial propagation of geodesic acoustic modes

Analysis of magnetic geometry, nonlinear and non-Boussinesq properties of oscillating flows

TECHNISCHE UNIVERSITÄT MÜNCHEN
Max-Planck-Institut für Plasmaphysik

Radial propagation of geodesic acoustic modes

—

Analysis of magnetic geometry, nonlinear and non-Boussinesq properties of oscillating flows

Robert Christoph Hager

Vollständiger Abdruck der von der Fakultät für Physik
der Technischen Universität München
zur Erlangung des akademischen Grades eines
Doktors der Naturwissenschaften (Dr. rer. nat.)
genehmigten Dissertation.

Vorsitzender: Univ.-Prof. Dr. Lothar Oberauer
Prüfer der Dissertation:
1. Priv.-Doz. Dr. Klaus Hallatschek
2. Univ.-Prof. Dr. Harald Friedrich

Die Dissertation wurde am 13.01.2011 bei der Technischen Universität München eingereicht und durch die Fakultät für Physik am 05.10.2011 angenommen.

Abstract

One of the biggest problems of magnetic confinement fusion is the loss of heat and particles due to plasma micro-turbulence. Geodesic acoustic modes (GAMs), oscillating plasma flows, which are induced by radial gradients of the electrostatic potential, have the ability to control the turbulent transport.
The main subject of this thesis is the radial propagation of GAMs, which is crucial for the understanding of experimental GAM frequencies measured, for example, in the tokamaks ASDEX Upgrade and TEXTOR. The GAM group velocity is estimated from the ratio of the radial free energy flux of the GAM to its total free energy applying linearised two-fluid and gyrokinetic equations. This method is much more robust than approaches which calculate the group velocity directly and can be generalised to include additional physics, e.g. the influence of the X-point, which is out of reach of a direct analytical calculation of the dispersion relation. Since the individual terms of the energy-flux of the GAM can be explained by specific physical effects, deep insight into the propagation mechanisms is gained. Useful approximations for the radial GAM group velocity are derived for circular and elliptic flux-surfaces and for a simple single-null divertor model. The results are verified with numerical gyrokinetic and two-fluid computations.
The influence of the turbulence on the dispersion relation of GAMs is studied in numerical two-fluid studies. The nonlinear GAM dispersion can be much stronger than the linear dispersion implying that a GAM mode with one specific frequency can have a considerable radial mode width, which can be an explanation of the frequency plateaus observed in ASDEX Upgrade. The nonlinear driving term responsible for the modification of the GAM dispersion is identified and the correlation between the GAM dispersion and the position of reflection and absorption layers of the GAM is discussed.
The results of a comparative numerical study of turbulence generated GAMs applying the two-fluid code NLET and the gyrokinetic code GYRO is presented and good qualitative agreement is observed. The reasons for quantitative differences are discussed.
Linear GAM frequency spectra are calculated for experimental equilibrium data of NSTX and ASDEX Upgrade discharges obtained from equilibrium reconstruction routines like EFIT and Cliste. Very good agreement between the theoretical GAM frequencies computed with real ASDEX Upgrade equilibria and the corresponding experimental frequencies is observed. Earlier studies, which used Miller type equilibria to approximate the experimental configuration, deviated significantly from the experimental values.
Linear and nonlinear numerical two-fluid studies for NSTX show that the frequency of periodically appearing quiet periods with reduced turbulence intensity, which have been

observed in recent experiments, is of the order of the numerical GAM frequencies. Due to their ability to modulate the turbulent transport, GAMs could therefore account for the observed phenomenon. Moreover, a different mechanism leading to a modulation of the turbulent transport is identified, which is caused by a geometry induced preferential (turbulent) excitation of GAMs with negative radial wave numbers in conjunction with non-Boussinesq effects.

Contents

Chapter 1

Introduction

One of the biggest problems of magnetic confinement fusion is the turbulent transport of heat and particles out of the confinement region [1]. For an efficient fusion reactor, those energy losses have to be minimised to maximise the net output of electrical power. Zonal flows (ZFs) [2] and geodesic acoustic modes (GAMs) [3], stationary and oscillating plasma flows, respectively, which are induced by radial gradients of the electrostatic potential, are promising candidates for controlling the turbulent transport [4, 5, 6]. The basic mechanism is that the turbulent vortices are sheared and eventually torn apart between flux-surfaces with opposite flow velocities.

The key issue in the following chapters is the radial propagation of GAMs, which is crucial for the understanding of the experimentally observed GAM frequencies [7]. It provides an explanation for the frequency plateaus observed in ASDEX Upgrade. Another application is the excitation of GAMs through resonant magnetic perturbations in TEXTOR [8, 9].

The analysis starts by developing an elegant method to estimate the GAM group velocity v_g by constructing a Poynting theorem. It allows to estimate the group velocity even for asymmetric magnetic configurations like the single-null divertor geometry common in today's tokamaks, which is out of reach of a direct analytical calculation of the dispersion relation. Moreover, specific physical effects can be assigned to the individual terms in the energy-flux providing insight into the propagation mechanisms.

As evident from numerical turbulence studies, the turbulence can significantly alter the GAM frequency and can thus lead to a nonlinear GAM dispersion relation with a greatly enhanced radial group velocity. In realistic systems, in which the GAM dispersion and the turbulence properties depend on the radial position, high group velocities allow for GAM modes fulfilling $\omega_{GAM}(r, k_r) = \text{const.}$ [10] with a large radial extent. These modes may also be trapped radially between reflection and absorption layers and form eigenmodes with specific radial mode structures. Numerical non-Boussinesq turbulence studies are performed to investigate the nonlinear GAM dispersion relation and the resulting radial mode structures. The influence of turbulence and non-Boussinesq effects on the propagation of GAMs and the formation of eigenmodes may provide an explanation for the frequency plateaus observed in ASDEX Upgrade [7].

Since poloidal flows can couple to various sound waves in realistic magnetic configurations

– thus giving rise to more than one oscillating flow mode with the characteristics of a GAM – the GAM frequency spectra for several ASDEX Upgrade and NSTX discharges are calculated using experimental equilibrium data. Calculation of the GAM frequency using experimental geometries leads to better agreement between the GAM frequencies measured in ASDEX Upgrade and the numerical ones compared to earlier studies [11], which only approximated the experimental configuration using Miller equilibria [12]. Recent discharges in the spherical tokamak NSTX [13], displayed an oscillation of the turbulent heat transport at a frequency comparable to that of a GAM. Turbulence simulations and GAM spectra based on experimental equilibrium data are analysed to verify whether the observed phenomenon can be caused by GAMs.
The numerical turbulence studies presented in the following apply almost exclusively two-fluid theory, which does not cover collisionless effects like Landau damping. In order to demonstrate the qualitative agreement between the two-fluid code NLET [14] and the gyrokinetic code GYRO [15] in case of ZF and GAM studies, the transition from zonal flow activity in the plasma core to dominating GAM activity in the plasma edge is studied in numerical turbulence simulations.

1.1 Zonal flows and geodesic acoustic modes

Zonal flows and geodesic acoustic modes are collective plasma flows that are able to reduce the diffusion of energy due to turbulence [4]. This property makes them interesting for magnetic confinement research.
The term zonal flow originates from meteorology and oceanography, where the term zonal flow simply denotes large scale east-west flows of air or water along lines of constant latitude [16, 17, 18, 19]. An especially pronounced flow system is formed by the zonal winds in the atmosphere of Jupiter [20], which are visible as coloured rings.
In the context of magnetically confined plasmas the term zonal flow describes a plasma flow resulting from differences between the electrostatic potential on neighbouring flux-surfaces. The corresponding radial electric field $\mathbf{E}$ in conjunction with the magnetic field $\mathbf{B}$ leads to a rotation of the plasma in the direction of $\mathbf{E} \times \mathbf{B}$ (see Fig. 1.1 a)).
Commonly, such a flow is called zonal flow if it is stationary. However, if it periodically changes its direction, it is called geodesic acoustic mode. This name already conveys the mechanism causing the oscillatory nature of the GAM. Geodesic refers to the geodesic curvature of the magnetic field, that is the component of the curvature vector tangential to the flux-surface. The coupling of the GAM to sound waves is implied by the term acoustic. To clarify this connection, consider the curvature vector of a magnetic field line, which is defined by

$$\boldsymbol{\kappa} \equiv (\mathbf{b} \cdot \nabla)\, \mathbf{b} \tag{1.1}$$

with $\mathbf{b} \equiv \mathbf{B}/B$. The curvature of the equilibrium field can be transformed into [21]

$$\boldsymbol{\kappa} = \frac{1}{8\pi B^2} \nabla_\perp \left(8\pi p + B^2\right), \tag{1.2}$$

where $\nabla_\perp \equiv \nabla - \mathbf{b}(\mathbf{b} \cdot \nabla)$ is the component of the gradient perpendicular to B. From Eq. (1.2) it is evident that $\boldsymbol{\kappa}$ is always perpendicular to the magnetic field. Since ∇p

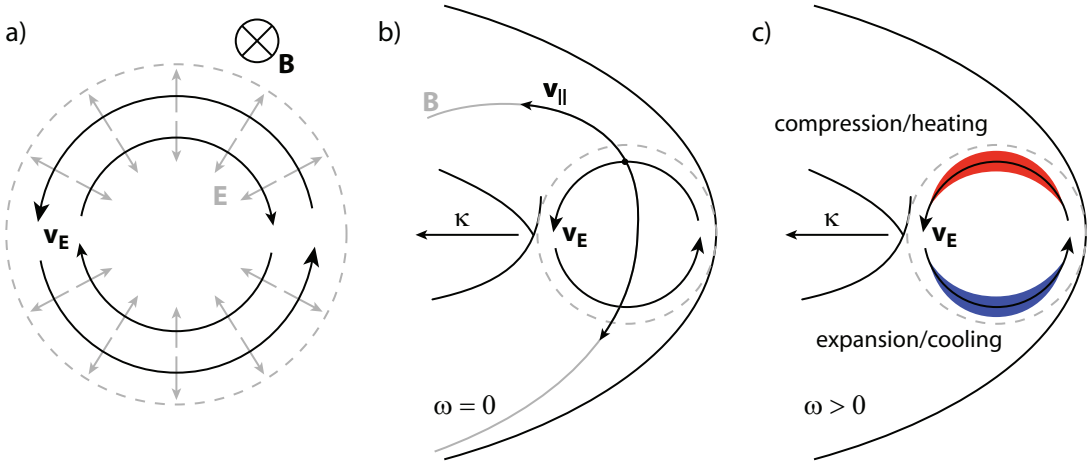

Figure 1.1: Schematic picture of poloidal $\mathbf{E} \times \mathbf{B}$-flows. a) Cross-section of torus with two zonal flow layers and the corresponding electric fields. b) Divergence of poloidal flow cancelled by parallel return-flow, therefore stationary ZF. c) Without return-flow up-down asymmetric pressure perturbations acting as restoring force, therefore oscillating ZF, i.e. GAM.

is perpendicular to the flux-surfaces, a geodesic component of the field line curvature can arise only due to the gradient of the magnetic field strength. Thus, if a geodesic component of $\nabla_\perp B^2$ exists, it is naturally parallel (or anti-parallel) to the zonal flows, i.e. $\boldsymbol{\kappa}_g \parallel \mathbf{E} \times \mathbf{B}$ with the geodesic curvature $\boldsymbol{\kappa}_g$. In order to close the line of argument, a result of ideal magnetohydrodynamic theory is applied. In an ideal plasma, the magnetic flux through any closed contour moving with the plasma is conserved (see [21, 22]). Thus, the cross section of a magnetic flux-tube moving in the direction of the geodesic curvature, i.e. to a region of higher field, is compressed and vice versa. If the plasma could not move parallel to $\mathbf{B}$, it would therefore be compressed in any case. However, the compression can be cancelled if the plasma can evade the compression of the flux-tube by a parallel flow. Consequently, in a system with geodesic curvature, a zonal flow is associated to a divergence of the corresponding density flux. If this divergence is compensated by a parallel flow, the flow is stationary, if not, a pressure perturbation arises, which absorbs the kinetic energy of the flow. Thus, the flow is braked, stopped and eventually reversed resulting in an oscillating flow. The geodesic acoustic mode was studied first by Winsor et al. [3] when analysing a magnetohydrodynamic (MHD) model for arbitrary toroidal field geometry. The GAM frequency was found to be proportional to $2^{1/2} c_s/R$, where $c_s \equiv ((T_i + T_e)/m_i)^{1/2}$ with the ion and electron temperatures T_i and T_e, the ion mass m_i, and the major radius R. Figure 1.1 illustrates the above discussion for a tokamak equilibrium with circular flux-surfaces. In Fig. 1.1 a) the radial electric field is shown with the resulting zonal flows. In the case under consideration, the curvature vector is mostly in negative major radial direction. Therefore, the divergence of the flow induced density flux is maximal at the top and the bottom of the device. In case of stationary zonal flows, the divergence is cancelled by an adequate return-flow parallel to the field lines as shown in Fig. 1.1 b). If the flow

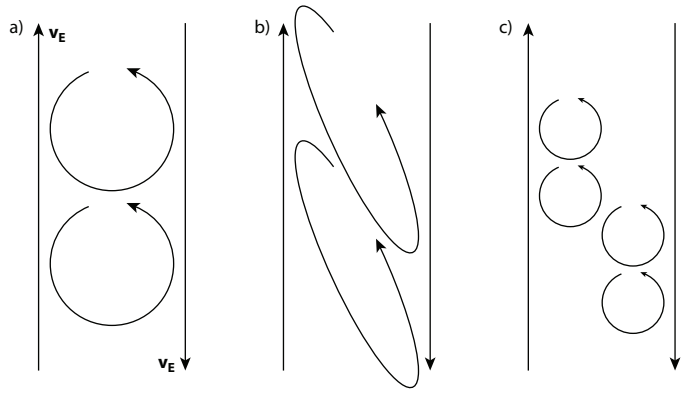

Figure 1.2: Turbulent vortices in a sheared $\mathbf{E} \times \mathbf{B}$-flow. a) Initial state. b) Turbulent eddies are distorted. c) When distorted by approximately their initial diameter, eddies break up into smaller vortices.

divergence is not cancelled by parallel flows, the flow oscillates according to the discussion above, i.e. a GAM arises (see Fig. 1.1 c)).
The fact that makes zonal flows and GAMs interesting for magnetic confinement research is their potential to reduce the turbulent diffusion of heat and particles. The basic idea of how zonal flows reduce the turbulence intensity is simple, the details can be found in Refs. [4, 5, 6, 23, 24, 25]. Imagine, as sketched in Fig. 1.2, a series of nested zonal flow layers with alternating flow direction and a turbulent vortex transporting heat and particles by moving perpendicular to the flux-surface. Let the initial diameter of the vortex be of the order of the minor radial extent of the flow layers. When moving across the flow layers, the vortex is sheared due to the variation of the flow velocity, the so-called shearing rate. Provided a large enough shearing rate, the flows tear the vortex apart into smaller scale vortices thereby absorbing part of the vortex's energy via the induced turbulent stress. Since the instability creating the turbulent eddies usually grows at a specific scale length, the reduction of the vortex scale length by sheared flows shifts the turbulence into a damped region of the wave number spectrum. Both effects lead to reduced anomalous transport.

1.2 Outline and motivation

Geodesic acoustic modes have been found experimentally in many tokamaks over the last few years, and therefore seem to be an ubiquitous phenomenon in tokamak edge plasmas at least in ohmic and L-mode discharges [26, 27, 28, 29, 30, 31, 32]. Hence, developing a detailed understanding of the properties of the GAM and its interaction with turbulence is not a merely academic challenge. The main subject of the following chapters is the radial propagation of the GAM (see e.g. [33, 34, 35]), which is important for several reasons. First, the group velocity contains information on the dispersion relation. In the calculation of the GAM frequency, finite Larmor radius effects are often neglected (e.g. in [11]) sometimes for convenience, sometimes due to the too high complexity of the considered situation (e.g.

magnetic geometry). Since, naturally, the scale length of GAMs in experiments is finite – typically ~ 1 cm (see above Refs.) – depending on the form of the dispersion relation, this can lead to significant discrepancies between experiment and theory. Second, due to their finite radial scale length, GAMs are influenced by the spatial variation of the plasma parameters, e.g. by the background temperature gradient, which can introduce reflection layers determining the radial mode structure of the GAM. This can, for example, lead to the formation of frequency plateaus as observed in ASDEX Upgrade [7]. According to Refs. [10, 33], for example, the radial mode structure of a GAM with $\omega_{GAM}(r, k_r) = \text{const.}$, i.e. whether the temperature gradient accelerates the GAM propagation towards the high or the low temperature region, depends on whether group and phase velocity have equal or opposite sign. In any case, the existence and properties of such eigenmodes strongly depend on the GAM dispersion. Therefore, GAM propagation is also an issue if one considers the excitation of GAMs by external antennas (see Refs. [8, 9]) in order to build up internal transport barriers.

The dispersion relation of the GAM mainly depends on two factors, the magnetic geometry and the turbulence. Most tokamak experiments run highly shaped plasma equilibria, often in divertor configurations, that deviate substantially from circular flux-surfaces at high aspect ratio which are often used in theory. This configuration is comfortable for numerical and analytical studies because it avoids the complexity of experimental equilibria while preserving the fundamental effects of toroidicity. However, since the properties and the excitation of GAMs and turbulence are closely related [36, 37, 38, 39] and both depend on the magnetic geometry, it is necessary, to develop an understanding of how the geometry can change the properties of the GAM and its impact on turbulent transport. The strong geometry dependence of the GAM frequency found by McKee et al. and Conway et al. [7, 40] and the problems in explaining theoretically from first principles the GAM frequencies found in experiments [11] underlines this necessity.

The aforementioned questions represent the starting point of this thesis. The basic methods and theories which are applied in the remainder of this work are reviewed in Chap. 2. Among those are gyrokinetic and two-fluid theory, calculation and modelling of plasma equilibria, and a basic explanation of micro-instability mechanisms.

The linear properties of GAM propagation are studied analytically and numerically in Chap. 3 applying linearised gyrokinetic and two-fluid theories. The results of this study have also been published in Refs. [41, 42]. Since the basic characteristics of the GAM such as its frequency and dispersion are determined by the geodesic curvature in the first place, starting with a set of linear differential equations and thus excluding turbulence is reasonable. A linear system allows for isolated treatment of GAMs and their geometry dependence.

The formal calculation of the GAM dispersion relation – as done for example in Refs. [33, 43, 44] – from which the radial group and phase velocity can be computed as $v_{g,r} = \partial_k \omega_{GAM}(k_r)$ and $v_{p,r} = \omega_{GAM}(k_r)/k_r$, respectively, tends to become very difficult for increasingly complex magnetic configurations. Therefore, an elegant way of computing the group velocity of the GAM via its free energy or Poynting flux is developed. A GAM can be constructed as a wave packet of the form $\int A(k_r) \exp(i(k_r r - \omega(k_r)t))\mathrm{d}k_r$ centered around a flux-surface. Since its energy is transported with its group velocity, it is possible

to compute the group velocity of the wave packet as the ratio of its energy-flux to its total energy. The Poynting flux is obtained by expressing the equation describing the time evolution of the total energy of the GAM as a continuity equation. Evaluating the energy-fluxes of the GAM applying two-fluid and gyrokinetic descriptions of the plasma, various contributions to the total energy-flux are identified. A detailed and vivid interpretation of the individual Poynting fluxes admits physical insights into the mechanisms of GAM propagation, which could be used for manipulation of the GAM group velocity by changing the magnetic geometry, and thus for influencing the global mode structure of the GAM.
Moreover, estimation of the GAM group velocity applying the energy approach is still feasible for complicated magnetic geometries. Predictions on the propagation behaviour of the GAM can be obtained with relatively little effort even for single-null divertor configurations. The advantages of the method are demonstrated by deriving estimates of the group velocity of the GAM for up-down symmetric elongated flux-surface shapes. Specific attention is paid to the effects of up-down asymmetry of the flux-surfaces, which is important in experiments using a divertor configuration. The possible symmetry breaking between inward and outward propagating GAMs may have implications for the L-H-transition in divertor configuration, where the L-H-power threshold depends on the position of the X-point [45].
The analytical calculations are verified with numerical studies applying the two-fluid code NLET [14], and the gyrokinetic codes GYRO [15] and GS2 [46]. These, furthermore, provide a complete linear spectrum including, besides the GAM dispersion, the sound wave spectrum and other modes, which may become resonant with the GAM and can thus limit the group velocity.
Gyrokinetic simulations tend to be computationally quite expensive in comparison to fluid simulations. Furthermore, because of the familiarity of its variables density, temperature and velocity, a fluid description is in many cases more intuitive than a gyrokinetic treatment. However, kinetic effects like trapped particles or Landau damping are not contained in a two-fluid description. Therefore, the gyrokinetic code GYRO and the two-fluid code NLET are benchmarked against each other for three different parameter sets, which represent the transition from core to edge parameters, in Chap. 4 in order to show that both codes produce equivalent results and to justify the almost exclusive use of two-fluid theory for the turbulence studies analysed in this thesis. Due to the strong Landau damping of the GAMs, stationary zonal flows are expected for core parameters. Since the effective mass of the ZFs increases towards the edge whereas Landau damping becomes significantly weaker, GAMs are expected to be dominant for edge parameters [11]. The central part of Chap. 4 is therefore given by the analysis of those turbulence studies intended to reproduce the transition from stationary zonal flows in the core plasma to geodesic acoustic modes in the edge.
Most numerical results of this thesis are obtained applying the Boussinesq approximation (the local limit), i.e. under the assumption that the background gradient scale length L_∇ is much larger than the turbulence scale length. This implies that the fluctuations of density, temperature etc. are much smaller than the corresponding background values, and that the properties of GAMs (like ω_{GAM}) and turbulence are constant over the computational domain. Since the local limit allows for significant simplifications of the governing

equations of motion, it is applied where the focus is on the pure parameter dependence of the phenomenon under consideration, for example the relation of the level of turbulent transport and GAM amplitude. If the influence of specific background density and temperature profiles, i.e. the variation of the plasma parameters, is of interest, the local limit has to be dropped. Non-local effects can become important when trying to match numerical studies and experiments. In this context, consider GAM measurements in ASDEX Upgrade. Conway et al. report radial frequency profiles displaying regions with constant GAM frequency in spite of the background temperature gradient, which are interrupted by regions in which the GAM frequency scales with $\sqrt{T}$ as expected (see Sec. 1.1) [7]. Itoh et al. in Ref. [10] describe a mode with constant frequency despite the variation of the local GAM frequency in terms of geodesic acoustic eigenmodes, whose radial structure depends on the GAM dispersion relation.

The latter, which is extensively discussed in Chap. 3, depends on the plasma parameters and the magnetic geometry. This dependence, however, can be influenced by the turbulence and therefore deviate from the linear predictions. Hence, the nonlinear GAM dispersion relation is studied numerically in Chap. 5. The radial mode structure of a GAM fulfilling the condition $\omega_{GAM}(r, k_r) = \text{const.}$ – this is called eigenmode in Ref. [10] – is discussed on the basis of a model dispersion relation. By deriving an expression for the wave front – a curve of constant phase – of such a global GAM, a method to measure the nonlinear GAM dispersion relation in non-Boussinesq turbulence simulations by fitting the numerical wave front to the analytical prediction is developed.

The propagation of GAMs in non-Boussinesq NLET simulations, in which the local GAM frequency varies significantly between the inner and outer radial boundary, is studied first in the linear case. Finally, the method for measuring the nonlinear GAM dispersion is demonstrated for an NLET turbulence simulation, in which the observed GAM frequencies $\omega_{GAM}(r, k_r)$ exceed their local values $\omega_{GAM,0}(r)$ by up to 30 % suggesting a much stronger dispersion and much higher group velocities than in linear calculations. By splitting the nonlinear terms which drive the GAMs into terms acting as energy source and terms shifting the phase of the GAM oscillation, the drive mechanism responsible for the modification of the GAM dispersion relation can be identified. The nonlinear dispersion relations of two GAM studies discussed in Chap. 4 are also measured and give hints on a possible parameter dependence of the propagation direction of the GAM.

In Chap. 6, experimental geometries of the National Spherical Torus Experiment (NSTX) and ASDEX Upgrade (AUG) obtained by equilibrium reconstruction routines are analysed according to their GAM properties. In ASDEX Upgrade GAMs have been found in numerous ohmic and L-mode discharges [47]. Therefore, the analysis of the AUG equilibria is focused in the first place on finding a theoretical explanation of the features observed experimentally. The theoretical GAM frequencies in an earlier study [11], computed using Miller-type equilibria [12], deviated from the values found experimentally by a factor of up to two. In order to achieve better agreement, the GAM frequencies are calculated with experimental equilibrium data. Besides the the frequency comparison, the radial regions in which GAMs can be observed in experiment are discussed. In divertor discharges with a pronounced edge density and temperature pedestal, GAMs are measured only in a narrow radial region in the plasma edge whereas GAMs are excited until further inside the plasma

in limiter discharges with less pronounced pedestals [7, 48]. This question is approached using NLET turbulence calculations, and possible relations to the plasma parameters are discussed.
The analysis of NSTX equilibria is based on recent observations made using a gas puff imaging (GPI) diagnostic [13]. Shortly before the L-H-transition, a quasi-periodic oscillation of the GPI-intensity in the scrape-of-layer (SOL) at approximately 3 kHz was detected, which was interpreted as a periodic suppression of turbulence. The oscillation of the GPI-intensity was accompanied by an oscillation of the poloidal velocity. In total these observations suggest to further investigate, whether the oscillation can be attributed to a geodesic acoustic mode. In a first approach, the GAM frequency is calculated from linearised two-fluid equations using experimental equilibrium data and temperature profiles. Such an analysis is necessary since in realistic geometries and especially in rather extreme configurations like spherical tokamaks, there may be more than one mode showing distinct characteristics of a GAM. Which one of these GAM candidates is eventually excited depends on the turbulence. Moreover, another mechanism is discussed, which can cause the turbulent heat-flux to oscillate at the GAM frequency. Instead of directly modulating the turbulence intensity, GAMs could also influence the turbulence indirectly via their radial scale length (i.e. their shearing rate), which may depend on the magnetic geometry and can fluctuate in time in non-Boussinesq turbulence studies.
Finally, a summary of the results presented in this thesis is given in Chap. 7.

Chapter 2

Methods

In the following, the fundamental theories and concepts used throughout this thesis, are reviewed in a concise way. Since most of the topics addressed here are discussed in more detail in standard text books, this chapter shall serve as a reminder or a short reference. Since the influence of the geometry of the magnetic field on geodesic acoustic modes an important issue of this thesis, Sec. 2.1 is dedicated to the theoretical description of plasma equilibria in axisymmetric magnetic confinement devices like tokamaks, i.e. the calculation of the equilibrium magnetic field. Section 2.2, which gives a short introduction to the gyrokinetic and two-fluid description of plasma dynamics, depends on Sec. 2.1 insofar as the differential operators appearing in the equations of motion are determined by the magnetic geometry. The mechanisms that lead to the growth of small perturbations of the equilibrium and to turbulence with the corresponding radial particle and energy transport are discussed in Section 2.3. Finally, the calculation of the geodesic acoustic mode frequency for zero minor radial wavenumber is discussed exemplarily for a geometrically simple two-fluid system. The generalisation to arbitrary magnetic geometry is straightforward.

2.1 Plasma equilibrium

The first step in describing a magnetically confined plasma is equilibrium analysis. Equilibrium theory aims at finding a stationary state in which the plasma is confined by the magnetic field. Therefore, equilibrium analysis is time-independent. Its basic condition expresses the force balance between pressure and Lorentz forces:

$$c\nabla p = \mathbf{j} \times \mathbf{B}. \tag{2.1}$$

From Eq. (2.1) it is immediately clear that the magnetic field is perpendicular to the pressure gradient everywhere, and that the magnetic field lines lie on surfaces of constant pressure. Of course Eq. (2.1) also allows field line chaos, but for the derivation of a stationary equilibrium, it is assumed that pressure and magnetic field are well behaved such that the confinement volume is filled with nested isobars which are densely covered by a magnetic field line, i.e. one assumes the existence of flux-surfaces. This assumption already simplifies the problem significantly. In addition, the flux-surfaces are assumed to

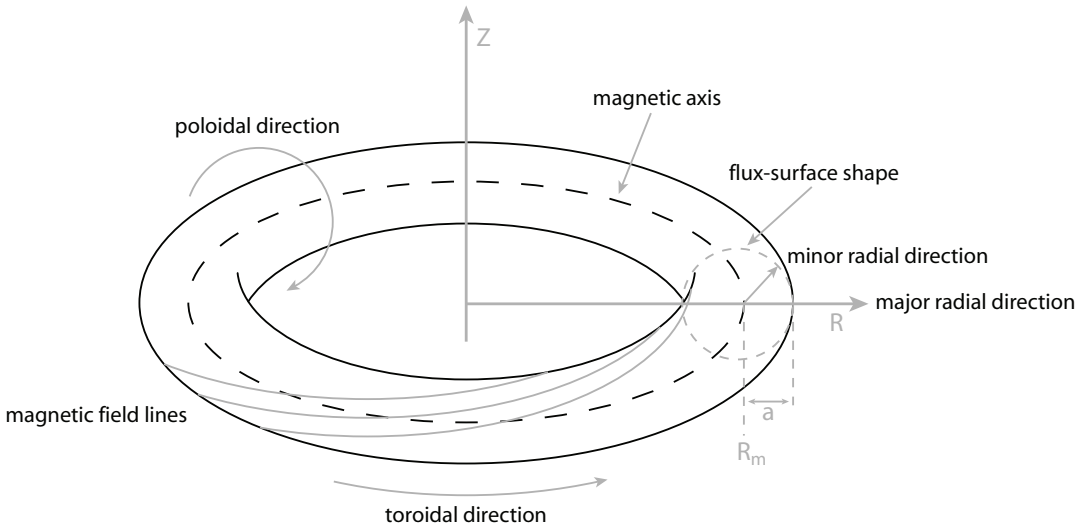

Figure 2.1: Schematic drawing of the magnetic field configuration of a tokamak.

be axisymmetric because only tokamak equilibria – a schematic of a tokamak equilibrium is shown in Fig. 2.1 – are considered in this thesis.
In the following, a more convenient and frequently used form of the equilibrium condition exploiting the benefits of axisymmetry – the Grad-Shafranov equation – will be derived, and a strategy to compute local approximate solutions of this equation will be explained. For detailed discussions of those two topics the reader is referred to Refs. [12] and [21].

2.1.1 Symmetry coordinates

Assuming the existence of axisymmetric flux-surfaces allows for the use of a very convenient set of coordinates, namely symmetry coordinates, which are a special case of magnetic flux coordinates. The name "flux-surface" stems from the fact that the magnetic flux enclosed by the flux-surface is constant on the surface. The toroidal and poloidal magnetic fluxes are defined by

$$\Psi_T \equiv \int_{S_T} \mathrm{d}S\mathbf{n}\cdot\mathbf{B}, \quad \Psi_P \equiv \int_{S_P} \mathrm{d}S\mathbf{n}\cdot\mathbf{B}, \tag{2.2}$$

where $\mathbf{n}$ is the unit normal from the surfaces S_T and S_P, which are indicated in Fig. 2.2. Functions f fulfilling $\mathbf{B}\cdot\nabla f = 0$ are called flux labels. It is therefore natural to choose a flux label as radial coordinate r, since it uniquely labels a flux surface. To make the set of coordinates complete, two angle variables are to be specified. In order to make use of axisymmetry, the toroidal angle ζ is defined as the negative cylindrical azimuthal angle, $\zeta \equiv -\phi$ (ζ clockwise with respect to the Z-axis). Axisymmetry implies

$$\frac{\partial\mathbf{B}}{\partial\zeta} = 0. \tag{2.3}$$

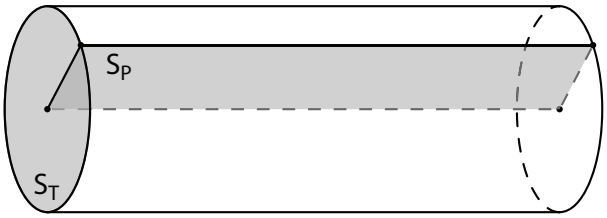

Figure 2.2: Integration surfaces for the calculation of the poloidal and toroidal magnetic fluxes Ψ_P and Ψ_T – for the sake of clarity – in cylindrical geometry.

The poloidal angle coordinate θ can then be chosen such that the magnetic field can be written in terms of flux labels and the covariant basis vector $\nabla\zeta$ [21],

$$\mathbf{B} = I(r)\nabla\zeta + \nabla\zeta \times \nabla\chi, \tag{2.4}$$

where the covariant ζ-component of $\mathbf{B}$, $B_\zeta \equiv I(r)$ is a flux label and $\chi \equiv \Psi_P/2\pi$. The coordinate set (r, θ, ζ) with the corresponding covariant basis vectors ∇r, $\nabla\theta$, and $\nabla\zeta$ is partially orthogonal,

$$\nabla\zeta \cdot \nabla r = 0 = \nabla\zeta \cdot \nabla\theta. \tag{2.5}$$

The metric tensor simplifies to

$$g_{ij} = \begin{pmatrix} g_{rr} & g_{r\theta} & 0 \\ g_{r\theta} & g_{\theta\theta} & 0 \\ 0 & 0 & R^2 \end{pmatrix}, \tag{2.6}$$

where R is the usual cylindrical radius. Thus, $\left|\nabla\zeta\right| = (g^{\zeta\zeta})^{1/2} = 1/R$. The determinant of the metric tensor is given by

$$\sqrt{g} \equiv \sqrt{\det\left(g_{ij}\right)} = q\frac{\partial\chi}{\partial r}\frac{R^2}{I(r)}. \tag{2.7}$$

For the poloidal and toroidal magnetic field follows

$$\begin{aligned} \left|\mathbf{B}_P\right| &= \left|\nabla\zeta \times \nabla\chi\right| = \frac{\left|\nabla\chi\right|}{R}, \\ \left|\mathbf{B}_T\right| &= \left|I(r)\nabla\zeta\right| = \frac{I(r)}{R}. \end{aligned} \tag{2.8}$$

2.1.2 Grad-Shafranov equation

The coordinates defined in the previous section simplify the derivation of the Grad-Shafranov equation, which is a special form of the equilibrium condition (2.1) for axisymmetric systems. In addition, further conventions are specified for convenience. Partial derivatives with respect to the radial coordinate are denoted by $f' \equiv \partial f/\partial r$. Any vector $\mathbf{V}$ can be constructed as the sum of a vector parallel and a vector perpendicular to the magnetic field $\mathbf{B}$:

$$\mathbf{V} = \mathbf{V}_\parallel + \mathbf{V}_\perp. \tag{2.9}$$

With $\mathbf{b} \equiv \mathbf{B}/B$, the parallel and perpendicular parts of $\mathbf{V}$ can be written as

$$\mathbf{V}_{\parallel} = \mathbf{b}\,(\mathbf{b}\cdot\mathbf{V})\,, \quad \mathbf{V}_{\perp} = (\mathbb{I} - \mathbf{bb})\cdot\mathbf{V}_{\perp}. \tag{2.10}$$

Thus, Eq. (2.1) yields an expression for the diamagnetic current $\mathbf{j}_{\perp}$:

$$\mathbf{j}_{\perp} = \frac{c}{B}\mathbf{b}\times\nabla p. \tag{2.11}$$

Therefore, the contravariant radial component of the current, $j^r = \mathbf{j}\cdot\nabla r = \mathbf{j}_{\perp}\cdot\nabla r$ vanishes, which in conjunction with the contravariant radial component of Ampère's law $(4\pi/c)\mathbf{j} = \nabla\times\mathbf{B}$ and axisymmetry implies that B_ζ is indeed a flux label.
Since $B^r = 0 = j^r$, only the radial component of the equilibrium condition (2.1) has to be considered:

$$\sqrt{g}\left(j^\theta B^\zeta - j^\zeta B^\theta\right) = cp'. \tag{2.12}$$

The components of the plasma current can be eliminated from Eq. (2.12) applying Ampère's law. Its radial component has been used to prove that $B_\zeta = I$ is a flux label. The remaining two components determine j^θ and j^ζ:

$$\begin{aligned} j^\theta &= \nabla\theta\cdot(\nabla\times\mathbf{B})\,,\\ j^\zeta &= \nabla\zeta\cdot(\nabla\times\mathbf{B})\,. \end{aligned} \tag{2.13}$$

Using the identity $\nabla\xi\cdot(\nabla\times\mathbf{A}) = \nabla\cdot(\mathbf{A}\times\nabla\xi)$ for any ξ, one finds

$$\begin{aligned} j^\theta &= -\frac{c}{4\pi}\frac{II'}{q\chi' R^2},\\ j^\zeta &= \frac{c}{4\pi}\nabla\cdot\left(R^{-2}\nabla\chi\right). \end{aligned} \tag{2.14}$$

Thus, after substitution of the currents, the equilibrium condition becomes

$$R^2\nabla\cdot\left(R^{-2}\nabla\chi\right)\chi' = -II' - 4\pi R^2 p', \tag{2.15}$$

which is called Grad-Shafranov equation. Choosing $r \equiv \chi$ implies $f' = \partial f/\partial\chi$ and $\chi' = 1$.

2.1.3 Mercier-Luc formalism and Miller geometry

The Grad-Shafranov equation (2.15) is a second order partial differential equation for the flux label $\chi = \Psi_P/2\pi$. It can in principle be solved when the right-hand-side is known, i.e. I and I', which determine the toroidal field profile and the poloidal current, and the pressure gradient p' (in this section $f' = \partial f/\partial\chi$). However, finding a solution can be challenging, especially if one wants to reconstruct an experimental equilibrium from the limited information available from the diagnostics.
In numerical studies the problem can be simplified significantly by using the local limit. When the radial extent of the simulation domain is small compared to the system size, the solution of the Grad-Shafranov equation has to be computed only for a narrow region around one flux surface. A convenient way of obtaining such a local solution [12] is to

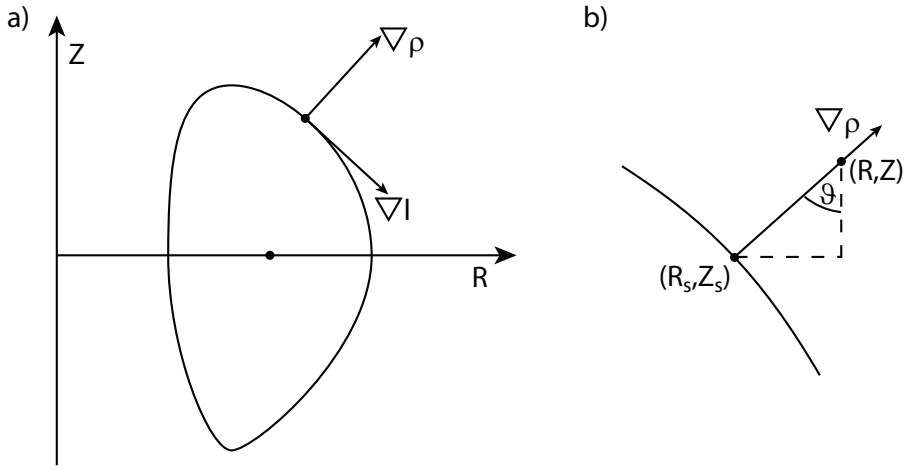

Figure 2.3: a) Flux surface in the poloidal plane with corresponding basis vectors $\nabla\rho$ and ∇l. b) Representation of an arbitrary point (R, Z) in the poloidal plane with the Mercier-Luc coordinates ρ and l, and the angle ϑ.

specify first the solution on a flux-surface $\chi = \chi_0$, which can be done by defining the shape of the flux-surface, $R_s(l)$ and $Z_s(l)$, the poloidal magnetic field $B_{Ps}(l)$, the pressure gradient $p'(\chi_0)$, $I(\chi_0)$, and $I'(\chi_0)$. Here, R and Z are cylindrical coordinates, l is the poloidal arc length, the magnetic field is given by Eq. (2.4) and the field strength of the poloidal and toroidal fields by Eq. (2.8). Based on the specified flux-surface shape, one can then define the set of coordinates (ρ, l, ζ), where ρ is the the distance normal to the flux-surface (R_s, Z_s), and expand χ in terms of ρ. The corresponding basis vectors are illustrated in Fig. 2.3 a). With the specified information one can compute an approximate solution of the Grad-Shafranov equation correct to first order in ρ.
In terms of the coordinates defined above, each point (R, Z) in the poloidal plane can be written as

$$\begin{aligned} R &= R_s(l) + \rho\sin(\vartheta(l)), \\ Z &= Z_s(l) + \rho\cos(\vartheta(l)), \end{aligned} \tag{2.16}$$

where the angle ϑ is the angle between the Z-axis and $\nabla\rho$ (Fig. 2.3 b). Thus, it follows immediately that

$$\begin{aligned} \frac{\partial R_s}{\partial\vartheta} &= \cos(\vartheta), \\ \frac{\partial Z_s}{\partial\vartheta} &= -\sin(\vartheta), \\ \frac{1}{R_c(l)} &= \left|\frac{\partial_l R_s \partial_l^2 Z_s - \partial_l^2 R_s \partial_l Z_s}{((\partial_l R_s)^2 + (\partial_l Z_s)^2)^{3/2}}\right| = \frac{\mathrm{d}\vartheta}{\mathrm{d}l} \end{aligned} \tag{2.17}$$

with the radius of local curvature of the flux-surface shape R_c. The calculation of the metric coefficients and the Grad-Shafranov operator $R\nabla\cdot(R^{-2}\nabla)$ can be found in App. A.

With the expansion $\chi = \chi_0 + \rho\chi_1(l) + \rho^2\chi_2(l) + \dots$ one finds by evaluating $B_{Ps} = \left|\nabla\zeta \times \nabla\chi\right|$ that

$$\chi_1(l) = R_s(l) B_{Ps}(l). \tag{2.18}$$

The second order term χ_2 is obtained from the Grad-Shafranov equation

$$R^2\left(R^{-2}\nabla\chi\right) = \frac{R^2}{\sqrt{g}}\left[\frac{\partial}{\partial\rho}\left(\frac{\sqrt{g}}{R^2}g^{\rho\rho}\frac{\partial\chi}{\partial\rho}\right) + \frac{\partial}{\partial l}\left(\frac{\sqrt{g}}{R^2}g^{ll}\frac{\partial\chi}{\partial l}\right)\right] = -R^2 p'(\chi_0) - II'(\chi_0). \tag{2.19}$$

Substituting the expansion of χ and the metric coefficients (A.3), one finds

$$\chi_2(l) = \frac{1}{2}\left[\left(\frac{R_s(l)}{R_c(l)} + \sin(\vartheta(l))\right) B_{Ps}(l) - II' - R_s(l)^2 p'\right]. \tag{2.20}$$

What remains to be computed now are the safety factor $q(\chi_0)$ and the global shear $s_g(\chi_0) \equiv \partial q/\partial\chi(\chi_0)$. The local field line pitch is given by the ratio of the toroidal to the poloidal arc length $\mathrm{d}l_\zeta/\mathrm{d}l_p = B_T/B_P$. Therefore, the safety factor is given by

$$q(\chi) = \frac{1}{2\pi}\oint \mathrm{d}\zeta = \frac{I(\chi)}{2\pi}\oint \frac{\mathrm{d}l_p}{R^2 B_P}. \tag{2.21}$$

For $q(\chi_0)$ the leading order of Eq. (2.21) is sufficient whereas the first order in ρ yields the global shear. The latter requires the first order expressions of $1/R^2$, $1/B_P$ and $\mathrm{d}l_p$, which are

$$\begin{aligned}
\frac{1}{R^2} &= \frac{1}{R_s^2}\left(1 - \frac{2\rho}{R_c}\sin(\vartheta)\right), \\
\frac{1}{B_P} &= \frac{1}{B_{Ps}}\left[1 - \rho\left(\frac{1}{R_c} - \frac{R_s p'}{B_{Ps}} - \frac{II'}{R_s B_{Ps}}\right)\right], \\
\mathrm{d}l_p &= \left(1 - \frac{\rho}{R_c}\right)\mathrm{d}l.
\end{aligned} \tag{2.22}$$

Eventually, the safety factor and global shear are given by

$$q(\chi_0) = \frac{I(\chi_0)}{2\pi}\oint \frac{\mathrm{d}l}{R_s B_{Ps}} = \frac{I(\chi_0)}{2\pi(\partial\chi/\partial\rho)}\oint \frac{\mathrm{d}l}{R_s\left|\nabla\rho\right|}, \tag{2.23}$$

and

$$\begin{aligned}
s_g(\chi_0) \equiv \frac{\partial q}{\partial\chi}(\chi_0) = \frac{I'(\chi_0)}{I(\chi_0)} q(\chi_0) \\
+ \frac{I(\chi_0)}{2\pi}\oint \frac{\mathrm{d}l}{R_s^3 B_{Ps}^2}\left(-\frac{2}{R_c} - \frac{2\sin(\vartheta)}{R_s} + \frac{R_s p'(\chi_0)}{B_{Ps}} + \frac{II'(\chi_0)}{R_s B_{Ps}}\right).
\end{aligned} \tag{2.24}$$

Equations (2.23) and (2.24) are convenient, since they allow to specify the safety factor and shear instead of I and I'.

The formalism presented here will be applied in two ways in the following chapters. The first application is the calculation of local equilibria with specific features such as X-points.

The second application is the computation of local equilibria using the results of the numerical reconstruction of experimental plasma equilibria.
A useful parametrisation of the flux-surface shape – in the following referred to as Miller geometry – allowing a systematic study of the effects of plasma elongation and triangularity, which are important features of divertor configurations, has been given in [12] and is cited here as an example for the formalism explained before. The flux-surface is defined by

$$\begin{aligned} R_s &= R_0 + r\cos\left(\theta + \arcsin(\delta)\sin(\theta)\right), \\ Z_s &= \kappa r \sin(\theta). \end{aligned} \tag{2.25}$$

In order to derive a parametrisation of the poloidal magnetic field in terms of the elongation κ and the triangularity δ, one assumes for the moment that neighbouring flux surfaces are parametrised like (R_s, Z_s), i.e. $R_0 = R_0(r)$, $\kappa = \kappa(r)$, and $\delta = \delta(r)$. The poloidal field $B_{Ps} = \left|\nabla\chi\right|/R_s$ in the coordinate system (r, θ, ζ) can then be shown to be

$$\begin{aligned} B_{Ps} = (\partial_r\chi)\sqrt{\sin^2(\theta + x\sin(\theta))(1 + x\cos(\theta))^2 + \kappa^2\cos^2(\theta)}\,/ \\ \{\kappa R_s\left[\cos(x\sin(\theta)) + \partial_r R_0\cos(\theta) + (s_\kappa - s_\delta\cos(\theta)\right. \\ \left. + \ (1 + s_\kappa)x\cos(\theta))\sin(\theta)\sin(\theta + x\sin(\theta))\right]\}, \end{aligned} \tag{2.26}$$

where $x \equiv \arcsin(\delta)$, $s_\kappa \equiv (r\partial_r\kappa)/\kappa$, and $s_\delta \equiv (r\partial_r\delta)/(1-\delta^2)^{1/2}$. The assumption made on the form of neighbouring flux-surfaces is now dropped, since it was needed only to derive an expression of B_{Ps} consistent with the parametrisation of the flux-surface. It is in no way necessary for the subsequent calculation of the local equilibrium data.

2.2 Theories of plasma dynamics

After the discussion of time-independent equilibrium analysis in the previous chapter, the theories applied in this thesis to study turbulence in such equilibria are introduced in the following.
The theoretical description of the dynamics of a magnetised plasma presents a complicated problem due to the large number of particles involved, which, furthermore, are charged. A plasma can contain many different positively and negatively charged particle species, each of them with particle numbers $N_s \sim 10^{23}$. The formally exact physical representation of plasma dynamics is comprised of the Lorentz force and Maxwell's equations, resulting in a problem in $6 \cdot 10^{23}$ dimensional phase-space. Neither is such a system manageable by today's computers, nor would the full solution – if it could be obtained somehow – be helpful in any way because of the huge amount of information it contains. The route to go is therefore to simplify the governing equations as far as allowed by the question one is interested in.
A simplification common to all approaches to plasma dynamics is the reduction of the dimensionality of the problem from $d \sim 6 \cdot 10^{23}$ to just $d = 6$ by means of the BBGKY-approximation (see e.g. [49]), which transforms the Liouville equation into the Boltzmann equation and thereby wraps microscopic particle interactions into a collision operator.

Instead of the position and momentum of every particle in the plasma, for each particle species a six dimensional distribution function $f_s(\mathbf{x}, \mathbf{v}, t)$ is evolved specifying the density of the particles of species s at a certain position with a certain velocity.
Since only the lowest moments of each distribution function f_s are needed to compute ρ and $\mathbf{j}$, i.e. the particle density and the velocity moment (the source terms in Maxwell's equations), and since several different solutions of f_s can yield the same charge density and currents, further simplifications are possible. Two approaches that are common in plasma physics are the fluid and the (gyro-) kinetic description. Fluid theory is based on the derivation of equations describing the time evolution of the lowest moments of the distribution function, density, temperature and velocity [1]. Since the time derivative of one moment of the distribution function necessarily involves the next higher moments, fluid models rely on closure relations that truncate the hierarchy of moments at some point of the approximation.
The kinetic approach can be simplified by exploiting the smallness of the gyroradius compared to the system size and the rapidity of particle gyration compared to other processes. The kinetic Boltzmann description can thus be expanded in terms of a small parameter, which after averaging over the gyration leads to the driftkinetic and gyrokinetic description of a plasma.
In general, fluid equations are much cheaper regarding computational effort and easier to evaluate. However, some kinetic effects cannot be reproduced exactly by fluid theories. Two theories of plasma dynamics are applied in this thesis – mainly two-fluid theory and at some points gyrokinetic theory – and are therefore discussed in the remainder of this section.

2.2.1 Gyrokinetic theory

The derivation of the gyrokinetic equation presented here follows Ref. [21] and is mainly based on the application of an ordering principle and physical reasoning. A technically strict derivation applying Hamiltonian techniques is reviewed in Ref. [50]. However, the former approach suffices to demonstrate briefly the basic principle of gyrokinetics.
Starting in 6-dimensional phase-space and excluding atomic and nuclear reactions, i.e. keeping the particle number constant, conservation of phase-space density yields the kinetic equation

$$\frac{\mathrm{d}f}{\mathrm{dt}} = \frac{\partial f}{\partial t} + \mathbf{v} \cdot \nabla f + \mathbf{a} \cdot \nabla_{\mathbf{v}} f = \hat{C} f, \tag{2.27}$$

where $\hat{C}$ is the particle collision operator and the acceleration $\mathbf{a}$ is given by the Lorentz force

$$\mathbf{a} = \dot{\mathbf{v}} = \frac{q}{m}\left(\mathbf{E} + \frac{1}{c}\mathbf{v} \times \mathbf{B}\right) \tag{2.28}$$

[1] Magnetohydrodynamic theory, which computes the current and charge density instead and is also a fluid theory, will not be discussed here.

with particle mass m and charge q. The source terms of Maxwell's equations needed to close the problem are given by

$$\rho = \sum_s q_s \int \mathrm{d}^3 v f_s,$$
$$\mathbf{j} = \sum_s q_s \int \mathrm{d}^3 v \mathbf{v} f_s. \tag{2.29}$$

Here, the index "s" refers to the particle species. The problem may be simplified by introducing an ordering principle which selects from the kinetic equation (2.27) the terms of interest for the problem under consideration. The study of a magnetised plasma requires the (background) scale length L (or system size) of the plasma to be much larger than the thermal ion gyroradius

$$\frac{\rho_i}{L} \sim \delta \ll 1, \tag{2.30}$$

where $\rho_i = v_t/\Omega$ with the thermal velocity $v_t \equiv (2T_i/m_i)^{1/2}$ and the ion gyro-frequency $\Omega \equiv q_i B/m_i c$. The plasma is allowed to vary on two different length scales L and $\lambda \sim \rho_i$. All features contained in f varying at the scale L describe the plasma equilibrium, for example the background density and temperature gradients, whereas the features varying at the size of a gyroradius describe small perturbations of the equilibrium quantities, especially the response of the plasma to small scale field fluctuations. The latter need to be small in amplitude compared to the former because fluctuations at the gyroradius scale with amplitudes comparable to the equilibrium quantities would demagnetise the plasma [21] by effectively destroying the gyro-orbits. Therefore, gyrokinetic theory – at least in the ordering used here – can be applied only to instabilities with small fluctuation amplitudes. Thus, the distribution function can be decomposed into

$$f = f_0 + f_1 \tag{2.31}$$

with

$$\frac{f_1}{f_0} \sim \Delta \ll 1, \tag{2.32}$$

where the index "0" refers to scale L and the index "1" to scale ρ_i. In this context, the definitions of the parallel unit vector $\mathbf{b}$ and the gyro-frequency Ω are refined to $\mathbf{b} \equiv \mathbf{B}_0/B_0$ and $\Omega \equiv q_i B_0/m_i c$. Next, all terms in the kinetic equation (2.27) have to be ordered according to the parameters δ and Δ. Although the single particles are gyrating around the field lines with the gyro-frequency, it is plausible to assume that the macroscopic quantities of the plasma vary at a much longer time scale. And since the focus of gyrokinetic theory is on the time evolution of instabilities, whose time scale is shorter than that of the equilibrium, it is assumed that

$$\frac{\partial f_0}{\partial t} = 0, \quad \frac{\partial f_1}{\partial t} \sim \delta\Delta\Omega. \tag{2.33}$$

The velocity in $\mathbf{v} \cdot \nabla f$ is of order v_t, whence

$$\mathbf{v} \cdot \nabla f \sim \frac{v_t}{L} + \Delta \frac{v_t}{\rho_i} = \omega_t + \Delta\Omega = \Omega\left(\delta + \Delta\right). \tag{2.34}$$

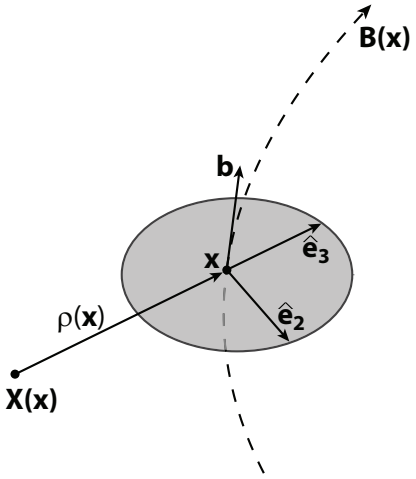

Figure 2.4: Relation between particle position $\mathbf{x}$ and guiding centre position $\mathbf{X}$. Since the motion of a particle at $\mathbf{x}$ is determined by the fields at position $\mathbf{x}$, the gyro-radius vector $\boldsymbol{\rho}$, the basis vectors $(\mathbf{b}, \hat{\mathbf{e}}_2, \hat{\mathbf{e}}_3)$ *and* the guiding centre position $\mathbf{X}$ relate to the particle position $\mathbf{x}$, not vice-versa.

Here, $\omega_t \equiv v_t/L$ is the transit frequency and $\omega_t/\Omega \sim \delta$. Clearly, the magnetic field part of the acceleration term fulfills

$$\frac{q}{mc}(\mathbf{v} \times \mathbf{B}) \cdot \nabla_{\mathbf{v}} f \sim \Omega f \tag{2.35}$$

because it contains the acceleration involved in particle gyration. The collision operator is assumed to be small,

$$\hat{C} f \sim \delta f, \tag{2.36}$$

which seems reasonable, since the plasma cannot be considered magnetised if the particle collision frequency is of the order of or higher than the gyro-frequency. The magnetic moment of the particles would no longer be an adiabatic invariant. As a consequence, the acceleration term due to the parallel component of the electric field has to be small to keep the approach consistent because the only term in Eq. (2.27) being able to cancel the acceleration along the field lines is the collision term. Choosing the parallel electric acceleration larger than the collision term would result in a continuous unbalanced acceleration of the parallel rotation of the plasma. Therefore,

$$\frac{q}{m}\mathbf{E}_{\parallel} \cdot \nabla_{\mathbf{v}} f \sim \frac{qE_{\parallel}}{mv_t} f \equiv \nu_E f \sim \delta\Omega f. \tag{2.37}$$

Finally the acceleration term due to the perpendicular electric field can be expressed as

$$\frac{q}{m}\mathbf{E}_{\perp} \cdot \nabla_{\mathbf{v}} f \sim \frac{v_E}{v_t}\Omega f, \tag{2.38}$$

where v_E is the magnitude of the $\mathbf{E} \times \mathbf{B}$ drift velocity $\mathbf{v}_E \equiv (c/B)\mathbf{E} \times \mathbf{b}$. In gyrokinetic theory, $\mathbf{E} \times \mathbf{B}$ drifts are assumed to be small compared to the thermal velocity,

$$\frac{v_E}{v_t} \sim \delta, \tag{2.39}$$

enabling the study of electrostatic instabilities, which represent an important class of micro-instabilities (see Ref. [21]).
The following derivation of the gyrokinetic equation uses guiding centre coordinates $\mathbf{X}$ rather than particle coordinates $\mathbf{x}$ in position space, where $\mathbf{X}$ is simply the current centre of the gyration of a particle at position $\mathbf{x}$ with a certain velocity $\mathbf{v}$ at time t. The connection between those two positions is the gyroradius vector $\boldsymbol{\rho}$. With $(\mathbf{b}, \hat{\mathbf{e}}_2, \hat{\mathbf{e}}_3)$ being a right-handed orthonormal basis set at the particle position $\mathbf{x}$ the velocity can be expressed as

$$\mathbf{v} = \mathbf{u} + \mathbf{s} = u\mathbf{b} + s\hat{\mathbf{s}} = u\mathbf{b} + s\left(\hat{\mathbf{e}}_2 \cos(\gamma) - \hat{\mathbf{e}}_3 \sin(\gamma)\right), \tag{2.40}$$

where γ is the gyrophase. The gyroradius vector is given by

$$\boldsymbol{\rho} = \frac{\mathbf{b} \times \mathbf{s}}{\Omega} = \rho\hat{\boldsymbol{\rho}} = \rho\left(\hat{\mathbf{e}}_2 \sin(\gamma) + \hat{\mathbf{e}}_3 \cos(\gamma)\right). \tag{2.41}$$

The relation between $\mathbf{x}$ and $\mathbf{X}$ is

$$\mathbf{X} \equiv \mathbf{x} - \boldsymbol{\rho}. \tag{2.42}$$

These relations are illustrated in Fig. 2.4.
In velocity space, the magnetic moment $\mu \equiv ms^2/2B_0$ of a particle, the particle energy $U \equiv mv^2/2 - q\Phi$ and the gyrophase γ are used as coordinates. The kinetic equation (2.27) therefore takes the form

$$\frac{\partial f}{\partial t} + \frac{\mathrm{d}\mathbf{X}}{\mathrm{d}t} \cdot \frac{\partial f}{\partial \mathbf{X}} + \frac{\mathrm{d}\mu}{\mathrm{d}t}\frac{\partial f}{\partial \mu} + \frac{\mathrm{d}U}{\mathrm{d}t}\frac{\partial f}{\partial U} + \frac{\mathrm{d}\gamma}{\mathrm{d}t}\frac{\partial f}{\partial \gamma} = \hat{C}f, \tag{2.43}$$

so the first task is to compute the equations of motion of the variables (see App. B). The results are

$$\begin{aligned}
\frac{\mathrm{d}\mu}{\mathrm{d}t} &= \dot{\mu}_0 + \dot{\mu}_1 \sim \omega_t \mu + \Delta\Omega\mu, \\
\dot{\mu}_0 &= -\frac{\mu}{B_0}\mathbf{v} \cdot \nabla B_0 - \frac{mu}{B_0}\mathbf{s} \cdot (\mathbf{v} \cdot \nabla)\,\mathbf{b} + \frac{q}{B_0}\mathbf{s} \cdot \mathbf{E}_0, \\
\dot{\mu}_1 &= \frac{q}{B_0}\left(\mathbf{s} \cdot \mathbf{E}_1 - \frac{us}{c}\hat{\boldsymbol{\rho}} \cdot \mathbf{B}_1\right),
\end{aligned} \tag{2.44}$$

$$\begin{aligned}
\frac{\mathrm{d}\gamma}{\mathrm{d}t} &= \omega_0 + \omega_1 \sim (\Omega + \omega_t) + \Delta\Omega, \\
\omega_0 &= \Omega + \hat{\mathbf{e}}_3 \cdot (\mathbf{v} \cdot \nabla)\,\hat{\mathbf{e}}_2 + \frac{u}{s}\hat{\boldsymbol{\rho}} \cdot (\mathbf{v} \cdot \nabla)\,\mathbf{b} - \frac{q}{ms}\hat{\boldsymbol{\rho}} \cdot \mathbf{E}_0, \\
\omega_1 &= -\frac{q}{ms}\hat{\boldsymbol{\rho}} \cdot \mathbf{E}_1 + \Omega\left(\mathbf{b} - \frac{u}{s}\hat{\mathbf{s}}\right) \cdot \mathbf{B}_1,
\end{aligned} \tag{2.45}$$

$$\frac{\mathrm{d}U}{\mathrm{d}t} = q\frac{\partial \Phi_1}{\partial t} - \frac{q}{c}\mathbf{v} \cdot \frac{\partial \mathbf{A}_1}{\partial t} \sim \Delta\omega_t U, \tag{2.46}$$

$$\begin{aligned}
\frac{\mathrm{d}\mathbf{X}}{\mathrm{d}t} &= \mathbf{v}_0 + \mathbf{v}_1 \sim (\omega_t + \delta v_t) + \Delta v_t, \\
\mathbf{v}_0 &= \mathbf{u} + \mathbf{v}_{E,0} + \frac{1}{\Omega}\mathbf{v} \times (\mathbf{v} \cdot \nabla)\,\nabla\mathbf{b} + \boldsymbol{\rho}\frac{(\mathbf{v} \cdot \nabla)\,B_0}{B_0}, \\
\mathbf{v}_1 &= \mathbf{v}_{E,1} - \mathbf{v}\frac{\mathbf{b} \cdot \mathbf{B}_1}{B_0} + \frac{u}{B_0}\mathbf{B}_1,
\end{aligned} \tag{2.47}$$

where $\mathbf{v}_{E,0/1}$ are the $\mathbf{E}\times\mathbf{B}$ velocities computed with $\mathbf{E}_0$ and $\mathbf{E}_1$, respectively. Since variations on the time scale of the gyration are not of interest in the discussion of plasma instabilities, those variations are eliminated from Eq. (2.43) by taking its gyro-average at fixed $\mathbf{X}$ defined by

$$\bar{A} = \langle A \rangle_\gamma \equiv \frac{1}{2\pi} \oint A(\mathbf{X}+\boldsymbol{\rho}, U, \mu, \gamma) \mathrm{d}\gamma. \tag{2.48}$$

Since the collision operator is an approximate term anyway and does not influence the argumentation below, it is dropped now. Afterwards, the collisionless gyrokinetic equation can be modified by introducing an appropriate collision operator. It is convenient to make the following ansatz for the distribution function f

$$f = f_0(U_0+U_1) + f_1(U_0), \tag{2.49}$$

which includes part of the linear (in Δ) perturbation in the background distribution. The perturbed distribution function $f_1(U_0)$ is assumed to be independent of the gyrophase and the only gyrophase dependent part is due to the perturbed field U_1 in $f_0(U_0+U_1)$. This part is comparable to f_1 and will be seen to represent plasma polarisation. The point in doing so is that the function $f_0(U_0+U_1)$ is assumed to be the exact solution to the kinetic equation in case of time-independent fields Φ and $\mathbf{A}$, this is it solves

$$\underbrace{\frac{\partial f_0(U_0+U_1)}{\partial t}}_{=0} + (\mathbf{v}_0+\mathbf{v_1})\cdot\frac{\partial f_0(U_0+U_1)}{\partial \mathbf{X}} + (\dot{\mu}_0+\dot{\mu}_1)\frac{\partial f_0(U_0+U_1)}{\partial \mu} + \underbrace{\dot{U}\frac{\partial f_0(U_0+U_1)}{\partial U}}_{=0} + (\omega_0+\omega_1)\frac{\partial f_0(U_0+U_1)}{\partial \gamma} = 0. \tag{2.50}$$

The two terms involving partial time derivatives of the fields vanish in case of time-independent fields. However, even if the time-dependence of the perturbed fields Φ_1 and $\mathbf{A}_1$ is included, the terms in Eq. (2.50) containing no time derivatives of the fields with the distribution function $f_0(U_0+U_1)$ sum up to zero. So the kinetic equation with time-dependent fluctuating fields consists of the kinetic equation (2.43) with $f \to f_1(U_0)$ and the correction terms of Eq. (2.50) due to the time dependence of Φ_1 and $\mathbf{A}_1$. To keep the notation simple, $f_1(U_0) \equiv f_1 = \bar{f}_1$ and due to the smallness of U_1, $f_0(U_0+U_1) \approx f_0(U_0) + U_1(\partial f_0(U_0)/\partial U)$ and $f_0(U_0) \equiv f_0 = \bar{f}_0$. Thus, one has for f_1

$$\underbrace{\frac{\partial f_1}{\partial t} + (\mathbf{v_0}+\mathbf{v}_1)\cdot\frac{\partial f_1}{\partial \mathbf{X}}}_{\sim\delta\Delta\Omega+\Delta^2\Omega} + \underbrace{(\dot{\mu}_0+\dot{\mu}_1)\frac{\partial f_1}{\partial \mu}}_{\sim\delta\Delta\Omega+\Delta^2\Omega} + \underbrace{\dot{U}\frac{\partial f_1}{\partial U}}_{\sim\delta\Delta^2\Omega}. \tag{2.51}$$

It is reasonable to distinguish the parallel and perpendicular scale lengths of the perturbed quantities. Since relevant instabilities vary on the gyroradius scale only perpendicular to the magnetic field, $\nabla_\perp f_1 \sim \Delta/\rho_i$, while varying on the system scale parallel to the field, $\partial_\parallel f_1 \sim \Delta/L$, the partial time derivative of f_1 as well as the linear (in the perturbations) part of the advection terms are of order $\delta\Delta\Omega$. The nonlinear part of the advection term

$\mathbf{v}_1 \cdot (\partial f_1/\partial \mathbf{X})$ is of order $\Delta^2\Omega$. The terms involving $\dot{\mu}$ are of order $\delta\Delta\Omega$ and $\Delta^2\Omega$. The $\dot{U}$ term is of order $\delta\Delta^2\Omega$ and is therefore neglected. The correction terms due to Eq. (2.50) are

$$\underbrace{\frac{\partial U_1}{\partial t}\frac{\partial f_0}{\partial U} + \dot{U}\frac{\partial f_0}{\partial U}}_{\sim\delta\Delta\Omega} + \underbrace{\dot{U}U_1\frac{\partial^2 f_0}{\partial U^2}}_{\sim\delta\Delta^2\Omega}, \tag{2.52}$$

where the last term of order $\delta\Delta^2\Omega$ is also neglected. The gyrokinetic equation is obtained by summing and gyro-averaging Eqs. (2.51) and (2.52):

$$\frac{\partial f_1}{\partial t} + \left\langle \mathbf{v}_0 + \mathbf{v}_1 \right\rangle \cdot \frac{\partial f_1}{\partial \mathbf{X}} + \left\langle \dot{\mu}_1 \right\rangle \frac{\partial f_1}{\partial \mu} + \left(\frac{\partial \bar{U}_1}{\partial t} + \left\langle \dot{U} \right\rangle \right) \frac{\partial f_0}{\partial U} = 0. \tag{2.53}$$

The gyro-averages $\left\langle \mathbf{v}_0 + \mathbf{v}_1 \right\rangle$, $\left\langle \dot{\mu}_1 \right\rangle$ and $\left\langle \dot{U} \right\rangle$ are calculated in App. B. It is intuitive to write the gyrokinetic equation in terms of $\delta\bar{f} \equiv \left\langle f - f_0(U_0) \right\rangle$. Since $f = f_0(U_0 + U_1) + f_1$, the averaged deviation from the unperturbed equilibrium distribution $f_0(U_0)$ is given by

$$\delta\bar{f} = f_1 + \bar{U}_1 \frac{\partial f_0}{\partial U}, \tag{2.54}$$

whence the full distribution function f can be decomposed into its gyro average and its gyrophase dependent part yielding

$$f = \bar{f} + \tilde{f} = \left(f_0 + \delta\bar{f}\right) + \left(U_1 - \bar{U}_1\right) \frac{\partial f_0}{\partial U}. \tag{2.55}$$

The gyrokinetic equation in terms of $\delta\bar{f}$ is

$$\frac{\partial \delta\bar{f}}{\partial t} + \left\langle \mathbf{v}_0 + \mathbf{v}_1 \right\rangle \cdot \frac{\partial}{\partial \mathbf{X}} \left(\delta\bar{f} - \bar{U}_1 \frac{\partial f_0}{\partial U} \right) + \tag{2.56}$$

$$+ \left\langle \dot{\mu}_1 \right\rangle \frac{\partial}{\partial \mu} \left(\delta\bar{f} - \bar{U}_1 \frac{\partial f_0}{\partial U} \right) + \left\langle \dot{U} \right\rangle \frac{\partial f_0}{\partial U} = 0. \tag{2.57}$$

The total perturbed distribution function is given by

$$\delta\bar{f} + \left(U_1 - \bar{U}_1\right) \frac{\partial f_0}{\partial U}, \tag{2.58}$$

where the second term yields a density perturbation linear in Φ_1 which represents the polarisation density ρ_{pol}. In order to calculate ρ_{pol} at the particle position $\mathbf{x}$, the second term in Eq. (2.58) has to be integrated over velocity space taking U_1 at position $\mathbf{x}$ and $\bar{U}_1$ at $\mathbf{X} + \boldsymbol{\rho}$, because the gyro-average implies that $\bar{U}_1$ is known only at the guiding centre $\mathbf{X}$ and has to be translated to $\mathbf{x} = \mathbf{X} + \boldsymbol{\rho}$. Therefore, the integration of $\bar{U}_1(\mathbf{X} + \boldsymbol{\rho})(\partial f_0/\partial U)$ eventually results in the "double gyro-average" of U_1 averaged over the background distribution f_0. This average can be written in terms of an integral operator $\hat{\Gamma}_0$, whose exact form depends on $f_0(U_0)$ (which usually is a Maxwellian). Finally, with the background density n_0, the polarisation density is given by:

$$\rho_{pol}(\mathbf{r}) = -\frac{q^2 n_0}{T}(1 - \hat{\Gamma}_0)\Phi_1. \tag{2.59}$$

Quasineutrality then requires that the densities of all species sum up to zero:

$$\sum_s q_s n_s + \sum_s \rho_{pol,s} = 0. \tag{2.60}$$

A detailed derivation of the gyrokinetic equation as implemented in the gyrokinetic code GYRO, which is used for most of the numerical gyrokinetic investigations, can be found in Ref. [15].

2.2.2 Two-fluid theory

As pointed out in the previous section, the quantities needed to close Maxwell's equations are the sources of the electromagnetic fields. Instead of evolving the plasma by means of an approximate equation of motion for the distribution function in five-dimensional phase space and afterwards calculating the sources from the approximate distribution function as done in gyrokinetic theory, conventional fluid theory derives approximate equations of motion for the plasma density, temperature and velocity directly as moments of the Boltzmann equation. The need for approximation arises from the fact that the time derivative of one moment of the distribution function inevitably involves higher moments, which can be understood presently from a simple example. The time derivative of the density in a co-moving reference frame – as is common in fluid dynamics – is given by

$$\frac{\mathrm{d}n}{\mathrm{d}t} = \frac{\partial n}{\partial t} + \mathbf{v} \cdot \nabla n = \text{source terms} \tag{2.61}$$

and is directly seen to involve the fluid velocity, the next higher moment. The equation of motion of velocity in turn follows an equivalent equation involving acceleration, i.e. heat sources and sinks. This hierarchy of fluid moments has to be cut at some point by adequate closure relations in order to obtain a numerically and if applicable analytically manageable system of equations. The approach discussed here is termed "two-fluid", since fluid equations are derived for both main species of the plasma, electrons and ions. A "one-fluid" model, in which fluid equations are obtained by averaging over velocity space and species, is represented for example by MHD.
Since the formal derivation outlined before will not be discussed in detail here, it is instructive to construct the general form of the class of fluid equations applied in this thesis. The requirements to be met by the fluid equations are equivalent to the basic idea of gyrokinetic theory: The phenomena described by the desired equations shall have frequencies much smaller than the ion cyclotron frequency. One can therefore expect that the perpendicular motion of a fluid element is described sufficiently accurate by the particle drift velocities. Thus, the time derivative of the density moment becomes

$$\frac{\mathrm{d}}{\mathrm{d}t} n\left(\mathbf{x}(t), t\right) = \left(\mathbf{v}_{Drift} + \mathbf{v}_{\parallel}\right) \cdot \nabla n + \frac{\partial n}{\partial t}. \tag{2.62}$$

On the other hand, the conservation of particle number gives

$$\frac{\partial n}{\partial t} = -\nabla \cdot \left(n(\mathbf{v}_{Drift} + \mathbf{v}_{\parallel})\right) = -\left(\mathbf{v}_{Drift} + \mathbf{v}_{\parallel}\right) \cdot \nabla n - n \nabla \cdot \left(\mathbf{v}_{Drift} + \mathbf{v}_{\parallel}\right), \tag{2.63}$$

and therefore

$$\frac{\mathrm{d}n}{\mathrm{d}t} = -n\nabla \cdot \left(\mathbf{v}_{Drift} + \mathbf{v}_{\parallel}\right). \tag{2.64}$$

Equation (2.64) implies that in a co-moving reference frame the time evolution of the density is mainly determined by the divergence of the particle drift velocities. The drift velocities of concern are the $\mathbf{E}\times\mathbf{B}$ drift $\mathbf{v}_E$, the curvature drift $\mathbf{v}_\kappa$, the ∇B drift $\mathbf{v}_{\nabla B}$ and the polarisation drift $\mathbf{v}_{pol}$ (see e.g. Ref. [21]) given by

$$\begin{aligned}
\mathbf{v}_E &= c\frac{\mathbf{E}\times\mathbf{b}}{B},\\
\mathbf{v}_\kappa &= \frac{u^2}{\Omega B}\mathbf{B}\times\boldsymbol{\kappa} \approx c\frac{T}{qB}\mathbf{b}\times\boldsymbol{\kappa},\\
\mathbf{v}_{\nabla B} &= \frac{\mu}{m\Omega}\mathbf{b}\times\nabla B \approx c\frac{T}{qB}\mathbf{b}\times(\nabla \ln B),\\
\mathbf{v}_{pol} &\approx \frac{c}{\Omega B}\frac{\mathrm{d}\mathbf{E}_\perp}{\mathrm{d}t} \approx -\frac{c}{\Omega B}\frac{\mathrm{d}}{\mathrm{d}t}\nabla_\perp\Phi.
\end{aligned} \tag{2.65}$$

In the polarisation velocity the electromagnetic part of the electric field arising from $\partial\mathbf{A}_\perp/\partial t$ can usually be neglected since it is small compared to $\mathbf{E}_\perp$ [51]. These drifts can be explained by noting that the motion of a charged particle due to an arbitrary force perpendicular to the magnetic field after averaging over the gyro-motion can be expressed to lowest order as a drift motion perpendicular to the arbitrary force and the magnetic field. In analogy to the $\mathbf{E}\times\mathbf{B}$ drift, one finds that $\mathbf{v}_{Drift} = c(\mathbf{F}/q)\times(\mathbf{b}/B)$. Thus, the curvature drift can be interpreted as a result of the centrifugal forces on a particle moving along a curved magnetic field line, the ∇B drift as the result of the force on a magnetic dipole in a nonuniform magnetic field, and the polarisation drift as the result of the varying electric field, $\mathbf{F} = m\dot{\mathbf{v}}_E$.

Defining the time derivative $\mathrm{d}/\mathrm{d}t$ as $\partial/\partial t + \mathbf{v}_E\cdot\nabla$, one obtains with the drift velocities (2.65)

$$\frac{\mathrm{d}n}{\mathrm{d}t} = -n\nabla\cdot\mathbf{v}_E - \nabla\cdot\left[\left(\mathbf{v}_\kappa + \mathbf{v}_{\nabla B} + \mathbf{v}_{pol} + \mathbf{v}_{\parallel}\right)n\right]. \tag{2.66}$$

To obtain the equation of motion of the fluid density in a reference frame co-moving with the $\mathbf{E}\times\mathbf{B}$ velocity one now has to calculate the divergence of $\mathbf{v}_E$ and the divergence of the drift particle fluxes and the parallel particle flux. In App. B it is shown that

$$\nabla\cdot\mathbf{v}_E = c\frac{\mathbf{b}}{B}\times(\boldsymbol{\kappa} + \nabla(\ln B))\cdot\nabla_\perp\Phi \equiv -\hat{C}\Phi \tag{2.67}$$

and

$$\nabla\cdot(n(\mathbf{v}_\kappa + \mathbf{v}_{\nabla B})) = -\hat{C}\frac{p}{q}, \tag{2.68}$$

where $\hat{C}$ is called curvature operator. It is worth noting at this point that the divergence of the currents induced by the magnetic inhomogeneity drift $\mathbf{v}_\kappa + \mathbf{v}_{\nabla B}$ is nearly equal to the divergence of the diamagnetic current density.

With Eqs. (2.67) and (2.68) equations of motion for electron and ion density can be constructed. Since the polarisation drift is proportional to the particle mass, it can be

neglected completely in the electron density equation. For the same reason – the parallel velocity is proportional to the thermal velocity which again depends on the particle mass – the parallel velocity is defined only for the ions while the difference between $\nabla \cdot n\mathbf{v}_{\parallel,i}$ and $\nabla \cdot n\mathbf{v}_{\parallel,e}$ is accounted for by the parallel current density in the electron equation. Thus, one arrives at the following equations of motion for electron and ion densities:

$$\begin{aligned}\frac{\mathrm{d}n_e}{\mathrm{d}t} &= \hat{C}\left(\Phi + \frac{p_e}{q}\right) - \partial_\parallel \cdot \left(n\mathbf{v}_{\parallel,i}\right) - \partial_\parallel \frac{\mathbf{j}_\parallel}{q}, \\ \frac{\mathrm{d}n_i}{\mathrm{d}t} &= \hat{C}\left(\Phi + \frac{p_i}{q}\right) - \nabla \cdot \left(n\mathbf{v}_{pol}\right) - \partial_\parallel \cdot \left(n\mathbf{v}_{\parallel,i}\right). \end{aligned} \tag{2.69}$$

Similar equations can be derived for ion and electron temperatures. To close the system, one needs three more equations (apart from those for the temperatures): one for the divergence of the polarisation flux, one for the parallel ion motion and one for the parallel current. Without discussing the details, one can guess the general form of those equations. The parallel ion velocity mainly depends on parallel pressure gradients plus some term involving perpendicular magnetic field fluctuations arising from the parallel component of the vector potential $A_\parallel \equiv \Psi$, therefore

$$\frac{\mathrm{d}v_{\parallel,i}}{\mathrm{d}t} = -\partial_\parallel p + \mathrm{F}\left[\Psi\right]. \tag{2.70}$$

The parallel current density has to fulfill some form of Ohm's law relating the current to the parallel electric field

$$j_\parallel = \sigma E_\parallel - \sigma_p \partial_\parallel p_e = -\sigma\left(\partial_\parallel \Phi + \frac{1}{c}\frac{\partial \Psi}{\partial t}\right) - \sigma_p \partial_\parallel p_e, \tag{2.71}$$

where σ is the parallel conductivity and σ_p is a proportionality factor to correctly include the parallel pressure gradient.
The divergence of the polarisation flux can be obtained by exploiting quasineutrality. Therefore the charge density $\rho_c = \sum_s q_s n_s = 0$ at all times and the charge continuity equation is just $\nabla \cdot \mathbf{j} = 0$. The total current consists of the diamagnetic current $\mathbf{j}_{dia} = c(\mathbf{b}/B) \times \nabla p = qn(\mathbf{v}_\kappa + \mathbf{v}_{\nabla B}) + \nabla \times \mathbf{M}$ with the magnetization density $\mathbf{M}$, the polarisation current and the parallel current. Combining Eqs. (2.65), (2.68) and $\nabla \cdot \nabla \times \mathbf{A} = 0$, one obtains

$$\nabla \cdot \mathbf{j} = -\nabla_\perp \cdot \left(\frac{nmc^2}{B^2}\frac{\mathrm{d}}{\mathrm{d}t}\nabla_\perp \Phi\right) - \hat{C}p + \partial_\parallel j_\parallel = 0, \tag{2.72}$$

which is called vorticity equation. Due to the definition of the charge density, it represents the difference between the ion and electron density equations (2.69). Therefore, a closed two-fluid system is comprised of six equations: the electron density equation, the vorticity equation, the ion and electron temperature equations, the parallel ion velocity equation and a generalised Ohm's law.
Although the principle structure of two-fluid theory can be understood from the considerations above, those equations are lacking important physics. Particle collision induced effects like viscosity and collisionless damping effects like phase mixing have been neglected

completely. In order to include these effects, the two-fluid equations have to be derived in a consistent approach as demonstrated for example in Refs. [51, 52, 53]. Starting from the Boltzmann equation (2.27) with an approximate collision operator, one computes first the corresponding density, velocity and temperature moments for ions and electrons to obtain the density continuity equations, the momentum conservation equations and the temperature equations, which are commonly called Braginskii equations. This of course requires certain assumptions, for example that the distribution function is close to a Maxwellian at each position, that the background quantities vary on a timescale longer than the collisional time scale, that the parallel scale length $L_{\|}$ is longer than the mean free path along the field, and that the perpendicular scale length is longer than the ion gyroradius. Through the collision operator momentum exchange and heat transport enter the fluid equations. In a second step – discussed in detail in Ref. [51] – the Braginskii equations can be transformed into drift reduced Braginskii equations by applying an ordering principle which eliminates the time scale of particle gyration. In spite of the use of a "poor-man's" approach, the fluid equations derived above display striking similarity to the drift reduced Braginskii system derived in Ref. [51]. The specific fluid equations used for numerical studies with the two-fluid code NLET in this thesis are given in [14].

2.2.3 Discussion

Both approaches discussed in the previous sections, gyrokinetic and two-fluid theory, have the same scope, the study of instabilities and microturbulence in plasmas. Therefore, it seems appropriate to discuss shortly the strengths and shortcomings of the two theories.
One of the first advantages of fluid theory compared to gyrokinetic theory to cross one's mind is the lower dimensionality of the system to be solved. Since fluid theory is situated in the three-dimensional real space instead of five-dimensional phase space, a fluid code runs much faster for a given spatial resolution of the computational domain than a gyrokinetic code. Or conversely, much higher resolutions can be computed with given computational resources using a fluid description.
Additionally, since fluid theory describes the time evolution of densities, velocities and temperatures, it is much more intuitive and easier to understand. Furthermore, extensive diagnostics can be computed with little effort in fluid theory while the calculation of equivalent quantities with kinetic theory involves the calculation of possibly quite complicated moments of the distribution function by numerical integration.
The most prominent advantage of fluid theory, however, is the fact, that in contrast to gyrokinetic theory it does not require the use of the local approximation (see e.g. [14]) to describe small scale fluctuations. In gyrokinetic theory as presented in Sec. 2.2.1, the assumption that the perturbed quantities comprising instabilities and turbulence are small compared to the background is essential for the theory to work. The problem with this restriction is that in the edge of fusion plasmas the amplitudes of the turbulent perturbations can be of the order of the background quantities which makes this gyrokinetic approach break down.
But there are also kinetic effects that are not naturally contained in fluid theory. The influence of trapped particles for example, which has at least quantitative influence on

the results of numerical studies, is not reproduced by fluid equations. However, the most important kinetic effect missing in fluid theory is collisionless damping. Fluid theory is based on the assumption of high collisionality [21, 51, 22]. Therefore, since damping is mostly collisional, fluid treatment is very reliable in the edge region of fusion plasmas where temperatures are low and collisionality is high. Further inside, temperatures are high and the collision frequency becomes very low. In this regime collisionless effects like Landau damping and phase mixing dominate the dynamics of the plasma. If nevertheless one would like to use a fluid description in the low collisionality regime, collisionless damping has to be modeled in some way, for example by modified heat fluxes. The role of collisionless damping with respect to zonal flows and geodesic acoustic modes is discussed for example in Ref. [54].
In summary it can be stated that the predominant use of two-fluid theory in this thesis is justified since geodesic acoustic modes are indeed an edge phenomenon. However, a comparison of gyrokinetic and two-fluid results is presented in Chap. 4 to back up this statement. Furthermore, gyrokinetic theory is applied in addition to fluid theory in wide parts of Chap. 3.

2.3 Instability and turbulence

In the following, the two main mechanisms leading to instability and turbulence in a magnetised plasma are discussed trying to focus more on physical reasoning than on explicit calculations. Detailed discussions of those two instability mechanisms can be found in Refs. [1, 51]. In slab geometry, the magnetic field has no curvature and the dominant unstable modes are drift waves. In realistic geometries – realistic in the sense of tokamaks – the magnetic field is curved and sheared, which favours curvature driven instabilities. Common to both mechanisms is the need of density or temperature gradients, which act as energy sources for the growth of unstable modes.

2.3.1 Drift wave instability

Drift waves are fluctuations of the density and the electrostatic potential that can become unstable and turbulent. Since the drift wave instability occurs already in a very simple system – a homogeneous magnetic field with a non-vanishing plasma density gradient – and since the properties of drift waves like their scale length and frequency are in accord with experimental observations of turbulent transport, drift waves are often considered as the paradigm of microturbulence in magnetised plasmas.
The principle of drift waves and their instability can be explained without using heavy mathematics. Consider the situation depicted in Fig. 2.5. The magnetic field is assumed to be homogeneous, the density gradient is perpendicular to $\mathbf{b}$. One isobar is indicated in Fig. 2.5 a) to clarify the physical configuration. The electron response to any electrostatic potential perturbation is assumed to be adiabatic and parallel resistivity is neglected, i.e. if a potential fluctuation arises somewhere, the electrons adjust their density instantaneously, $n_e = (1 + e\Phi/T)n_0$, where n_0 is the equilibrium density. Therefore, any density perturbation goes along with a corresponding potential perturbation as shown in Fig. 2.5 a).

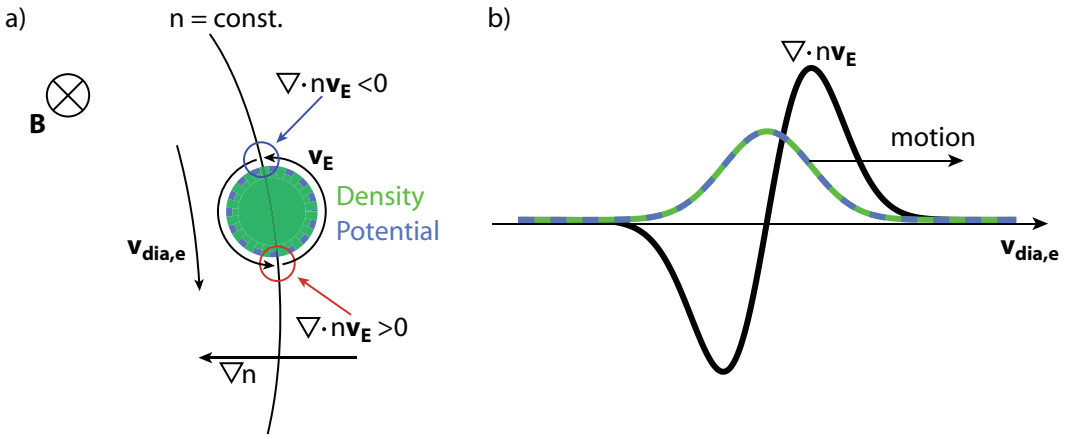

Figure 2.5: Stable drift waves. a) Due to the inhomogeneous density, the initial perturbation is moving with the electron diamagnetic velocity. Since density and potential perturbation are in phase, the fluctuation amplitude is constant. b) One-dimensional picture. Density and potential are in phase. The divergence of the $\mathbf{E}\times\mathbf{B}$ particle flux causes the potential and density fluctuations to move.

Due to the gradient of the potential perturbation, the density perturbation is surrounded by an $\mathbf{E}\times\mathbf{B}$ drift vortex. Since the density is not homogeneous, the component of the corresponding particle flux parallel to the density gradient has a divergence leading to an increase of the initial perturbation where $\mathbf{v}_E$ is antiparallel to ∇n and to a decrease where $\mathbf{v}_E$ and ∇n are parallel. Consequently, the divergence of the $\mathbf{E}\times\mathbf{B}$ flow leads to a motion of the initial perturbation perpendicular to the magnetic field and the density gradient, i.e. $\mathbf{v}\propto-(\mathbf{b})\times\nabla n\propto\mathbf{v}_{dia,e}$. For reasons of clarity, the situation is illustrated in one dimension in Fig. 2.5 b). Indeed, a proper calculation yields that the perturbations move exactly with the electron diamagnetic velocity $\mathbf{v}_{dia,e}=-c/(enB)\mathbf{b}\times\nabla p_e$ (see e.g. Ref. [1]).
This discussion explains the motion of a density perturbation but not its growth. Therefore, instead of a localised density perturbation consider now a perturbation sinusoidal in the diamagnetic direction. Measuring this density $n(\mathbf{x},t)$ at a fixed position while the perturbation is moving in the electron diamagnetic direction results in a periodic density oscillation. To understand how the perturbation can gain energy from the density gradient, an analogy can be drawn between drift wave growth and a driven harmonic oscillator. With the driving term taken as proportional to the velocity with a phase shift φ, the oscillator equation is

$$m\ddot{x}+kx=D\exp^{i\varphi}\dot{x}. \tag{2.73}$$

Thus, the rate of change of the total energy of the oscillator becomes

$$\frac{\mathrm{d}E}{\mathrm{d}t}=\frac{1}{2}\frac{\mathrm{d}}{\mathrm{d}t}\left(m\left|\dot{x}\right|^2+k\left|x\right|^2\right)=2D\left|\dot{x}\right|^2\cos\varphi. \tag{2.74}$$

From equation (2.74) it is concluded that if the driving term is in phase with the velocity $\dot{x}$ (i.e. out of phase with x), the energy input is maximal whereas the energy is conserved

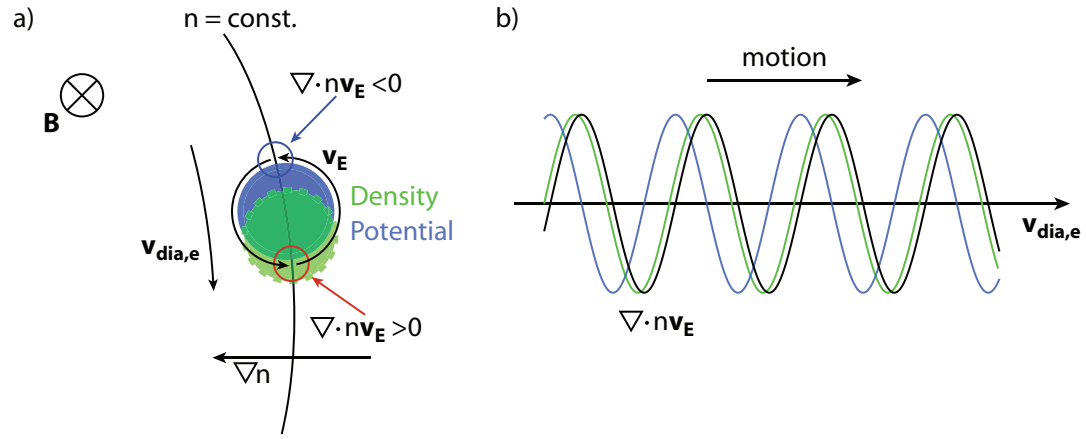

Figure 2.6: Unstable drift waves. a) Density and potential perturbations are phase shifted such that the maximum of the density perturbation is close to the maximum of the divergence of the $\mathbf{E} \times \mathbf{B}$ particle flux. Therefore, the initial perturbation is continuously fed by the $\mathbf{E} \times \mathbf{B}$ flow, the drift wave is unstable. b) Same situation in one dimension with sinusoidal perturbation.

if driving term and velocity are phase-shifted by $\pi/2$. For $\varphi = \pi$ the oscillation is damped. Even if the driving term does not change the total energy for $\varphi = \pi/2$, it modifies the oscillation frequency.

The transition to drift waves is straightforward. The density perturbation represents the oscillating quantity and the corresponding $\mathbf{E} \times \mathbf{B}$ drift the driving term. The difference between the simple drift wave picture is the lacking of a restoring force represented by kx in Eq. (2.73). The oscillation of the density perturbation at fixed position is due to the driving term alone. As long as density and potential perturbation, where the latter is responsible for the "external" drive, are in phase, drift waves do not grow. Note that the vanishing phase shift is based upon the assumption that the plasma has been assumed ideally conducting. If this assumption is dropped, the electron response to the density perturbation is delayed, resulting in a phase shift between n and ϕ, which goes along with growth or damping of the initial perturbation. Therefore, the existence of parallel resistivity is essential for the instability of drift waves. The effect of the phase shift between density and potential perturbation is illustrated in Fig. 2.6.

Assuming now the existence of a growing drift wave, there must be a saturation mechanism preventing infinite growth, since otherwise the plasma would collapse rapidly. This mechanism is illustrated in Fig. 2.7. Density and potential perturbations periodic in the diamagnetic direction as in Fig. 2.6 go along with opposite $\mathbf{E} \times \mathbf{B}$ flows. Such sheared flows if strong enough become unstable themselves due to the Kelvin-Helmholtz instability [51]. Small perturbations of the $\mathbf{E} \times \mathbf{B}$ flows generated by the primary instability perpendicular to the density gradient and the magnetic field start to grow deforming the initially straight flows to wiggly lines which eventually form vortices. Interaction between the vortices makes

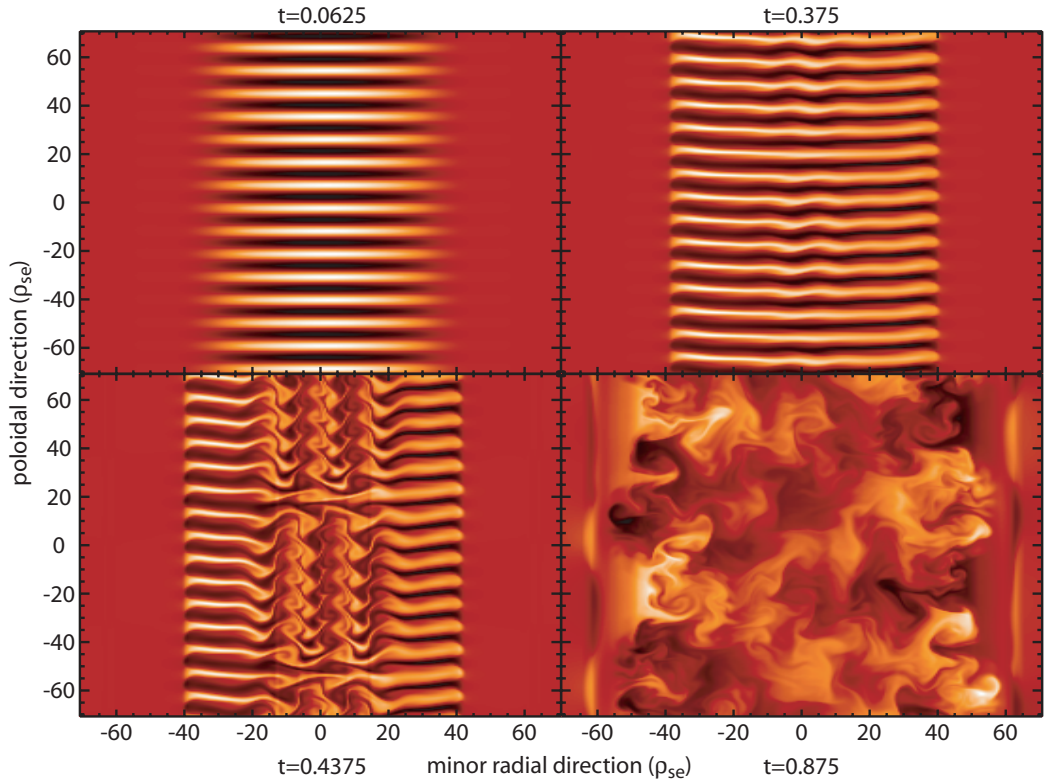

Figure 2.7: From a linear instability to turbulence (computed with the two-fluid code NLET [14]). The initial density fluctuation is periodic in the diamagnetic direction (top left). Having grown to a certain amplitude the opposite radial flows corresponding to the density fluctuation become unstable leading to small flow fluctuations in the poloidal direction, which deform the initial density perturbation (top right). The deformation generates vortices (bottom left) which due to their interaction decay into smaller and smaller vortices resulting in turbulence (bottom right). Length is measured in units of the sound Larmor radius ρ_{se}.

them break up into smaller and smaller eddies thus starting a turbulence cascade to smaller wave numbers at which the instability does not grow any longer or is even damped.

2.3.2 Curvature-driven instability

Although the drift wave instability is often cited as the paradigm for microturbulence in magnetically confined fusion plasmas, it essentially plays a minor role in tokamak geometry because drift waves are stabilised by magnetic shear [51]. Therefore, another mechanism is needed to explain the destabilisation of the plasma. Magnetic curvature, unavoidable in a closed confinement device, provides such a mechanism. Instabilities caused by non-vanishing curvature are categorised as curvature driven instabilities. Like the drift wave instability, curvature driven modes require an inhomogeneous plasma, e.g. a density (bal-

looning modes) or temperature gradient (ion temperature gradient driven modes, ITG) as their energy source. In tokamak geometry, the curvature vector $\boldsymbol{\kappa}$ can roughly be identified as the toroidal curvature, pointing to the symmetry axis with the curvature radius equal to the major radius R.
Figure 2.8 a) shows a situation typical for the outboard midplane of a tokamak. Density gradient ($\rightarrow$ ballooning mode) and curvature vector are pointing to the symmetry axis. On an isobar, a perturbation of the density is indicated. Due to the magnetic inhomogeneity drifts given in Eq. (2.65), which depend on the particle charge q, the ion density drifts in the ion diamagnetic direction and the electron density in the electron diamagnetic direction. Since the density perturbation provides a component of the density gradient in this direction, the magnetic inhomogeneity drifts lead to a charge separation and an electric field. The $\mathbf{E}\times\mathbf{B}$ flow resulting from the density perturbation (Fig. 2.8 b)) is – in principle – equivalent to the one shown in Fig. 2.5 a). Therefore, the explanation of the growth of the ballooning mode is analogous to the drift wave instability except for the $\mathbf{E}\times\mathbf{B}$ convection being induced by the curvature drift. Like the drift wave instability, ballooning modes become unstable due to parallel resistivity. However, also electromagnetic effects and electron inertia can drive the ballooning mode unstable [51].
In case of $\nabla n = 0$ and $\nabla T \neq 0$ ($\rightarrow$ ITG mode), on the contrary, the growth of an initial temperature fluctuation is due to the temperature dependence of the magnetic inhomogeneity drift: Hot particles drift faster than cold particles. Therefore, ions are compressed where electrons are expanded and vice versa, which induces a charge separation as in case of an initial density perturbation. Since the ITG instability requires a phase shift between the electrostatic potential and the temperature perturbation – instead of the density perturbation as in case of the ballooning modes – it can be unstable even in the electrostatic, ideally conducting limit.
Furthermore, it is obvious from Fig. 2.8 b) that the initial perturbation can only grow for $\nabla(n,T)\cdot\boldsymbol{\kappa} > 0$. The development of curvature driven modes from linear instability to turbulence is similar to that of drift waves.

2.4 GAM frequency in general geometry

The calculation of the GAM frequency in general geometry will become important in Chap. 6, however, just as a tool for the analysis of magnetic geometry effects on GAMs. Therefore, the algorithm upon which the results discussed in Chap. 6 are based is explained in this introductory section. Results obtained this way for Miller type geometries (Sec. 2.1.3 and [12]), are discussed in Ref. [11].
The following calculation is based upon two-fluid theory in the local and infinite aspect ratio limit as given in Ref. [51]. The coordinate system (x,y,z) therein is a flux-tube with the flux-label x indicating the minor radial position and z increasing along the field line. The coordinate y is chosen such as to be constant along a field line, i.e. y is a field line label, and a derivative with respect to y corresponds to a derivative with respect to the toroidal coordinate. Since, as explained in Sec. 1.1, GAM oscillations are the result of the coupling between a poloidal $(m,n) = (0,0)$ $\mathbf{E}\times\mathbf{B}$ flow, where n and m are the toroidal

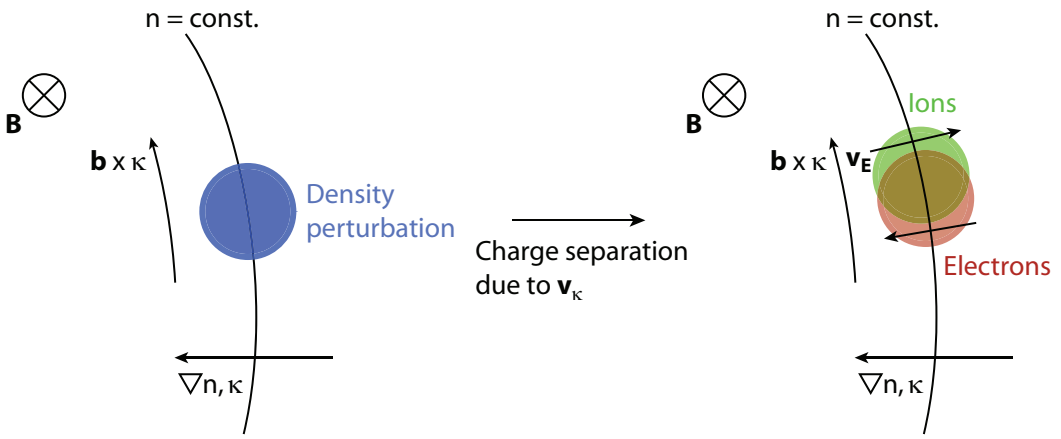

Figure 2.8: Growth mechanism of curvature driven instabilities. The magnetic inhomogeneity drifts try to advect ions and electrons in opposite directions resulting in a charge separation and a corresponding electric field. The $\mathbf{E} \times \mathbf{B}$ drift amplifies the initial perturbation when $\boldsymbol{\kappa} \cdot \nabla n > 0$. The indicated charge separation is exaggerated to clarify the growth mechanism.

and poloidal mode numbers, and a pressure perturbation acting as the restoring force, the linearised vorticity and the density equation are needed for the description of GAMs. If the coupling to the parallel velocity, i.e. to sound waves, is to be considered, one additionally needs the parallel velocity equation. Derivatives with respect to y are neglected for reasons of symmetry and the electron response is assumed adiabatic. From the sum of the vorticity and the electron density equation, one obtains the ion density equation, and integration of the vorticity equation over x and z yields the equation for the poloidal flow velocity. The vorticity, the ion density and the parallel velocity equation are given by

$$\begin{aligned}
\frac{\partial^3 \phi}{\partial t \partial x^2} &= -\hat{C} p - \tau \alpha_d \frac{\partial^3 p_i}{\partial t \partial x^2} + \partial_\parallel j_\parallel, \\
\frac{\partial n}{\partial t} &= \epsilon_n \hat{C} \left(\phi + \alpha_d p_i \right) + \epsilon_v \partial_\parallel v_\parallel + \alpha_d \epsilon_n (1+\tau) \frac{\partial}{\partial t} \frac{\partial^2}{\partial x^2} \left(\phi + \tau \alpha_d p_i \right), \\
\frac{\partial v_\parallel}{\partial t} &= -\epsilon_v \partial_\parallel p,
\end{aligned} \tag{2.75}$$

where the curvature operator is given by $\hat{C} = \sin(2\pi z)\partial/\partial x$, and $\tau = T_{i,0}/T_{e,0}$ is the ratio of the ion to electron background temperature. For a discussion of the other parameters appearing in Eq. (2.75) see Ref. [51]. Equation (2.75) contains only the fluctuating parts of density, temperature and pressure, which is why $p_{i,e} = n + T_{i,e}$ and $p = (p_e + \tau p_i)/(1+\tau)$. Assuming constant ion entropy, one can approximate $T_i \approx 2n/3$ and $p_i \approx 5n/3$. Neglecting electron temperature perturbations, the pressure becomes $(1+5\tau/3)/(1+\tau)n$. The poloidal $\mathbf{E} \times \mathbf{B}$ velocity is given by $\partial\phi/\partial x$. Since the GAM frequency is to be calculated in the limit $\partial/\partial x \to ik_x \to 0$, some terms can be neglected in addition to the y-derivatives. Those terms can be identified by an order analysis. One characteristic of the geodesic

acoustic mode is that the energy contained in the pressure perturbation and the poloidal flow averaged over one oscillation period are equal. The kinetic energy of the $\mathbf{E}\times\mathbf{B}$ flow is according to Refs. [51] and [55] $E_{kin,pol} = (1/2)\epsilon_n(1+\tau)(k_x\phi)^2$ and that of the pressure perturbation $E_p = (1/2)(1+5\tau/3)n^2$. Therefore, a GAM has to fulfill $n \sim k_x\phi$, and the GAM equations (2.75) in the limit $k_x \to 0$ become

$$\begin{aligned}\frac{\partial v_E}{\partial t} &= -\frac{1+\frac{5\tau}{3}}{1+\tau}\sin(2\pi z)n,\\ \frac{\partial n}{\partial t} &= \epsilon_n \sin(2\pi z)v_E + \epsilon_v \partial_\parallel v_\parallel,\\ \frac{\partial v_\parallel}{\partial t} &= -\epsilon_v \frac{1+\frac{5\tau}{3}}{1+\tau}\partial_\parallel n.\end{aligned} \tag{2.76}$$

For simplicity, the parallel motion is neglected in the following. To find the solution of the resulting system of partial differential equations for a geodesic acoustic mode, the flow velocity v_E is taken to be independent of y and z, whereas the density, which may depend on x and z is decomposed into a Fourier series in $\sin(2\pi mz)$ and $\cos(2\pi mz)$ with the poloidal mode number m. To simplify the form of the equations, the flow velocity is normalised to $\tilde{v}_E \equiv (\epsilon_n/2)^{1/2}v_E$ and the density to $\tilde{n} \equiv ((1+5\tau/3)/(2+2\tau))^{1/2}n$. Thus,

$$\begin{aligned}\frac{\partial}{\partial t}\tilde{v}_E &= -\omega_0 \sin(2\pi z)\sum_m \left(\tilde{n}_{s,m}\sin(2\pi mz) + \tilde{n}_{c,m}\cos(2\pi mz)\right),\\ \frac{\partial}{\partial t}\sum_m \left(\tilde{n}_{s,m}\sin(2\pi mz) + \tilde{n}_{c,m}\cos(2\pi mz)\right) &= \sin(2\pi z)\omega_0\tilde{v}_E,\end{aligned} \tag{2.77}$$

where ω_0 is given by

$$\omega_0 \equiv \sqrt{\frac{\epsilon_n}{2}\frac{1+\frac{5\tau}{3}}{1+\tau}}. \tag{2.78}$$

Due to the simplicity of the curvature operator in the local limit with infinite aspect ratio the flow of the GAM couples only to the sinusoidal pressure perturbation:

$$\frac{\partial}{\partial t}\langle\tilde{v}_E\rangle = \frac{\partial}{\partial t}\tilde{v}_E = -\omega_0\tilde{n}_{s,1}. \tag{2.79}$$

Therefore, only the sinusoidal component of the density equation is necessary to solve the problem, which can now be represented as the eigenvalue problem

$$\frac{\partial}{\partial t}\begin{pmatrix}\tilde{v}_E\\ \tilde{n}_{s,1}\end{pmatrix} = \begin{pmatrix}0 & -\omega_0\\ \omega_0 & 0\end{pmatrix}\begin{pmatrix}\tilde{v}_E\\ \tilde{n}_{s,1}\end{pmatrix} \tag{2.80}$$

with the eigenvalues $\omega = i\omega_{\mathrm{GAM}} = \pm i\omega_0$. Including the parallel velocity in the limit of infinite aspect ratio is straightforward.
However, in realistic geometry, the aspect ratio is finite, the magnetic field strength is no longer constant along a field line and the curvature operator $\hat{C} \propto \mathbf{b}\times\boldsymbol{\kappa}\cdot\nabla_\perp$ becomes far more complex than $\sin(2\pi z)$. Thus, the flux surface averaged poloidal flow $\tilde{v}_E$ couples to

many components $\tilde{n}_{s/c,m}$ of the density, and the GAM eigenvalue problem in principle has infinite dimensionality. When a specific magnetic geometry is analysed numerically with the method described in Sec. 2.1.3, one typically samples one toroidal circuit of a field line with a finite number of data points n_{num} allowing for the computation of Fourier series with $n_{\mathrm{num}}/2$ modes. In numerical computations, the calculation of the GAM frequency can thus be reduced to a n_{num} dimensional eigenvalue problem that can easily be solved – once all geometric coefficients have been calculated – yielding n_{num} eigenvalues and eigenvectors. This of course raises the question which of the eigenmodes correspond to a geodesic acoustic mode and which have dominating sound wave character. This question can be answered with the information provided by the eigenvectors, which allow to calculate the energies contained in the geodesic acoustic oscillation, i.e. in v_E and n, and the parallel flow $v_\parallel$. Thus, according to the ratio $E_{kin,\perp}/E_{kin,\parallel}$ of perpendicular to parallel kinetic energy, the "GAM-ness" of an eigenmode can be judged. Naturally, to be considered a GAM, the energy of the poloidal rotation must at least be comparable to the energy of the parallel flow whereas a mode with $E_{kin,\parallel} \gg E_{kin,\perp}$ is considered a sound wave.

Chapter 3

Linear GAM dispersion

This chapter, which is based on Refs. [41, 42] (see also App. E), is dedicated to the linear group velocity $v_g = \partial\omega(k_r)/\partial k_r$ of the GAM. Although GAMs are normally part of a turbulent system, it is nevertheless very useful to study their linear behaviour, in order to be able to judge how the turbulence modifies their properties. The nonlinear GAM dispersion is discussed in Chap. 5. A convenient and robust approach to the calculation of the group velocity – which contains much information on the dispersion relation – applying an energy principle will be presented. This energy approach allows for a relatively quick yet rather accurate calculation of the group velocity even for complicated magnetic geometries, and provides theoretical insight into the mechanisms of GAM propagation. The latter plays an important role in the formation of the global mode structure of the GAM as discussed in Ref. [10, 33].

The basic concepts of the method are demonstrated for two-fluid equations for cold ions and large safety factor q. The generalisation to warm ions, arbitrary safety factors and a gyrokinetic model is straightforward. Effects of the magnetic geometry are also considered, especially the influence of up-down asymmetric configurations like the single-null divertor configuration. The calculations are corroborated with exact analytical calculations for simple test cases and with numerical results obtained by the gyrokinetic codes GYRO [15] and GS2 [46], and the two-fluid code NLET [14].

This chapter is organised as follows. The basic idea of the approach presented here is discussed in Sec. 3.1. The energy functional which is applied to calculate the total energy and the Poynting flux of the GAM is introduced in Sec. 3.2. In Sec. 3.3 the equations for the free energy, its flux and the group velocity are derived within a two-fluid framework for $\tau = 0$, $q \to \infty$, low β, and high aspect ratio circular magnetic geometry. The calculation is generalised in Secs. 3.4 and 3.5 to the warm ion, finite q case and to the gyrokinetic model. In Sec. 3.6, the effects of plasma shaping on GAM propagation are discussed and an estimate of the group velocity for elongated plasmas is derived. The influence of up-down asymmetry of the magnetic geometry is investigated in Sec. 3.7 thereby generalising the results of Secs. 3.4 and 3.5.

3.1 Basic idea – the energy approach

Consider a flux-surface and a thin layer around it, and suppose that a geodesic acoustic mode is excited in this layer whereas outside of this layer the GAM intensity is zero. Since the geodesic acoustic mode is an axisymmetric perturbation, the plasma quantities related to the geodesic acoustic oscillation, the $\mathbf{E}\times\mathbf{B}$ velocity and the corresponding pressure perturbation, can be expressed as wave packets centered around the flux-surface under consideration, constructed of plane waves with specific radial wave numbers. Due to its symmetry, the GAM can only propagate in the minor radial direction.
The energy contained in a wave packet can be shown to be transported with the group velocity of the wave packet (e.g. Ref. [49]). This will be demonstrated in the following with the example of a one-dimensional Gaussian wave-packet of the quantity u and the corresponding energy $\left|u\right|^2$. The motivation of this approach is given by the nature of the GAM, which consists of an $\mathbf{E}\times\mathbf{B}$ velocity fluctuation, in the notation of Sec. 2.4 $v_E = k_r\phi$ with energy $\left|k_r\phi\right|^2/2$, and a pressure perturbation p with energy $\left|p\right|^2/2$. The wave packet is defined by

$$u(r,t) = \int_{-\infty}^{\infty} \tilde{u}(k_r)\exp\left[i\left(k_r r - (\omega(k_r) + i\gamma(k_r))t\right)\right]\mathrm{d}k_r, \tag{3.1}$$

where $\omega(k_r)$ is (the real part of) the dispersion relation and $\gamma(k_r)$ the corresponding damping rate. The weight function $\tilde{u}(k_r)$ is supposed to be Gaussian with a half width σ that is assumed to be small, such that the wave number dependence of the frequency and the damping rate can be approximated by their lowest order Taylor expansion in k_r. Thus, the wave packet becomes

$$u(r,t) = \int_{-\infty}^{\infty} \frac{1}{\sqrt{2\pi\sigma}}\exp\left[-\left(\frac{k_r - k_{r,0}}{\sigma}\right)^2\right]\exp\left[i\left(k_r r - (\omega_0 + i\gamma_0)t\right)\right] \times \exp\left[-i(v_{g,0} + i\gamma_0')(k_r - k_{r,0})t\right]\mathrm{d}k_r \tag{3.2}$$

with $\omega_0 \equiv \omega(k_{r,0})$, $\gamma_0 \equiv \gamma(k_{r,0})$, $v_{g,0} = \partial\omega/\partial k_r(k_{r,0})$ and $\gamma_0' \equiv \partial\gamma/\partial k_r(k_{r,0})$. This is easily integrated to

$$u(r,t) = \sqrt{\frac{\sigma}{2}}\exp\left[i\left(k_{r,0}r - \omega_0 t\right)\right]\exp\left[\gamma_0 t - \frac{\left(r - t(v_{g,0} + i\gamma_0')\right)^2\sigma^2}{4}\right] \tag{3.3}$$

and

$$\left|u(r,t)\right|^2 = \frac{\sigma}{2}\exp\left[2\gamma_0 t - \sigma^2\frac{(r - tv_{g,0})^2 - t^2{\gamma_0'}^2}{2}\right]. \tag{3.4}$$

The total energy is obtained by integrating Eq. (3.4) over space, which yields $E_{tot}(t) = \exp[t(4\gamma_0 + t{\gamma_0'}^2\sigma^2)/2]$. It is instructive to calculate the barycentre of the energy of the wave packet:

$$r_c = \frac{\int_{-\infty}^{\infty} r\left|u(r,t)\right|^2\mathrm{d}r}{E_{tot}(t)} = v_{g,0}t. \tag{3.5}$$

This shows that the energy of the wave packet is at least on average transported with the group velocity. The energy-flux of the wave packet can be computed via the continuity equation $\partial|u|^2/\partial t = -\nabla \cdot \mathbf{j} + S$. with a source term S accounting for the dissipation. Since Eq. (3.4) can be expressed as $|u|^2 = (\sigma/2)E_{tot}(t)\exp[-\sigma^2(r - v_{g,0}t)^2/2]$, it is immediately clear that the divergence of the energy-flux is given by $\partial|u|^2/\partial t|_{E_{tot}=const.} = (\sigma/2)E_{tot}\partial\exp[-\sigma^2(r - v_{g,0}t)^2/2]/\partial t$. Thus, the energy-flux becomes

$$j = -\int_{-\infty}^{r} \left.\frac{\partial|u|^2}{\partial t}\right|_{E_{tot}=const.} \mathrm{d}r = |u|^2 v_{g,0}, \tag{3.6}$$

which is exactly the product of group velocity and energy.
Thus, one can calculate the group velocity of a GAM wave packet by comparing its total energy to its energy-flux (Poynting flux). This provides a rather powerful tool for determining the direction and speed of GAM propagation.

3.2 The generalised grand canonical potential

The basic idea of the energy approach is vivid, however, the question remains which concrete energy functional is appropriate for the study of the propagation of geodesic acoustic modes. Looking at the orders of magnitude of the energies involved in the problem, one finds that the kinetic energy of the poloidal $\mathbf{E} \times \mathbf{B}$ rotation as well as the energy of the pressure perturbations of the GAM are of second order in the fluctuating quantities (see Sec. 2.4). Since GAM propagation is studied in the local limit in this chapter, these energy fluctuations are much smaller than, for example, the internal energy fluctuations, which are of first order in the fluctuations (proportional to $n_0\tilde{T}$ with the background particle density n_0 and the temperature fluctuation $\tilde{T}$). If the time evolution of the turbulent – i.e. nonlinear – system is not known exactly, e.g. only to second order in the fluctuations, problems can arise when trying to derive the time evolution of the energies connected with the propagation of the GAM. The discussion of this issue in Ref. [55] is summarised here and some points of the argumentation therein are clarified by explicit calculations.
In the local limit, the gradient scale lengths are assumed to be much larger than the computational domain. Let the ratio of these two scales be described by the small parameter ϵ. The time evolution of the perturbations can be described as in Ref. [55] by a state vector Ψ and the equation

$$\frac{\partial\Psi}{\partial t} = c_1\Psi + c_2\Psi^2 + \mathrm{O}(\epsilon^3), \tag{3.7}$$

where, due to the local limit, only the quadratic nonlinearity is retained. The coefficient c_1 of the linear term must be of order ϵ whereas c_2 is of order unity. The state vector Ψ is also of order ϵ [55]. Thus the time derivative of Ψ becomes

$$\frac{\partial\Psi}{\partial t} = \underbrace{d_2\left(\epsilon\Psi + \Psi^2\right)}_{\sim\mathrm{O}(\epsilon^2)} + \mathrm{O}(\epsilon^3) \equiv \left(\frac{\partial\Psi}{\partial t}\right)_2 + \mathrm{O}(\epsilon^3), \tag{3.8}$$

where $(\dots)_i$ is the i-th order term of $(\dots)$. Therefore, the time derivative of Ψ is known only to order ϵ^2, i.e. to second order in the fluctuations. The derivation of the energy-flux of the GAM relies on energy conservation $\partial_t E[\Psi] = -\nabla \cdot \mathbf{j}_E[\Psi]$, where $E[\Psi]$ is the energy functional that exactly conserves the GAM energy. Suppose for the moment that $E[\Psi]$ is the internal energy, which contains also energies linear in the fluctuations. Since Ψ is small, in order to compute $\partial_t E[\Psi]$ the energy functional is expanded as a power series in Ψ, such that

$$\begin{aligned}\frac{\partial E[\Psi]}{\partial t} &= \frac{\partial}{\partial t}\left(a_0 + a_1\Psi + a_2\Psi^2 + \dots\right) = a_1\frac{\partial \Psi}{\partial t} + a_2\frac{\partial \Psi^2}{\partial t} + \dots \\ &\equiv \frac{\partial E_1[\Psi]}{\partial t} + \frac{\partial E_2[\Psi]}{\partial t} + \dots,\end{aligned} \tag{3.9}$$

which can be evaluated by substituting the expression for $\partial_t \Psi$. It is straightforward to show that since $\partial_t \Psi$ is known only to order ϵ^2 the time derivative of the energy functional is also known only to that order, $\partial E[\Psi] = a_1(\partial_t \Psi)_2 + \mathrm{O}(\epsilon^3)$. However, this implies that the functional in the given approximation only conserves the first order term $E_1[\Psi]$ and is therefore inappropriate for the description of GAM propagation which requires the second order energies to be conserved.

If in contrast the linear term of the energy functional vanished, the time dependence of the second order term, $\partial_t E_2[\Psi]$, could be correctly described by $(\partial_t \Psi)_2$. Therefore, the desired energy functional should be minimal or maximal in the unperturbed ground state of the plasma, i.e. when $\Psi = 0$. This prerequisite is met by the generalised grand-canonical potential K introduced in Ref. [55], which is defined similar to the ordinary grand-canonical potential Ω of classical thermodynamics:

$$K \equiv U - \mu_0 N - T_0 S + p_0 V, \tag{3.10}$$

where U is the internal energy, N the particle number, S the entropy, and V the volume of the system, and μ_0, T_0 and p_0 are the unperturbed (i.e. background) chemical potential, temperature and pressure, respectively. Since $U = TS + \mu N - pV$ and $\Omega = U - \mu N - TS$ it follows immediately, that

$$K = \tilde{\mu} N + \tilde{T} S - \tilde{p} V, \tag{3.11}$$

where $\tilde{\mu}$, $\tilde{T}$, and $\tilde{p}$ are the fluctuating parts of the chemical potential, the temperature and the pressure. The generalised grand-canonical potential can therefore be regarded as a functional of the fluctuating quantities $\tilde{\mu}$, $\tilde{T}$, and $\tilde{p}$ and is consequently minimal in the unperturbed state when all fluctuations are zero. Thus, the generalised grand-canonical potential – in the remainder of this Chapter also referred to as free energy or simply energy – is appropriate for the description of the propagation of geodesic acoustic modes. For the derivation of gyrokinetic and fluid expressions of the second order term $K_2[\Psi]$ of K and of two-fluid equations that exactly conserve K_2 except for dissipation – which is beyond the scope of this thesis – the reader is referred to Ref. [55]. In the following, the tilde indicating fluctuating quantities is suppressed.

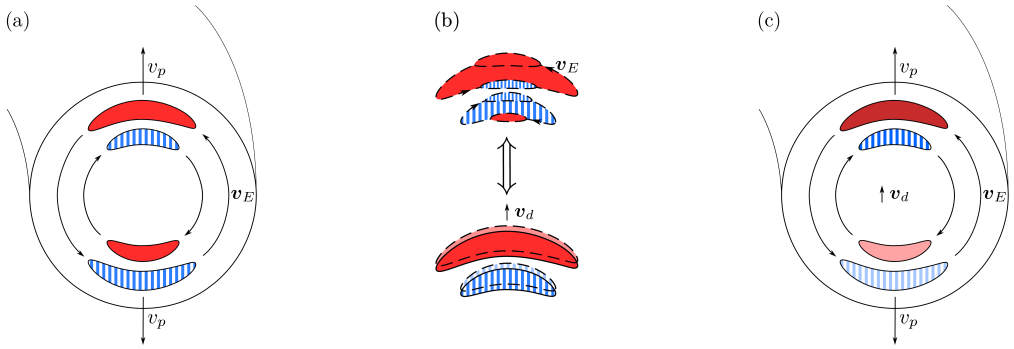

Figure 3.1: Sketch of a geodesic acoustic mode. (a) The poloidal $\mathbf{E}\times\mathbf{B}$-flow, moving with the GAM phase velocity v_p, leads to compression or expansion of the plasma (indicated by the filled and striped areas, respectively). Thus, an up-down antisymmetric $m = 1$ density perturbation arises, which is phase-delayed against the flow by $\pi/2$. (b) Density perturbations are associated with an $\mathbf{E}\times\mathbf{B}$ flow, which leads to compression or expansion of the plasma, causing the density perturbations to drift with the ion magnetic inhomogeneity drift velocity. (c) Parallel drift and phase velocity enhance the density perturbations caused by the GAM poloidal rotation, antiparallel v_d and v_p weaken the perturbations.

3.3 Fluid Model for cold ions and infinite safety factor

The units used in the following are chosen such that the magnetic drift velocity is unity. Density, n, temperature, T_i and T_e, and electric potential perturbations ϕ are normalised to

$$\rho^\star n_0, \quad \rho^\star T_{0,i/e}, \quad \rho^\star \frac{T_{0,e}}{e}, \tag{3.12}$$

respectively, where the subscript 0 indicates the corresponding background value and $\rho^\star$ is given by ρ_{se}/R with the major torus radius R, $c_{se} \equiv (T_{0,e}/m_i)^{1/2}$, and $\rho_{se} \equiv (m_i c_{se})\,/\,(eB)$. The time scale is $t_0 \equiv R/(2c_{se})$.

Beforehand, it is useful to recall the main characteristics of the GAM. An $(m, n) = (0, 0)$ $\mathbf{E}\times\mathbf{B}$ plasma flow, is generated by the flux-surface averaged electric field $-\nabla\phi_0$, with $\phi_0 \equiv \langle\phi\rangle$ and $\langle\ldots\rangle$ indicating flux-surface averaging. The divergence of the flow due to the magnetic inhomogeneities gives rise to a mainly up-down-antisymmetric $m = 1$ pressure perturbation [Fig. 3.1 (a)]. Since the compression of plasma requires work taken from the kinetic energy $(\nabla\phi_0)^2/2$ of the flow, a restoring force is generated, the flow is slowed down, stopped, and eventually reversed. An oscillation between pressure perturbations and flow results, in which the maximal energy stored in the pressure perturbations is comparable to the initial kinetic energy.

3.3.1 GAM Poynting flux and group velocity

As a first approach, the Poynting flux (and group velocity) of the GAM is calculated for the cold ion two-fluid equations according to Ref. [55] neglecting sound waves. Since in the

absence of perturbations the free energy is minimal, it is second order in the fluctuations. In the chosen framework, the free energy functional [55] is given by

$$\langle E \rangle = \langle E_e + E_i \rangle = \left\langle \frac{n^2}{2} + \frac{(\nabla\phi)^2}{2} \right\rangle, \tag{3.13}$$

where E_e and E_i are the electron and the ion free energy density, respectively, $n^2/2$ is the energy of the electron density perturbations, and $(\nabla\phi)^2/2$ the ion kinetic energy. The ion density fluctuations obey

$$\dot{n} - \Delta\dot{\phi} - \hat{C}\phi = 0, \tag{3.14}$$

where $\hat{C} \equiv -\boldsymbol{v}_d \cdot \nabla$ and $\boldsymbol{v}_d \equiv -(1/2)(\hat{\boldsymbol{\kappa}} + R\nabla \ln B) \times \hat{\boldsymbol{b}}$ is the sum of the curvature and ∇B-drifts of the electron density fluctuations, and $\Delta\dot{\phi}$ is the divergence of the polarisation current. The electrons are assumed to be adiabatic

$$n = \phi - \phi_0, \quad \langle n \rangle = 0, \tag{3.15}$$

because the GAM frequency is much smaller than the electron bounce and transit frequencies. By combining (3.13), (3.14), (3.15), and representing the time derivative of $\langle E \rangle$ as the divergence of a radial Poynting flux one obtains

$$\partial_t \langle E \rangle = -\langle \nabla \cdot \boldsymbol{S} \rangle = \left\langle -\nabla \cdot \left(\frac{\boldsymbol{v}_d n^2}{2} \right) + \nabla \cdot (n \nabla \dot{n}) \right\rangle. \tag{3.16}$$

The first term, $\boldsymbol{v}_d n^2/2$, represents the flow of the energy of electron pressure perturbations in ion magnetic drift direction. Since the radial component of $\boldsymbol{v}_d$ is up-down antisymmetric (for symmetric flux-surfaces), this energy-flux has a non-vanishing flux-surface average only if n^2 has an up-down asymmetry. That such an asymmetry exists and that the energy transport is in the ion drift direction can be shown as follows.
Due to adiabaticity, Eq. (3.15), the pressure fluctuations shown in Fig. 3.1 (a) are connected to potential fluctuations, which are encircled by $\mathbf{E} \times \mathbf{B}$-flows as indicated in Fig. 3.1 (b). Similar to the poloidal flow, the vortices lead to compression or expansion of the plasma owing to the magnetic field variations. This effect is equivalent to the advection of the density perturbation by the ion curvature drift, computed with the electron temperature. Due to resonance between GAM phase and magnetic drift velocity, the pressure perturbations are enhanced at poloidal angles where drift and phase velocity are parallel, whereas they are weakened where those velocities are antiparallel. Therefore, an up-down asymmetry of the energy density arises, which leads to a net radial energy transport through the flux-surface parallel to the phase velocity. Due to the asymmetry requirement, this flux somewhat resembles neoclassical density or temperature transport.
Owing to adiabaticity (3.15), pressure and potential perturbations are equal, so that the gradient of the local density fluctuations causes an electric field, whose time dependence gives rise to a polarisation current density $-\nabla\dot{n}$. Since the temperature is normalised to $T_{0,e}$, the term $-n\nabla\dot{n}$ can be interpreted as *hydraulic* energy-flux $p_e \boldsymbol{j}_{pol}$ consisting of the electron pressure $T_{0,e}n$ and the polarisation current density. It will be referred to as the polarisation energy-flux in the following. As the $\mathbf{E} \times \mathbf{B}$-flow associated with the density

perturbations is proportional to the density gradients, the polarisation energy-flux can be regarded as the energy-flux $-v_p(\nabla n)^2$, counter-intuitively with the reversed phase velocity v_p.
The requirement of up-down asymmetry of the free energy density $n^2/2$ makes the curvature flux comparable in size to $-n\nabla\dot{n}$, a polarisation effect. Whether the radial group and phase velocities eventually are parallel or antiparallel depends on the relative size of those two fluxes.
Next, the free energy and the Poynting flux, Eqs. (3.13) and (3.16), are evaluated in Fourier space for a circular high aspect ratio magnetic geometry. Recalling that the curvature operator $\hat{C}$ is up-down antisymmetric for circular flux-surfaces, one obtains an estimate for the density perturbations by splitting the ion density equation (3.14) into an up-down antisymmetric and a symmetric part with the corresponding densities n_a and n_s. Since the kinetic energy of the flow and the energy of the density fluctuations are of the same order, $k_r^2\phi_0 \sim n^2$, only terms up to first order in k_r are kept in the antisymmetric equation. The symmetric density fluctuations are of second order in k_r. Thus, with $\hat{C} = -\sin(\theta)\partial_r$, the density becomes

$$\begin{aligned} n_a &\approx \frac{k_r}{\omega}\sin(\theta)\,\phi_0, \\ n_s &\approx \left[\frac{1}{\omega^2}\sin(\theta)^2 - 1\right] k_r^2\phi_0. \end{aligned} \tag{3.17}$$

Due to electron adiabaticity the GAM frequency ω determined by $\langle n\rangle = \langle n_s\rangle = 0$ is given by $\omega = 2^{-1/2}$. Inserting (3.17) into (3.13) and (3.16) one obtains for the radial group velocity

$$v_{g,r} = \frac{\langle S_r\rangle}{\langle E\rangle} \approx -\frac{k_r}{2\sqrt{2}}. \tag{3.18}$$

Since the ratio of curvature to polarisation flux is $-1/2$, the total Poynting flux and the group velocity are antiparallel to the phase velocity for cold ions.
The free energy approach only requires knowledge of the up-down antisymmetric density fluctuation n_a and its symmetric correction n_s. The electron adiabaticity condition for n as given by Eq. (3.17) only yields the GAM frequency to 0th order in k_r. Thus, higher order corrections to the density have to be computed in order to calculate the group velocity directly from the dispersion relation. Hence, an advantage of the free energy approach is that less information is necessary compared to a direct calculation of the GAM frequency. The approximation (3.18) can be compared to the exact solution of (3.14), which due to the simplicity of the situation considered here can be obtained analytically and is given by

$$n = \phi_0\left(\frac{\sqrt{\Omega^2-1}}{\sin(\theta)+\Omega} - 1\right), \tag{3.19}$$

with $\Omega = (\omega/k_r)(1+k_r^2)$. The GAM frequency follows from the condition $\langle n\sin(\theta)\rangle = -\omega k_r\phi_0$, which is obtained from Eq. (3.14) by using (3.15), yielding $\omega = (2+k_r^2)^{-1/2}$ and the corresponding radial group velocity

$$v_{g,r} = -\frac{k_r}{(2+k_r^2)^{3/2}} \approx -\frac{k_r}{2\sqrt{2}} + O\left[k_r^3\right], \tag{3.20}$$

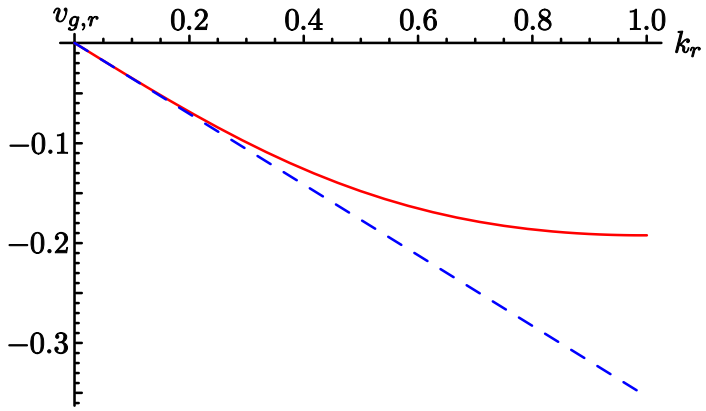

Figure 3.2: Exact GAM group velocity for $\tau = 0$, $q \to \infty$ (3.20) (solid) and approximation (3.18) (dashed).

which to lowest order in k_r is identical to the approximation (3.18). Figure 3.2 shows the exact group velocity in comparison with the approximated result. For small wave numbers the latter converges against the exact result. Deviations for larger wave numbers are due to drift velocity resonances. The resonance condition can be obtained from Eq. (3.14) giving

$$v_p \equiv \frac{\omega}{k_r} = \frac{\hat{\boldsymbol{k}} \cdot \boldsymbol{v}_d}{1 + k^2} = -\frac{\sin(\theta)}{1 + k_r^2} \tag{3.21}$$

for circular flux-surfaces. A mode loses the character of a GAM, if, due to resonances, the energy of the density perturbations becomes significantly larger than the kinetic energy. When the GAM frequency approaches a resonance, the density amplitude becomes very large compared to the poloidal rotation and dominates the mode. The resonant pressure perturbations propagate with the group velocity of the resonant drift mode, which is characterised as a $n = 0$ density perturbation localised at a specific poloidal angle θ. Accordingly, (3.14) and (3.17) imply, that the modes discussed here are GAMs for small radial wave numbers $k_r \ll 1$ only. Therefore, the deviations of the approximate frequency from the exact one shown in Fig. 3.2 are due to the transition of the mode from a GAM to a magnetic drift mode.

3.3.2 Numerical studies with NLET

To corroborate the analytical insights, linear numerical studies were carried out with the two-fluid code NLET. The computations were performed on a grid of 1024 radial and 32 parallel grid points with high aspect ratio circular geometry. The radial width of the computational domain was $400\,\rho_{se}$. The remaining parameters are $\epsilon = a/R = 0$, $\tau = 0$, and q ranging between 3 and ∞. The GAMs have been initialised at time $t = 0$ with an $(m, n) = (0, 0)$ electrostatic potential, which then evolves self-consistently.
An example for the resulting spectral density of the radial $\mathbf{E} \times \mathbf{B}$-flow profile $v_E(r, t)$ is shown in Fig. 3.3. The exact frequency, which also agrees with the numerical result,

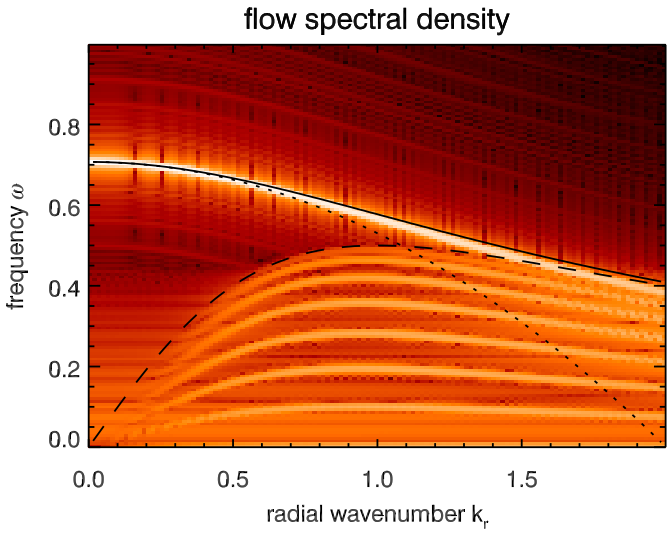

Figure 3.3: NLET computed log-colour-coded GAM spectrum (Fourier transform of ϕ) for $\tau = 0$ and $q = 30$ with exact analytical frequency (solid), approximate frequency [dotted, obtained by integrating Eq. (3.18)] and magnetic drift resonance frequency $k_r/\left(1+k_r^2\right)$ (dashed). The exact frequency (bright line) interpolates between the approximate and the resonance frequency. Also visible are additional drift modes enclosed by the resonance line.

interpolates between the approximation obtained by integrating (3.18) and the resonance frequency. For $k_r \lesssim 0.5$ the mode is obviously a GAM, whereas for larger k_r it is gradually taken over by the magnetic drift resonance. For $k_r \gtrsim 2$ the mode is completely dominated by resonant pressure perturbations as discussed in Sec. 3.3.1 and has lost the character of a GAM. The structure of the magnetic drift mode spectrum deserves comment here. Resonance of the GAM with the magnetic inhomogeneity drift occurs where the radial component of the magnetic drift velocity is equal to the GAM phase velocity resulting in a density perturbation localised at the poloidal position of the resonance. Therefore, one would expect the spectrum of the magnetic drift modes to be continuous, enclosed by the drift mode with the highest frequency, indicated by the dashed line in Fig 3.3. Instead, the spectrum consists of discrete lines. However, this is an artifact due to discretisation. Doubling the number of parallel grid points also doubles the number of drift modes observed in the spectrum.

3.4 Generalised fluid model

The generalisation of the preceding calculations is straightforward. Following Ref. [55], one can obtain the generalised ion free energy functional

$$E_i = \frac{1}{2}\tau n^2 + \frac{3}{4}\tau T_i^2 + \frac{1}{2}\left[\nabla\left(\phi + \tau\left(n + T_i\right)\right)\right]^2 + \frac{5}{4}\left(\nabla\tau T_i\right)^2 + \frac{1}{2}\left(v_\parallel^2 + \tau\left(\nabla v_\parallel\right)^2\right), \quad (3.22)$$

which includes ion temperature and parallel velocity. For warm ions, the ion density and temperature fluctuations contribute to the total free energy with $(1/2)\tau n^2+(3/4)\tau T_i^2$. The FLR (finite Larmor radius) heat flux contributes the energy density $(5/4)(\nabla\tau T_i)^2$. The energy density of the diamagnetic drift velocity increases by $\tau\nabla(n+T_i)$. For finite safety factor, the parallel flow $(1/2)v_\parallel^2$ and the FLR correction $(1/2)\tau(\nabla v_\parallel)^2$ also contribute to the total energy density. Fluid equations which exactly conserve the free energy functional [55] are given by

$$\dot{n}-\Delta\left(\dot{\phi}+\tau\dot{n}+\tau\dot{T}_i\right)+\left(1-\frac{5}{3}\tau\Delta\right)\partial_\parallel v_\parallel-\hat{C}\left(\phi+\tau n+\tau T_i-\tau\Delta a\right)=0, \tag{3.23}$$

$$\dot{T}_i-\frac{2}{3}\left[\Delta\left(\dot{\phi}+\tau\dot{n}+\frac{7}{2}\tau\dot{T}_i\right)+\left(1-\frac{7}{3}\tau\Delta\right)\partial_\parallel v_\parallel-\hat{C}\left(\phi+\tau n+\frac{7}{2}\tau T_i-\tau\Delta b\right)\right]=0, \tag{3.24}$$

$$\dot{v}_\parallel-\tau\Delta\dot{v}_\parallel+\left(1-\frac{5}{3}\tau\Delta\right)\partial_\parallel\left(\phi+\tau\left(n+T_i\right)\right)-\frac{5}{3}\tau^2\Delta\partial_\parallel T_i-2\tau\hat{C}\left(\left(1-\tau\Delta\right)v_\parallel\right)=0, \tag{3.25}$$

with $a\equiv\alpha(\phi+\tau n)+\beta\tau T_i$ and $b\equiv\beta(\phi+\tau n)+\gamma\tau T_i$. For a collisionless plasma, the three coefficients α, β and γ are given by $(11/6, 11/3, 85/12)$. Inserting (3.23-3.25) into $\partial_t E$ and writing the result in terms of divergences, the Poynting flux is seen to be

$$\begin{aligned}\partial_t\langle E\rangle=\Big\langle&-\nabla\cdot\left[\boldsymbol{v}_d\left(\frac{1}{2}\left(n+\tau p_i\right)^2+\frac{5}{4}\left(\tau T_i\right)^2+\tau v_\parallel^2\right)\right]\\&+\nabla\cdot\left[\left(n+\tau p_i\right)\nabla\left(\dot{n}+\tau\dot{p_i}\right)+\tau T_i\nabla\dot{\phi}_0+\frac{5}{2}\tau^2T_i\nabla\dot{T}_i+\tau v_\parallel\nabla\dot{v}_\parallel\right]\\&-\tau\nabla\cdot\left\{\boldsymbol{v}_d\left[\frac{\Delta}{2}\left(\alpha c^2+2\beta cd+\gamma d^2\right)-\frac{3}{2}\left(\alpha\left(\nabla c\right)^2+2\beta\nabla c\nabla d+\gamma\left(\nabla d\right)^2\right)\right.\right.\\&\left.\left.-\ \phi_0\Delta a+\tau\left(\Delta v_\parallel^2-3\left(\nabla v_\parallel\right)^2\right)\right]\right\}\Big\rangle,\end{aligned} \tag{3.26}$$

in which $c\equiv\phi+\tau n$ and $d\equiv\tau T_i$. The first two divergences on the right hand side of Eq. (3.26) represent the advection of the fluctuation energy by the magnetic drifts and the polarisation drift in complete analogy to the first term on the right hand side of Eq. (3.16). The last divergence in (3.26) is an FLR correction to the first one.

The two functionals (3.22), (3.26), and the group velocity can be approximated by splitting the fluctuations in (3.23-3.25) according to their up-down symmetry and keeping only the lowest order terms as in Sec. 3.3.1. When the GAM frequency approaches the sound frequency, the ratio of the energy densities of parallel flow velocity and density perturbations to the ion kinetic energy densities increases and tends towards infinity close to the resonance. Hence, the mode loses the character of a GAM. Sound wave resonance is negligible,

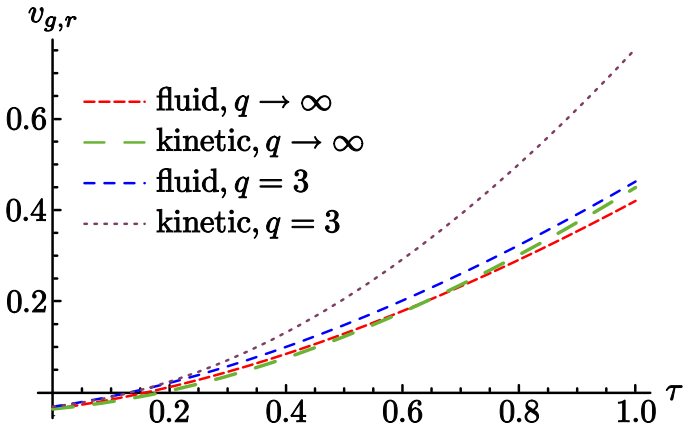

Figure 3.4: Ion temperature dependence of the fluid [Eq. (3.27)] and the kinetic [Eq. (3.34)] GAM group velocities for $k_r = 0.1$.

if $q \gg 1$ (in practice $q \gtrsim 3$ is sufficient). Inserting the approximate perturbations into (3.22) and (3.26), one obtains the group velocity

$$v_{g,r} = \frac{k_r}{2\sqrt{6}\,(3+5\tau)^{3/2}} \Big[\left(-9 + 21\tau + 189\tau^2 + 265\tau^3\right) + \frac{1}{4q^2\,(3+5\tau)} \left(135 + 1026\tau + 3324\tau^2 + 5360\tau^3 + 3675\tau^4\right) \Big] . \tag{3.27}$$

(For details see appendix C.2.) All additional terms compared to Eq. (3.18) are positive, which causes the group velocity to change sign at $\tau \approx 0.16$ (Fig. 3.4). When calculating GAM eigenmodes as in Ref. [33], regions of evanescent and propagating GAM would be switched at this critical τ because the group velocity is reversed. Since this might change the interaction of GAMs with the turbulence and since GAMs have recently been found to play an important role in nonlinear turbulence saturation [56], their propagation might influence turbulent transport.

3.5 Gyrokinetic model

For the generalisation of the previous discussion to gyrokinetic theory the linear model [57] (compare Sec. 2.2.1)

$$\partial_t f + \frac{\boldsymbol{v}_\mathrm{d}}{\tau} \cdot \nabla_\perp \left(\tau f + F_0 \hat{J}_0 \phi\right) + \frac{v_\parallel}{\tau} \partial_\parallel \left(\tau f + F_0 \hat{J}_0 \phi\right) = 0 \tag{3.28}$$

is applied with the quasineutrality condition

$$n + \frac{1 - \hat{\Gamma}_0}{\tau}\,\phi - \int \hat{J}_0 f \,\mathrm{d}^3 v = 0. \tag{3.29}$$

The velocity $\boldsymbol{v}_\mathrm{d}$ is the sum of the curvature and ∇B drift of the individual particles. F_0 is the thermal background distribution function, which is normalised such that $\int F_0 \,\mathrm{d}^3 v = 1$.

Gyro-averaging is represented by the operator $\hat{J}_0$ and the thermal average of $\hat{J}_0^2$ is defined by $\hat{\Gamma}_0 \equiv \int F_0 \hat{J}_0^2 \,\mathrm{d}^3v$. The Fourier representations of $\hat{J}_0$ and $\hat{J}_0^2$ are $J_0(\tau^{1/2} v_\perp k_r)$ and $\Gamma_0(k_r) \equiv \exp(-\tau k_r^2) I_0(\tau k_r^2)$, respectively, with the Bessel function of the first kind J_0 and the modified Bessel function of the first kind I_0. The ion free energy density [55] is

$$E_i = \int \frac{1}{\tau} \frac{(\tau f)^2}{2F_0} \mathrm{d}^3v + \frac{1}{2}\,\phi \frac{1-\hat{\Gamma}_0}{\tau}\phi, \tag{3.30}$$

in which the first term represents the energy of the fluctuations of the gyro-averaged distribution function, and the second one the energy of the gyrophase dependent fluctuations, i.e. the plasma polarisation. Using (3.28), $\partial_t E$ can be written as

$$\begin{aligned}\partial_t \langle E \rangle = \Bigg\langle - \int \Bigg[\nabla \cdot \frac{\boldsymbol{v}_d}{\tau} \frac{K^2}{2F_0} - \left\{ \frac{\boldsymbol{v}_d}{\tau} \cdot \nabla K, n \right\}_{J_0} - \left\{ \frac{\boldsymbol{v}_\parallel}{\tau} \cdot \nabla \tau f, n \right\}_{J_0} + \left\{ \tau f, \frac{\boldsymbol{v}_d}{\tau} \cdot \nabla \phi_0 \right\}_{J_0} \\ + \left\{ n F_0, \frac{\boldsymbol{v}_d}{\tau} \cdot \nabla \phi_0 \right\}_{J_0^2} \Bigg] \mathrm{d}^3v - \frac{1}{2} \left\{ \phi, \dot{\phi} \right\}_{\frac{1-\Gamma_0}{\tau}} + \nabla \cdot (\phi_0 \hat{\chi} \partial_t \boldsymbol{E}_0) \Bigg\rangle \end{aligned} \tag{3.31}$$

with $K \equiv \tau f + J_0 n F_0$. The susceptibility operator $\hat{\chi}$ is defined by its Fourier transform $\chi(k_r) \equiv (1 - \Gamma_0(k_r))/(\tau k_r^2)$. The brackets denote

$$\{a, b\}_K \equiv a\,(K * b) - b\,(K * a)\,, \tag{3.32}$$

with $*$ indicating convolutions. As shown in appendix C.1, $\{a, b\}_K$ can always be written as a divergence, provided the kernel K is symmetric.
The first term on the right hand side of Eq. (3.31) represents the advection of the free energy of gyro-averaged fluctuations by magnetic drifts. The remaining four terms in the integral are FLR corrections (e.g. gyroviscosity) equivalent to the FLR energy-fluxes in Eq. (3.26). The last two terms describe the polarisation energy-flux. They can be expressed as

$$-\chi n\,(\omega k_r n) - v_p \frac{\chi\,|k_r \phi|^2}{2} \frac{\partial \ln \chi}{\partial \ln k_r}, \tag{3.33}$$

where the first term is the gyrokinetic equivalent to the fluid term $-n\nabla\dot{n}$, and the second one is an FLR correction.
Keeping only the lowest order terms, an approximation of the group velocity as in Secs. 3.3.1 and 3.4 can be computed by splitting f and n in (3.30) and (3.31) according to their up-down symmetry, and even and odd terms in $v_\parallel$. One obtains the radial group velocity (App. C.2)

$$\begin{aligned} v_\mathrm{g} = \frac{k_r}{8\sqrt{2}\,(4+7\tau)^{3/2}} \Big[\left(-32 + 24\tau + 586\tau^2 + 1277\tau^3\right) \\ + \frac{1}{4q^2\,(4+7\tau)^2} \left(640 + 8736\tau + 55000\tau^2 + 215268\tau^3 + 560074\tau^4 + 526209\tau^5\right) \Big]. \end{aligned} \tag{3.34}$$

Far from drift and sound resonances, for $k_r \ll 1$, $q \gg 1$, the gyrokinetic equation can be solved alternatively by a power series expansion in terms of k_r and q yielding an identical

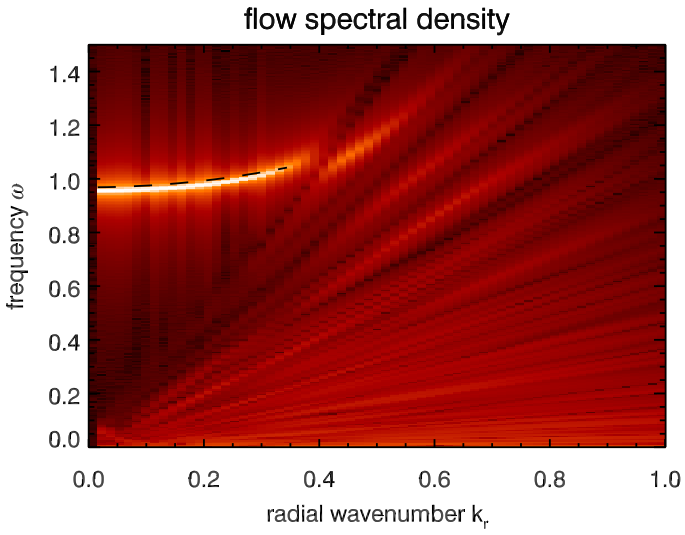

Figure 3.5: GYRO computed log-colour-coded GAM spectrum (Fourier transform of ϕ) for $\tau = 0.5$ and large safety factor $q = 30$. The analytical kinetic frequency (3.34) is indicated by the dashed black line. Due to damping of the resonant modes, the simulated dispersion ends at $k_r \sim 0.4$, as for warm ions the number of resonant particles increases with τ, so that Landau damping has to be taken into account.

result, also in agreement with [34]. The difference between the kinetic (3.34) and the fluid (3.27) group velocity is negligible for $q \to \infty$ (Fig. 3.4) and for $\tau = 0$. For $q \gtrsim 3$ and $\tau \gtrsim 0.2$ the kinetic group velocity tends to be higher than the fluid one (75% at $\tau = 1$, increasing with τ). This is caused by an earlier onset of the coupling to parallel modes due to hot particles.

Computational analyses with GYRO confirm the analytical results obtained from the kinetic and the fluid calculation. The simulations have been performed on a grid of 800 radial, 1 toroidal, 6 orbit and 8 energy gridpoints with a radial box size of $400\rho_{se}$, $0 \leqslant \tau \leqslant 0.5$, and $3 \leqslant q \leqslant 30$. Beforehand, agreement with NLET for cold ions has been checked. An example for $\tau = 0.5$ and $q = 30$ is shown in Fig. 3.5 together with the frequency obtained by integrating Eq. (3.34).

3.6 Magnetic geometry effects

Since magnetic geometry may influence the propagation of GAMs, the effects of plasma shaping on the Poynting flux in general and in the special case of elongated plasmas are discussed in this section. The case of up-down asymmetric flux-surfaces is investigated in the succeeding sections.

Assuming, for simplicity, cold ions, infinite safety factor, and neglecting the polarisation drift, one can approximate Eq. (3.14) at $\theta = \pm\pi/2$ (where $\boldsymbol{k}_r$, $\boldsymbol{v}_d$, and $\boldsymbol{v}_p$ are parallel)

$$n \approx \frac{2v_E}{(\omega - \boldsymbol{k}_r \cdot \boldsymbol{v}_d)\, R} = \frac{2v_E}{R\boldsymbol{k}_r \cdot (\boldsymbol{v}_p - \boldsymbol{v}_d)}, \tag{3.35}$$

in which R is the major radius, and $v_E = k_r\phi_0$ is the $\mathbf{E}\times\mathbf{B}$-drift velocity. For $k_r \ll 1$, equivalent to $v_p \gg v_d$, Eq. (3.35) implies

$$n^2 \approx \frac{4v_E^2}{\omega^2 R^2}\left(1 + \frac{2v_{d,r}}{v_p}\right), \tag{3.36}$$

$v_{d,r}$ being the radial component of $\boldsymbol{v}_d$. Accordingly, the flux-surface averages of the two terms on the right hand side of Eq. (3.16) (the Poynting flux) can be estimated by

$$\frac{1}{2}\left\langle v_{d,r} n^2 \right\rangle \approx \frac{v_d^2}{v_p}\left\langle n^2 \right\rangle = \frac{k_r v_d^2}{\omega}\left\langle n^2 \right\rangle,\ k_r\omega\left\langle n^2 \right\rangle \approx k_r \frac{2v_E^2}{\omega R^2}. \tag{3.37}$$

Since $\langle E \rangle \approx \langle n^2 \rangle$ and $v_d = 1$ in the units defined in 3.3, the group velocity is of order $\mathrm{O}(k_r)$. As the typical velocity scale of turbulent motion is v_{dia}, $v_{dia} \gg v_d$, and $k_r \ll 1$, GAMs generally propagate much slower than turbulence and the magnetic drifts.
The specific magnetic geometry enters the calculation by means of the factors $k_r(\theta)/\omega$ and $k_r(\theta)\omega$ in the neoclassical and the polarisation and FLR fluxes, respectively. Experimentally, only the radial wavenumber at the outboard midplane, k_0, is known. However, the GAM pressure fluctuations, energy-fluxes, and group velocity have to be estimated at $\theta = \pm\pi/2$, where k_r is smaller due to, e.g., ellipticity or Shafranov shift. For an elliptic Miller equilibrium [12], the radial wavenumber at $\theta = \pi/2$ is given by

$$k_r = \frac{1 + \partial_r R}{\kappa + r\partial_r \kappa} k_0, \tag{3.38}$$

where κ is the elongation and r the minor radius at the outboard midplane (r and R refer to the flux-surface center).
Typical values of the geometry parameters are [12] $\partial_r\kappa = (\kappa - 1)/r$, $\partial_r R = -1/3$ and aspect ratio $A = 3.5$. The κ dependence of ω for $k_r = 0$ can be obtained numerically (see 2.4 and [11]) and is rather accurately described for $\kappa = 1..2$ and $q > 1$ by

$$\omega(\kappa) \approx \left(1 + \frac{1}{4q^2}\right)\sqrt{1 + \frac{5}{3}\tau}\,\frac{2.97}{1 + 3.73\kappa}. \tag{3.39}$$

Other possible parametrisations are discussed in Ref. [7]. Substitution of these parameters into Eq. (3.38) yields

$$k_r \approx \frac{2}{3\,(2\kappa - 1)} k_0. \tag{3.40}$$

Multiplying the magnetic drift energy-fluxes (C.5-C.7) with $k_r^2\omega(1)/(k_0^2\omega(\kappa))$ and the polarisation energy-fluxes (C.8-C.12) with $k_r^2\omega(\kappa)/(k_0^2\omega(1))$, and defining $\kappa \equiv 1 + \delta\kappa$, the

following approximations of the group velocities at the outboard midplane are obtained for $\tau = 0$

$$v_{g,r}\left(\delta\kappa\right) \approx \frac{k_0}{0.32 + 2.15\delta\kappa + 5.31\delta\kappa^2 + 5.54\delta\kappa^3 + 2\delta\kappa^4} \left[-0.050 - 0.021\delta\kappa + 0.19\delta\kappa^2 + 0.062\delta\kappa^3 + \frac{0.062 + 0.26\delta\kappa + 0.33\delta\kappa^2 + 0.11\delta\kappa^3}{q^2}\right], \quad (3.41)$$

and $\tau = 1$

$$v_{g,r}\left(\delta\kappa\right) \approx \frac{k_0}{0.32 + 2.15\delta\kappa + 5.31\delta\kappa^2 + 5.54\delta\kappa^3 + 2\delta\kappa^4} \left[0.59 + 1.84\delta\kappa + 1.57\delta\kappa^2 + 0.52\delta\kappa^3 + \frac{0.54 + 2.51\delta\kappa + 3.45\delta\kappa^2 + 1.14\delta\kappa^3}{q^2}\right]. \quad (3.42)$$

Figure 3.6 shows the κ dependence of the group velocity. In the cold ion case, increasing plasma elongation leads to a change of sign of the group velocity when the "neoclassical" fluxes become larger than the polarisation terms. Compared to circular flux-surfaces, the group velocity for warm ions is reduced in elliptic geometry. Therefore, far from resonances, $v_g \sim k_r v_d$ remains small compared to the diamagnetic velocity and the magnetic drift. The cold ion approximation agrees with numerical studies performed with NLET.
However, in single-null configuration near the separatrix, the perturbations vanish at the X-point due to the magnetic null and GAMs are located opposite to the X-point. Consequently, the neoclassical energy-flux is $\langle v_{d,r} n^2\rangle/2 \sim v_d \langle n^2\rangle$ and $v_g \sim v_d$, because the polarisation energy-flux is one order smaller and can be neglected. Hence, independent of the ion temperature, GAMs propagate in the ion magnetic drift direction, which is usually directed towards the X-point, i.e. radially inward. The GAM dispersion must be linear in this case. In the up-down symmetric case, the radial mode structure can show standing waves while in up-down asymmetric geometry propagating waves are expected as the wave numbers of incoming and reflected wave at a cutoff layer are different.

3.7 Influence of up-down asymmetry

In the previous sections the energy-flux of GAMs has been shown to consist of two kinds of transports, the advection of free energy with the magnetic inhomogeneity drift (curvature, ∇B) and the polarisation energy-flux. In case of up-down symmetric plasma equilibria the magnetic inhomogeneity fluxes are of order $k_r \rho_{se} v_d E_{fluc}$ due to neoclassical cancellation effects, where v_d is the sum of curvature and ∇B drifts and E_{fluc} is the energy of the fluctuations. Since the polarisation fluxes are also of order $k_r \rho_{se} v_d E_{fluc}$ and opposite to the curvature energy-flux, the observed group velocities are much smaller than v_d. In this section, the geometry analysis is generalised to up-down asymmetric magnetic geometries including a model for single-null configuration. In these cases, the curvature energy-fluxes

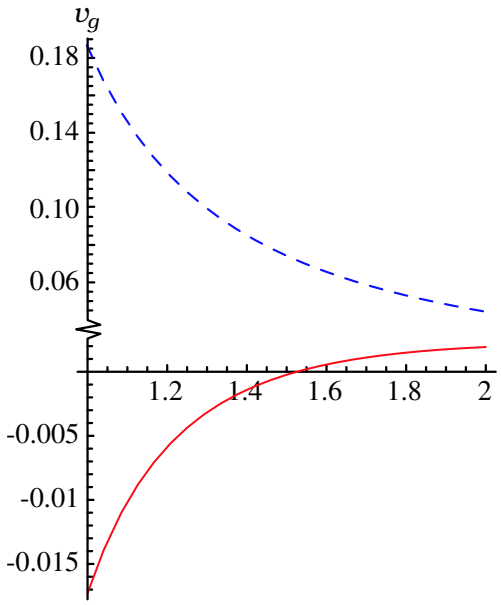

Figure 3.6: Estimates of the radial group velocities for $k_r = 0.1$, $\tau = 0$ (solid) and $\tau = 1$ (dashed) plotted against the elongation κ.

can be of order $v_d E_{fluc}$ since the asymmetry removes the neoclassical cancellation, and larger group velocities of order v_d and above are expected.
Here as well as in the following, r is defined as the minor radius of a particular flux-surface at the outboard midplane, which makes r a flux-surface label. Thus, k_r is the wavenumber and v_r the velocity with respect to the coordinate r.

3.7.1 Fluid model

The units used in the following are in principle analogous to those of the previous sections. However, due to the magnetic geometry, the definitions of Sec. 3.3 are defined more precisely such that the magnetic drift velocity equals unity *at the outboard midplane*. Density n, ion and electron temperature T_i and T_e, and electric potential perturbations ϕ are normalised to $\rho^\star n_0$, $\rho^\star T_{0,i/e}$, $\rho^\star T_{0,e}/e$, respectively, where the subscript 0 indicates the corresponding background value and $\rho^\star$ is given by ρ_{se}/R_0 with the major torus radius *at the outboard midplane* R_0, $c_{se} \equiv (T_{0,e}/m_i)^{1/2}$, and $\rho_{se} \equiv (m_i c_{se}) / (eB_0)$ with the magnetic field *at the outboard midplane* B_0. The time scale is $t_0 \equiv R_0/(2c_{se})$.
The evaluation of the time derivative of the total free energy for the cold ion equation (3.14) in general geometry yields:

$$\partial_t \langle E \rangle = \left\langle -\nabla \cdot \left(\frac{\boldsymbol{v}_d n^2}{2} \right) + \nabla \cdot \frac{(n \nabla \dot{n})}{B_{rel}^2} + \nabla \cdot \frac{\left(n \nabla \dot{\phi}_0 \right)}{B_{rel}^2} \right\rangle , \tag{3.43}$$

where $\boldsymbol{v}_d$ is the sum of curvature and ∇B-drift, and $B_{rel} \equiv B/B_0$. The additional factor

$1/B_{rel}$ appears because the polarisation related terms in Eq. (3.16) implicitly contain a factor ρ_i^2 (normalised to its value at the outboard midplane). The flux-surface average in general geometry is defined by $A_0 \equiv \langle A \rangle \equiv (\oint B^{-1}\,\mathrm{d}l_\parallel)^{-1} \oint AB^{-1}\,\mathrm{d}l_\parallel$, where $\mathrm{d}l_\parallel$ denotes the line element parallel to the magnetic field. With adiabatic electrons, $\phi = \phi_0 + n$ and $n_0 = 0$ still hold.

The first term on the right hand side of Eq. (3.43) is the flow of the energy of the electron pressure perturbations in the ion magnetic drift direction. The second term is a polarisation energy-flux, which can be interpreted as an hydraulic energy-flux, $p_e \boldsymbol{v}_{pol}$, consisting of the electron pressure and the polarisation drift velocity. A detailed discussion of the two terms can be found in Sec. 3.3.1. The term $n\nabla\dot{\phi}_0/B_{rel}^2$ appearing in Eq. (3.43) is an additional component of the polarisation energy-flux caused by the *flux-surface averaged* potential ϕ_0, and vanishes for up-down-symmetric magnetic geometries. Since the kinetic energy of the poloidal rotation $\nabla\phi_0 = ik_r\phi_0$, does not vanish for $k_r \to 0$, this term contributes to the Poynting flux of GAMs for $k_r = 0$.

In Sec. 3.6, the density perturbation for $k_r \ll 1$ was approximated by

$$n^2 \approx \frac{4v_E^2}{\omega^2 R^2}\left(1 + \frac{2v_{d,r}}{v_p}\right) \tag{3.44}$$

with the $\mathbf{E}\times\mathbf{B}$-drift velocity v_E, the radial component of the magnetic inhomogeneity drift $v_{d,r}$, the major radius R and the GAM phase velocity v_p. Whereas in circular geometry, the first term in Eq. (3.44) and the last term on the right hand side of Eq. (3.43) do not contribute to the flux-surface averaged energy-flux – implying zero group velocity for $k_r = 0$ – in general geometry, they can give rise to a non-vanishing $v_g(k_r = 0)$ and can be much larger than the k_r-dependent part of the polarisation energy-flux, $n\nabla\dot{n}/B_{rel}^2$.

Circular flux-surfaces [12] augmented with an r-dependent vertical shift $Z_0(r)$, i.e. $R(r,\theta) = R_0 + r\cos(\theta)$ and $Z(r,\theta) = Z_0(r) - r\sin(\theta)$, may serve as the most straightforward test of up-down asymmetric geometry in numerical studies. The Z-shifted geometry is the simplest modification of the circular equilibrium which shows the basic effects of up-down asymmetry while avoiding the complexity of force-free asymmetric configurations. Lacking complete consistency, it can be thought of as being maintained by a conductor inside the considered flux-surface. The dependence of $v_g(k_r = 0)$ on the differential Z-shift $s_z \equiv \partial_r Z_0$ (which can take values between -1 and 1) was studied for cold ions and infinite safety factor using the two fluid code NLET [14], the gyrokinetic codes GS2 [46] and GYRO [15], and direct numerical solutions of the GAM equation.

A GAM spectrum computed with NLET, in which v_d is parallel to the Z-axis, for $s_z = 0.3$ is shown in Fig. 3.7. As an effect of the additional k_r-independent terms in the group velocity, the extremum of the GAM dispersion is shifted away from $k_r = 0$. The group velocity at $k_r = 0$ is positive. Thus, as conjectured in Sec. 3.6, $v_g(k_r = 0) \neq 0$ due to the up-down asymmetry of the flux-surfaces. Note also the deformation of the spectral lines of the magnetic drift modes due to the up-down asymmetry. It arises due to the localisation of the drift modes (see Sec. 3.3.2) and the θ-dependence of their radial wave number.

The group velocity at $k_r = 0$ is rather accurately linear in $(1 + |s_z|)/(1 - |s_z|)$ (Fig. 3.8), the ratio of the inverse flux-surface distances at the poloidal positions of the maximum

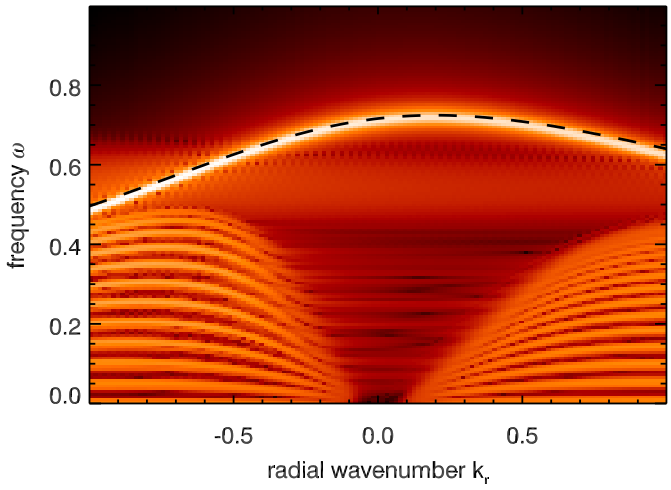

Figure 3.7: NLET computed log-colour-coded GAM spectrum (Fourier transform of ϕ) for $\tau = 0$, $q = 100$, and $s_z = 0.3$ with direct numerical solution of the GAM equations (dashed). The extremum of the GAM dispersion is shifted along the k_r-axis due to the up-down asymmetric magnetic geometry.

and the minimum of the poloidal magnetic field, i.e. $|\nabla r(\theta = \pi/2)|/|\nabla r(\theta = -\pi/2)|$ for $s_z > 0$. This implies $v_g(k_r = 0) \to \infty$ for $s_z \to 1$.
A very realistic up-down asymmetric magnetic geometry can be constructed with the magnetic field of three toroidal current loops, representing the plasma current and the currents of two coils, used to elongate the plasma and to generate separatrices. For large aspect ratios, the corresponding vector potentials are given by $A_i = a_i/2 \ln((R_0 + R)^2 + (Z + z_i)^2)$ where a_i measures the current and z_i the position of conductor i on the Z-axis. Since, due to axisymmetry, equipotential surfaces of the vector potential (of the poloidal field) are also surfaces of constant poloidal flux, the flux-surface shape is determined by the condition $\sum_{i=0}^{2} A_i = \Psi = const.$ with $\Psi_{max} \equiv \Psi$ for the last closed flux-surface. In order to assure that the vertical forces on the flux-surface balance to zero, $a_1 = ma_2$ and $z_1 = -mz_2$ with a real factor $m > 0$. The necessary geometry data can then be calculated analogous to an ordinary Miller equilibrium (see Sec. 2.1.3 and Ref. [12]). As in Miller geometry r is defined as the minor radius of a particular flux-surface at the outboard midplane. The corresponding value at the separatrix is referred to as r_{max}.
In this geometry, $(1 + |s_z|)/(1 - |s_z|)$ corresponds to $x \equiv |\nabla r(\theta = -\pi/2)|/|\nabla r(\theta = \pi/2)|$. Thus, the separatrix geometry can be compared to the shifted circular geometry by plotting v_g versus $s_z \equiv (x - 1)/(x + 1)$ (Fig. 3.9). The group velocity at $k_r = 0$ obtained from the numerical solution of the GAM equations for $a_0 = 1$, $z_0 = 0$, $a_1 = 2a_2 = 2$, $z_1 = -2z_2 = 2$ is positive. The values of s_z for which v_g is plotted correspond to $r = (0.055...0.999)\, r_{max}$. For small s_z, the group velocities of the shifted circular and the separatrix geometry are of the same order, but for $s_z \to 1$ the latter stays finite whereas the former diverges.
An estimate of the group velocity for $\tau > 0$ and large safety factor can be derived by

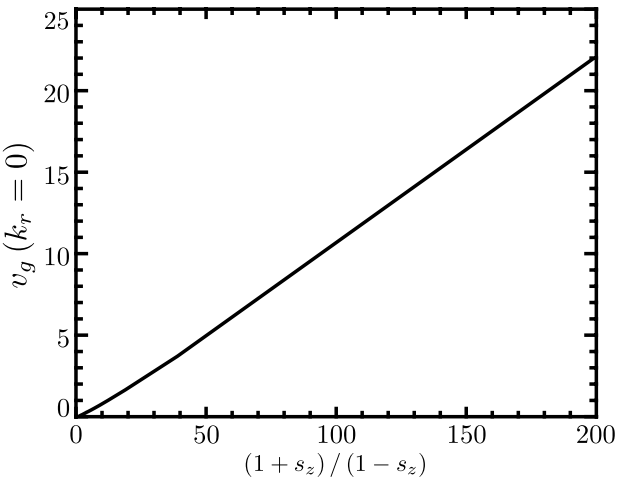

Figure 3.8: GAM group velocity $v_g(k_r = 0)$ in shifted Miller geometry plotted against $(1+s_z)/(1-s_z)$. For $s_z \to 1$, the ratio $(1+s_z)/(1-s_z)$ diverges, implying $v_g(k_r = 0) \to \infty$.

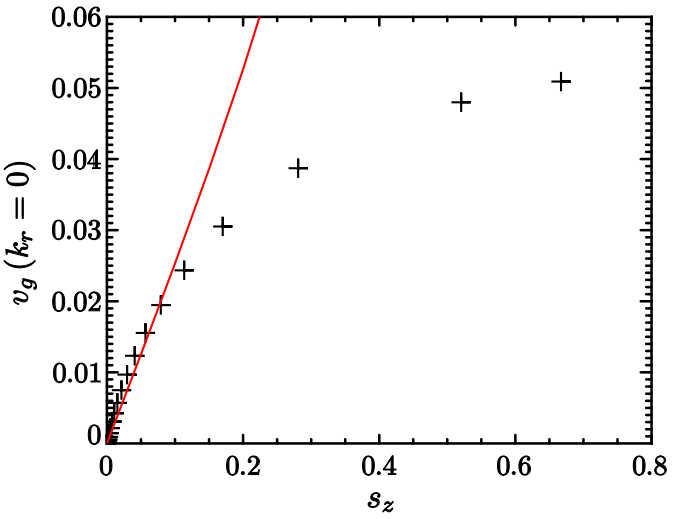

Figure 3.9: GAM group velocity $v_g(k_r = 0)$ in single-null (crosses) and shifted Miller geometry (solid) plotted against s_z. When approaching the X-point, i.e. $s_z \to 1$, the single-null group velocity approaches a finite maximum, while v_g diverges in case of the Miller equilibrium with Z-shift.

evaluating the two-fluid Poynting flux for warm ions and infinite safety factor. This in turn is obtained by a straightforward modification of Eq. (3.26) to general geometry – analogous to Eq. (3.43) – and adding the third term on the right hand side of Eq. (3.43). In the infinite safety factor limit, all terms involving $\boldsymbol{v}_{\|} \cdot \nabla$ can be neglected, and since $k_\theta \ll k_r$ for GAMs, only the radial component of $\nabla_\perp$ has to be considered. In flux coordinates using the normalisation defined at the beginning of this section, $\nabla_\perp$ can be written as $\gamma \partial_\Psi \equiv \gamma_{rel} \partial_r$. Here, Ψ is the poloidal flux, $\gamma \equiv |\nabla \Psi|$, γ_0 is the value of γ at the outboard midplane, and $\gamma_{rel} \equiv \gamma / \gamma_0$. The partial derivative ∂_r corresponds to ik_r in Fourier space, where k_r is the minor radial wave number at the outboard midplane. Thus, the radial component of the curvature operator $\hat{C} \equiv -\boldsymbol{v}_d \cdot \nabla$ is $-v_{d,r} \partial_r$ with

$$v_{d,r} \equiv \gamma_{rel} \boldsymbol{v}_d \cdot \frac{\nabla \Psi}{|\nabla \Psi|} = \frac{R_0 \gamma_{rel}}{B_{rel}} \left(\hat{\boldsymbol{b}} \times \nabla \ln B \right) \cdot \frac{\nabla \Psi}{|\nabla \Psi|}. \tag{3.45}$$

The ordering $k_r \phi_0 \sim n \sim T_i \sim E_{fluc}^{1/2}$ is applied and only Poynting fluxes of order $v_d E_{fluc}$ are retained. Assuming constant ion entropy, $T_i \approx 2n/3$, and neglecting polarisation effects, $n \approx (v_{d,r} k_r \phi_0)/\omega$, where $\omega \approx \omega(k_r = 0) \approx ((1 + 5\tau/3)/2)^{1/2}$. The total free energy of the GAM is $E \approx k_r^2 \phi_0^2 \langle \gamma_{rel}^2 / B_{rel}^2 \rangle$. Combining everything, one obtains the group velocity

$$v_g(\tau) \approx \frac{\left(1 + \frac{5\tau}{3}\right)^2 + \frac{10\tau^2}{9}}{\left(1 + \frac{5\tau}{3}\right)} \left\langle v_{d,r}^3 \right\rangle_g + \frac{11\tau}{12} \left\langle \frac{\gamma_{rel}^2 v_{d,r}}{B_{rel}^2} \right\rangle_g - \left(1 + \frac{5\tau}{3}\right) \left\langle \frac{\gamma_{rel}^2 v_{d,r}}{B_{rel}^2} \right\rangle_g, \tag{3.46}$$

where $\langle \dots \rangle_g \equiv \langle \gamma_{rel}^2 / B_{rel}^2 \rangle^{-1} \langle \dots \rangle$. The first term on the right hand side of Eq. (3.46) corresponds to the first term in Eq. (3.43), the second term is a finite Larmor radius (FLR) correction to the first one, and the third term corresponds to the polarisation energy-flux $n \nabla \dot{\phi}_0 / B_{rel}^2$ in Eq. (3.43).

With large aspect ratio and small s_z, $v_{d,r} \approx -\sin(\theta)(1 + s_z \sin(\theta))$ and $\gamma_{rel} \approx (1 - s_z \sin(\theta))^{-1}$. Thus, to first order in s_z one obtains $\langle v_{d,r}^3 \rangle_g \approx -3 s_z / 4$ and $\langle \gamma_{rel}^2 v_{d,r} / B_{rel}^2 \rangle_g \approx -s_z$.

As mentioned before, the parameters a_i and z_i of the separatrix geometry have been chosen such that the vertical magnetic forces on the central current loop (i.e. the flux-surfaces) balance, which corresponds to the condition $F_Z = \iint p_\perp \hat{\rho}_Z \, \mathrm{d}f = 0$ on each flux-surface. Here, $p_\perp = B^2/(2\mu_0)$ is the perpendicular component of the magnetic pressure, $\hat{\rho}_Z$ the vertical component of the flux-surface normal vector, and $\mathrm{d}f$ is an infinitesimal flux-surface element. This can be reduced to $\oint \gamma^2 \partial_\| \ln R \, \mathrm{d}l_\| = 0$. With $v_{d,r} = F B_0 R_0 / \gamma_0 (\partial_\| \ln B)/B$, one obtains

$$\left\langle \frac{\gamma_{rel}^2 v_{d,r}}{B_{rel}^2} \right\rangle = \frac{1}{\oint B^{-1} \mathrm{d}l_\|} \frac{F B_0^3 R_0}{\gamma_0^3} \oint \frac{\gamma^2}{B^4} \partial_\| \ln B \, \mathrm{d}l_\|. \tag{3.47}$$

For large aspect ratio, B is approximately constant and, due to $q \gg 1$, $\partial_\| \ln B \approx -\partial_\| \ln R$. Thus, the second integral on the right hand side of Eq. (3.47) reduces to the force-balance condition.

Therefore, $\langle \gamma_{rel}^2 v_{d,r} / B_{rel}^2 \rangle_g \approx 0$ in contrast to the shifted-circle geometry. This implies that for $k_r = 0$, the energy of GAMs is transported essentially by the magnetic drift energy-flux $v_d E_{fluc}$. In case of vertical force-balance this result agrees with the conjecture in Sec. 3.6,

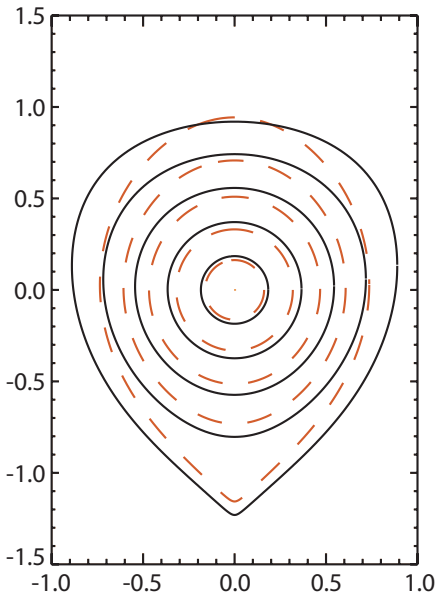

Figure 3.10: Single-null geometries computed with the model described in Sec. 3.7.1 for $\Psi = [0.2, 0.4, 0.6, 0.8, 0.999]\Psi_{max}$. Compared to the flux-surface shape obtained with two shaping coils (dashed), the flux-surfaces obtained with four coils (solid) are compressed at the top, which leads to an enhanced group velocity of the GAM compared to Fig. 3.9.

that in single-null geometry $v_g(k_r = 0)$ has the sign of $v_{d,r}$ at the position opposite to the X-point. However, with low aspect ratio, when the variation of B across the flux-surface cannot be neglected any longer, the remaining two terms in Eq. (3.46) might be significant.

Numerical calculations suggest that for large aspect ratio one can approximate the geometry coefficient $\langle v_{d,r}^3 \rangle_g$ by $0.028(1 - (s_z - 1)^4)^{-1/2}$ for $a_0 = 1$, $z_0 = 0$, $a_1 = 2a_2 = 2$, and $z_1 = -2z_2 = 2$.

In order to have high GAM group velocity, the magnetic geometry should have a maximum of the poloidal magnetic field – corresponding to the flux-surfaces being close to each other – at a poloidal position where the magnetic inhomogeneity drift has a significant radial component. In case of the single-null geometry in Sec. 3.7.1, this could be realised by adding an indentation coil – with a current opposite to the elongation currents – close to the plasma column opposite to the X-point. Instead of one upper coil, one has three upper shaping coils: the indentation coil opposite to the X-point and and two coils at each side of the indentation coil assuring the force balance. Preliminary studies easily yield a group velocity three times larger that way. In Fig. 3.10, this geometry is compared to the conventional single-null geometry discussed before, which only needs two shaping coils. The indentation coil presses the flux surfaces closer to each other, such that the asymmetry in the flux-surface distances at and opposite to the X-point is larger.

3.7.2 Gyrokinetic model

To elaborate the analogies between gyrokinetic and two-fluid theory, the linear gyrokinetic framework (3.28) already used in Sec. 3.5 is used again in the following. As in the previous sections, only cases, in which the parallel ion dynamics can be neglected, i.e. high safety factors q, are considered. In practice, this is hardly a restriction because modes lose the character of a GAM due to resonances with sound-waves at low q (see Sec. 3.3 and [11]). For effects of finite orbit width (FOW) on GAMs in that regime see e.g. Ref. [58].
With arbitrary geometry but infinite safety factor and the conventions of Sec. 3.5, the expression for $\partial_t \langle E \rangle$ is given by:

$$\begin{aligned}\partial_t \langle E \rangle = \Bigg\langle - \int \Bigg[& \nabla \cdot \frac{\boldsymbol{v}_d}{\tau} \frac{K^2}{2F_0} - \left\{ \frac{\boldsymbol{v}_d}{\tau} \cdot \nabla K, n \right\}_{\hat{J}_0} \\ & + \left\{ \tau f, \frac{\boldsymbol{v}_d}{\tau} \cdot \nabla \phi_0 \right\}_{\hat{J}_0} + \left\{ n F_0, \frac{\boldsymbol{v}_d}{\tau} \cdot \nabla \phi_0 \right\}_{\hat{J}_0^2} \Bigg] \mathrm{d}^3 v \\ & - \frac{1}{2} \left\{ \phi, \dot{\phi} \right\}_{\frac{1-\hat{\Gamma}_0}{\tau}} + \nabla \cdot (\phi_0 \hat{\chi} \partial_t \boldsymbol{E}) \Bigg\rangle . \end{aligned} \tag{3.48}$$

As in section 3.7.1, one can write the curvature operator $\boldsymbol{v}_d \cdot \nabla$ as $v_{d,r} \partial_r$ with the appropriate kinetic expression for $v_{d,r}$ when evaluating Eq. (3.48). The operators $\hat{J}_0$, $\hat{\Gamma}_0$ and $\hat{\chi}$ are defined by their Fourier transforms (using flux coordinates and the normalisation given in Sec. 3.7.1). The gyro-average $\hat{J}_0$ corresponds to $J_0(\tau^{1/2} v_\perp k_r \gamma_{rel} / B_{rel})$, the thermal average of $\hat{J}_0^2$, $\hat{\Gamma}_0$, to $\Gamma_0(k_r) \equiv \exp(-\tau k_r^2 \gamma_{rel}^2 / B_{rel}^2) I_0(\tau k_r^2 \gamma_{rel}^2 / B_{rel}^2)$, and the susceptibility operator $\hat{\chi}$ to $\chi(k_r) \equiv (\gamma_{rel}^2 / B_{rel}^2)(1 - \Gamma_0)/(\tau k_r^2)$ with the Bessel function of the first kind J_0 and the modified Bessel function of the first kind I_0.
The first term on the right hand side of Eq. (3.48) represents the advection of the free energy of gyro-averaged fluctuations by magnetic drifts. It is the equivalent to the first term on the right hand side of Eq. (3.43). Since $k_r \phi_0 \sim n \sim E_{fluc}^{1/2}$, this energy-flux is of order $v_d E_{fluc}$. The remaining three terms in the integral are FLR corrections. As J_0 is $O(k_r^2)$ in the commutator brackets, those terms correspond to energy-fluxes of order $k_r \rho_{se} v_d E_{fluc}$ and will therefore be neglected. The last two terms describe the polarisation energy-flux.
Different from Eq. (3.31), the very last term contains the entire electric field instead of its flux-surface average. Analogous to Eq. (3.33) the polarisation energy-flux can be expressed as

$$- \frac{\gamma_{rel}^2 \chi}{B_{rel}^2} \left[k_r \omega \left(\phi_0 n + n^2 \right) + v_p \frac{\chi \left| k_r \phi \right|^2}{2} \frac{\partial \ln \chi}{\partial \ln k_r} \right] . \tag{3.49}$$

Since χ is $O(1)$ and $v_p \chi (\partial \ln \chi / \partial \ln k_r) = \omega (\partial \chi / \partial k_r)$ is $O(k_r)$, only the very first term in Eq. (3.49) contributes to $v_g(k_r = 0)$. In Sec. 3.5 this term vanished due to flux-surface symmetry. It can therefore be considered as the equivalent of the additional polarisation flux in Eq. (3.43).
The τ-dependence of $v_g(k_r = 0)$ for the shifted circular flux-surfaces defined in section 3.7.1 has been studied using the gyrokinetic codes GS2 [46] and GYRO [15]. The plot of $v_g(k_r = 0)$ for $s_z = 0.3$ and 0.5 against τ (Fig. 3.11) illustrates that the additional

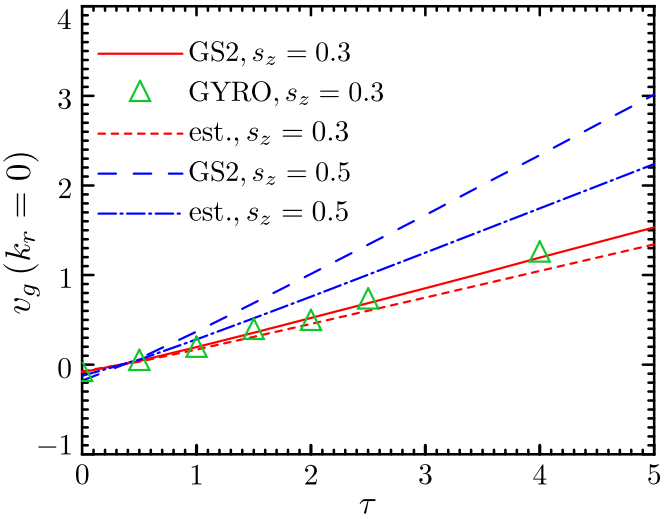

Figure 3.11: GAM group velocity – computed with GS2, GYRO and with the estimate (3.46) – at $k_r = 0$ for $s_z = 0.3$ and $s_z = 0.5$ vs. the ratio of ion to electron temperature τ. Since contrary to NLET, GS2 and GYRO take v_d to be in negative Z-direction, one has to compare the results with Eq. (3.46) for $s_z \to -s_z$.

polarisation flux discussed here [see Eq. (3.49)] and in section 3.7.1 exceeds the energy-flux due to the magnetic inhomogeneity drift in the cold ion case. When the ion temperature is increased ($\tau \gtrsim 0.3$) gyroradius effects overcompensate this effect such that the group velocity changes sign and behaves as suggested in Sec. 3.6. This behavior and the order of magnitude of v_g is quite well reproduced by the two-fluid approximation (3.46).

Chapter 4

GAMs in two-fluid and gyrokinetic simulations

Since, in general, fluid simulations require significantly less computational resources than gyrokinetic ones, it would be convenient to apply only fluid theory in numerical studies. However, there are effects like particle trapping or collisionless damping that are not contained in conventional fluid theory and may have an important influence on the result of the computations. Therefore, it is important to make sure that purely kinetic effects are sub-dominant for the problem under consideration such that one can safely assume that the results of fluid theory differ only quantitatively from kinetic calculations.

Since GAMs are mainly observed in the edge of tokamak plasmas, it seems reasonable to assume that GAMs and their interaction with turbulence is adequately described by two-fluid theory (see Sec. 2.2.3). In Chap. 3, where the linear properties of the geodesic acoustic mode have been studied, good agreement between gyrokinetic and two-fluid codes has been found. In order to back up the previous statement in case of nonlinear simulations, the two-fluid code NLET [14] and the gyrokinetic codes GYRO [15] and (to a limited extent) GS2 [46] are compared for three different parameter sets.

The first parameter set to be studied is the Cyclone base case [59, 60], which is the standard set for comparisons between kinetic plasma codes. Therefore, it is the natural starting point for a comparison between the two-fluid code NLET and gyrokinetic codes. The parameters of the Cyclone base case are based upon a real discharge of the DIII-D tokamak, however, with idealised physics. The background electron and ion temperatures are assumed to be equal, $\tau = T_{i,0}/T_{e,0} = 1$, the electron response is adiabatic and the plasma is in the electrostatic limit, collisions are neglected. Only one ion species is considered. The flux-surfaces are assumed to have circular $s - \alpha$ flux-tube geometry. The inverse aspect ratio $\epsilon = r/R$, where r is the local minor radius and R the major radius at the flux-surface centre, is $\epsilon = 0.18$. The safety factor is $q = 1.4$ and the global shear is $s_g = 0.786$. The normalised background density gradient, that is the ratio of the major radius to the density gradient scale length $L_n \equiv -(\mathrm{d}n/\mathrm{d}r)/n$ is $R/L_n = 2.2$. The analogously defined normalised temperature gradient is $R/L_T = 6.9$. The centre of the simulation domain is at $r/a = 0.5$, where a is the minor radius of the separatrix. The local limit is applied,

	Cyclone base case	**GAM case 1**	**GAM case 2**
ϵ	0.18	0.1	0.1
r/a	0.5	0.5	0.5
$\rho^\star$	$4 \cdot 10^{-3}$	$1.739 \cdot 10^{-5}$	$4.4 \cdot 10^{-6}$
R/L_T	6.9	27.27	113.64
R/L_n	2.2	9.09	22.73
L_T/L_n	3.14	3.0	5.0
τ	1	1	1
s_g	0.786	1	1
q	1.4	5	5

Table 4.1: Parameter sets for the comparison of NLET, GYRO and GS2.

i.e. $\rho^\star \equiv \rho_{se}/a = 4 \cdot 10^{-4} \ll 1$. Due to this choice of the parameters, especially the low safety factor and the shallow gradients, the situation represented by the cyclone base case corresponds to the core of a tokamak plasma.

The Cyclone base case parameters are then modified in order to represent the physical situation at the tokamak edge. The safety factor is increased to $q = 5$. The gradients are steeper: $R/L_T = 27.27$ and $R/L_n = 9.09$ in one parameter set, and $R/L_T = 113.64$ and $R/L_n = 22.73$ in another one. The corresponding ratios of the density to the temperature gradient scale lengths are $L_n/L_T = 3.0$ and $L_n/L_T = 5.0$. The ratios of the sound Larmor radius to the minor radius of the separatrix are $\rho^\star = 1.739 \cdot 10^{-5}$ and $\rho^\star = 4.4 \cdot 10^{-6}$, respectively. The shear is set to $s_g = 1$ and τ remains 1. In order to reduce the influence of trapped particles, a potential source of discrepancies between gyrokinetic and fluid codes, the inverse aspect ratio is reduced to $\epsilon = 0.1$. The parameters of those three parameter sets are summarized in Tab. 4.1.

For convenience, the units used in this chapter differ from those in Chap. 3. Instead, the normalisation used by GYRO is preferred. Therefore, the frequency is normalised to the ratio of the thermal sound velocity c_{se} (as defined in Chap. 3) to the minor radius of the separatrix a. The radial wave number, however, is still normalised to the sound Larmor radius ρ_{se}. Heat fluxes are measured in gyro-Bohm units $Q_{\mathrm{GB}} = n_0 T_0 c_{se} \rho^{\star 2}$.

Although the Cyclone base case is originally intended for the numerical study of tokamak-core turbulence, which is actually not the scope of this thesis, it is worth to be discussed for two reasons. First, by comparing NLET and GYRO for Cyclone base case parameters here, NLET results can immediately be compared to the results published in many other benchmark studies using Cyclone base case parameters. And second, GAMs are expected to be absent for core parameters but to be the dominant zonal flow for edge parameters. Thus, a transition from zero frequency zonal flows in the core to oscillating GAMs in the edge is expected to be observed when going from cyclone base case parameters to the edge parameters given in Tab. 4.1. Even if the results of GYRO and NLET may not match quantitatively, they should nevertheless produce qualitatively equivalent results.

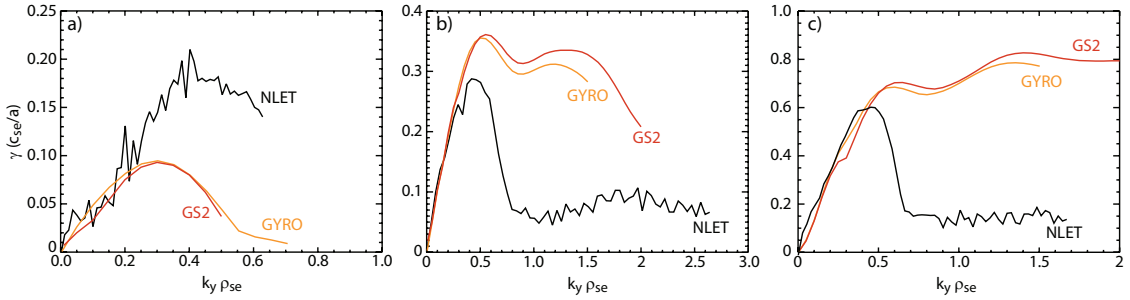

Figure 4.1: Growthrates computed with NLET, GYRO and GS2 for the parameter sets given in Tab. 4.1. a) Cyclone base case. b) GAM case 1. c) GAM case 2. The fluid growth rate in a) is higher than those of the two gyrokinetic codes for $k_y\rho_{se} \gtrsim 0.2$. In cases b) and c) the growth rates of the three codes agree reasonably well. The quench of the fluid growth rate at $k_y\rho_{se} \approx 0.5$ is a result of the fluid approximation, which excludes perturbations at the gyro radius scale and smaller.

The first quantity to be considered in a proper benchmark of plasma turbulence codes is the growth rate of instabilities. The growth rates are obtained from code runs solving the linearised gyrokinetic or fluid equations, initialised with small random perturbations upon a large density and temperature background. The results for the growth rates for $k_r\rho_{se} = 0$ are summarized in Fig. 4.1. In all three cases, the growth rates calculated with GYRO and GS2 are in very good agreement. The growth rate obtained with NLET also agrees with the gyrokinetic results, at least for small wave numbers k_y. However, the growth rate obtained with NLET for the Cyclone base case, is larger than the gyrokinetic result for wave numbers $k_y\rho_{se} > 0.2$. Since the aspect ratio in the Cyclone base case is about half the value used in the two GAM cases, this discrepancy might be due to the increased importance of trapped particles. It could also be caused by collisionless damping effects, which are more important in core-turbulence simulations than for edge parameters, for which the growth rates of all three codes agree very well for small wave numbers $k_y\rho_{se}$. Differences in the growth rates arising from collisionless effects can be compensated by adapting the parallel heat conduction coefficients in NLET, which partly account for e.g. Landau damping. The sudden quench of the fluid growth rates at $k_y\rho_{se} \approx 0.5$ is a typical feature of the fluid approximation, which excludes fluctuations at the gyro radius scale and smaller.

Since the linear calculations do not reveal significant and unforeseen differences between the tested fluid and gyrokinetic codes, one can be confident that NLET and GYRO deliver equivalent results for small k_y in the linear case, and one can continue and compare the nonlinear behaviour of the two codes.

When comparing the nonlinear results of NLET and GYRO, aiming at the investigation of geodesic acoustic modes, it is important in first place, that both codes display qualitatively equivalent turbulence and zonal flow behaviour. Numerical differences may often be explained by conceptual differences between gyrokinetic and two-fluid theory or by specific features of the turbulence codes. But it is indispensable for example that in both codes

Parameters	**Code**	L_r (ρ_{se})	L_y (ρ_{se})	n_r	n_y	$\langle v_E \rangle$ (v_d)	Q (Q_{GB})
Cyclone base case	NLET	114	140	320	320	1.54	4.29
	GYRO	114	140	114	16	1.54	3.17
GAM case 1	NLET	150	150	512	512	9.52	11.06
	GYRO	150	150	304	64	24.01	12.06
GAM case 2	NLET	150	150	1024	1024	34.51	211.49
	GYRO	150	150	500	64	45.51	69.85

Table 4.2: Domain and grid sizes as well as RMS amplitudes of the flux-surface averaged $\mathbf{E} \times \mathbf{B}$ flow (in units of the magnetic inhomogeneity drift) and heat flux (in gyro-Bohm units) for the code runs used for Figs. 4.2, 4.3, and 4.4.

the turbulence excites zonal flows for core parameters and GAMs for edge parameters. This transition from stationary zonal flows to GAMs can be tested with the parameter sets defined before.

For the following comparison, numerical turbulence studies using a variety of grid sizes and computational domains were performed. However, the gyrokinetic results for the cyclone base case are mainly based upon a run with a computational domain of $L_r \times L_y = 114\rho_{se} \times 114\rho_{se}$ with a grid of 114 radial points and 16 toroidal modes. The corresponding fluid simulations, used equivalent domain sizes with various resolutions. The simulations for the two GAM parameter sets mainly used domains of $150\rho_{se} \times 150\rho_{se}$. The gyrokinetic code runs were performed primarily with 64 toroidal modes. The radial grid sizes ranged from 128 up to 700 points. The fluid simulations used grid sizes from 128^2 up to 1024^2. The domain and grid sizes as well as the RMS amplitudes of the heat flux and the flow velocity for the simulations used for Figs. 4.2, 4.3, and 4.4 are summarized in Tab. 4.2.

The turbulence intensity, which may be measured by the turbulent radial heat flux, in the stationary state is discussed first. The flux-surface averaged heat fluxes for the given parameters are plotted versus time in Fig. 4.2. For better comparability, NLET and GYRO heat fluxes for each parameter set are arranged next to each other, and the average heat fluxes of both codes are indicated in each plot.

For Cyclone base case parameters, the average heat fluxes agree reasonably well. The fluid heat flux is about 26% smaller compared to the gyrokinetic result thereby confirming the result of an earlier comparison in Ref. [61]. However, the gyrokinetic heat flux drops to a value of 4.07 upon increasing the number of toroidal modes to 64, thus reducing the difference a bit.

The agreement between the heat fluxes for the parameters of GAM case 1 is better. The difference between the two code runs shown in 4.2 is only 8%. The corresponding computational domains had an extent of $150\rho_{se} \times 150\rho_{se}$ with 304 radial points and 64 toroidal modes in case of GYRO and 512^2 points in case of NLET. However, the gyrokinetic heat flux fluctuates a bit between runs with varying numbers of radial grid points. For radial grid sizes of 180, 256, 304 and 500, the corresponding average heat fluxes are 11.97, 11.52,

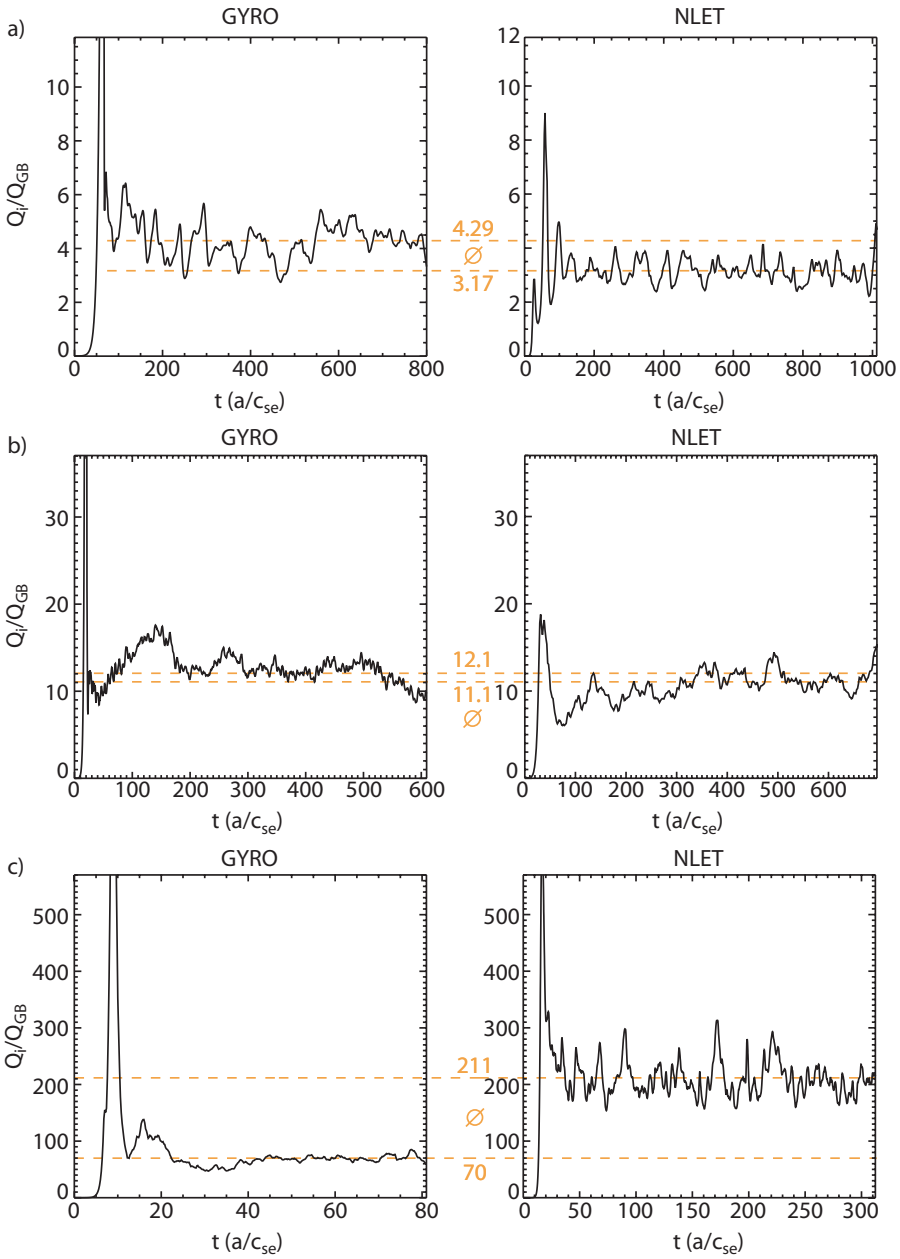

Figure 4.2: Radially and flux-surface averaged heat fluxes vs. time. The time averaged heat fluxes are indicated by dashed lines. a) Cyclone base case. b) GAM case 1. c) GAM case 2. The heat fluxes in a) agree reasonably well; the fluid result is about 26% smaller than the gyrokinetic result. The agreement is better in b), where the difference is only 8%. In case c) with the steepest gradients, the fluid heat flux is about a factor of 3 larger than the gyrokinetic value, presumably due to the overestimated collisionless damping of the GAM by the NLET parameters or the neglect of collisions in GYRO.

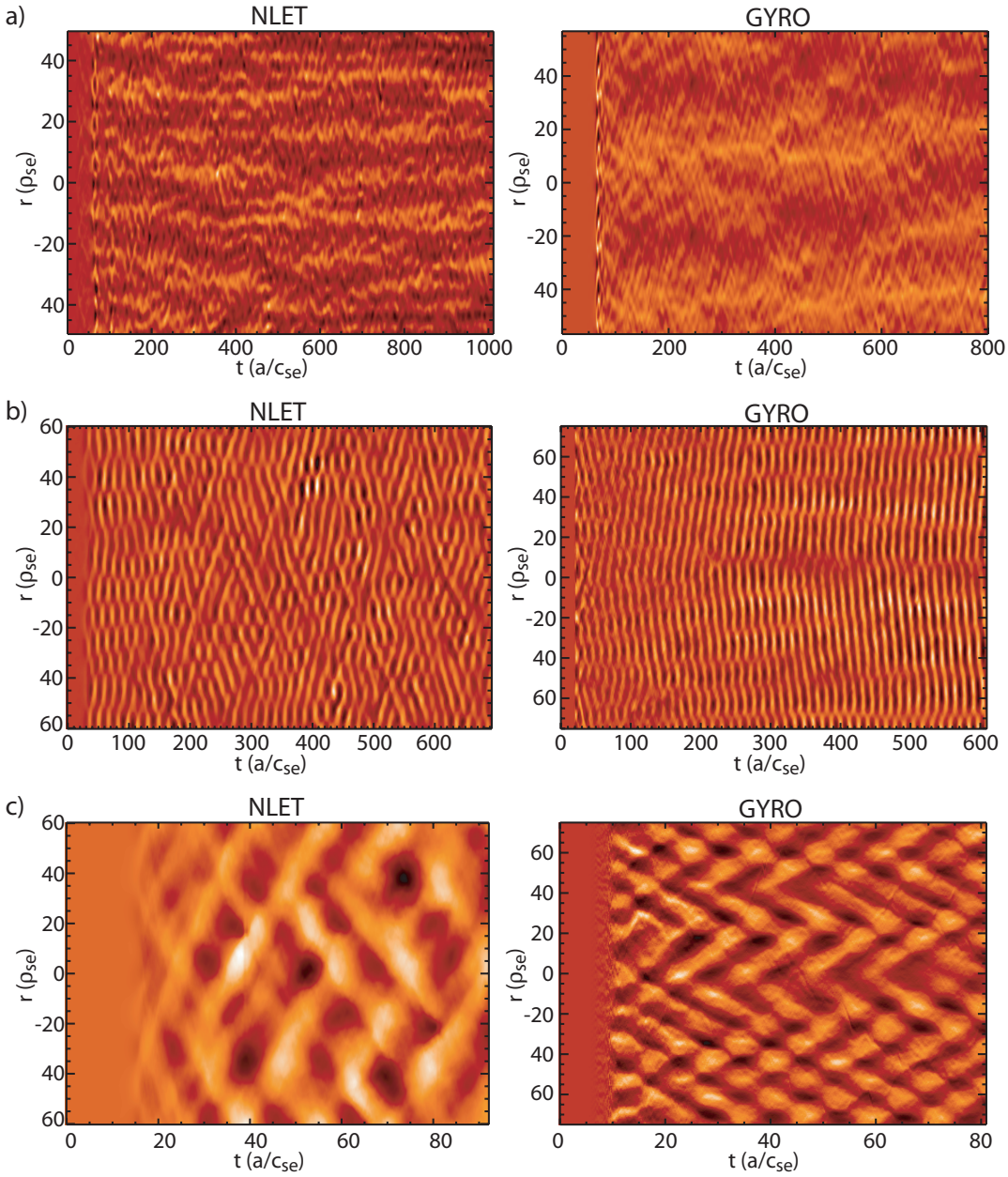

Figure 4.3: Flux-surface averaged poloidal flow velocity vs. radial position and time. a) Cyclone base case. b) GAM case 1. c) GAM case 2. Neither strong stationary zonal flows nor strong GAMs are observed for the Cyclone base case parameters. Only weak zonal flows are excited by the turbulence. The oscillations visible in a) are sub-dominant GAMs. In contrast, b) and c) display distinct GAM characteristics. The more accented GAM oscillations in the gyrokinetic simulation in c) correspond to the lower turbulence intensity shown in Fig. 4.2.

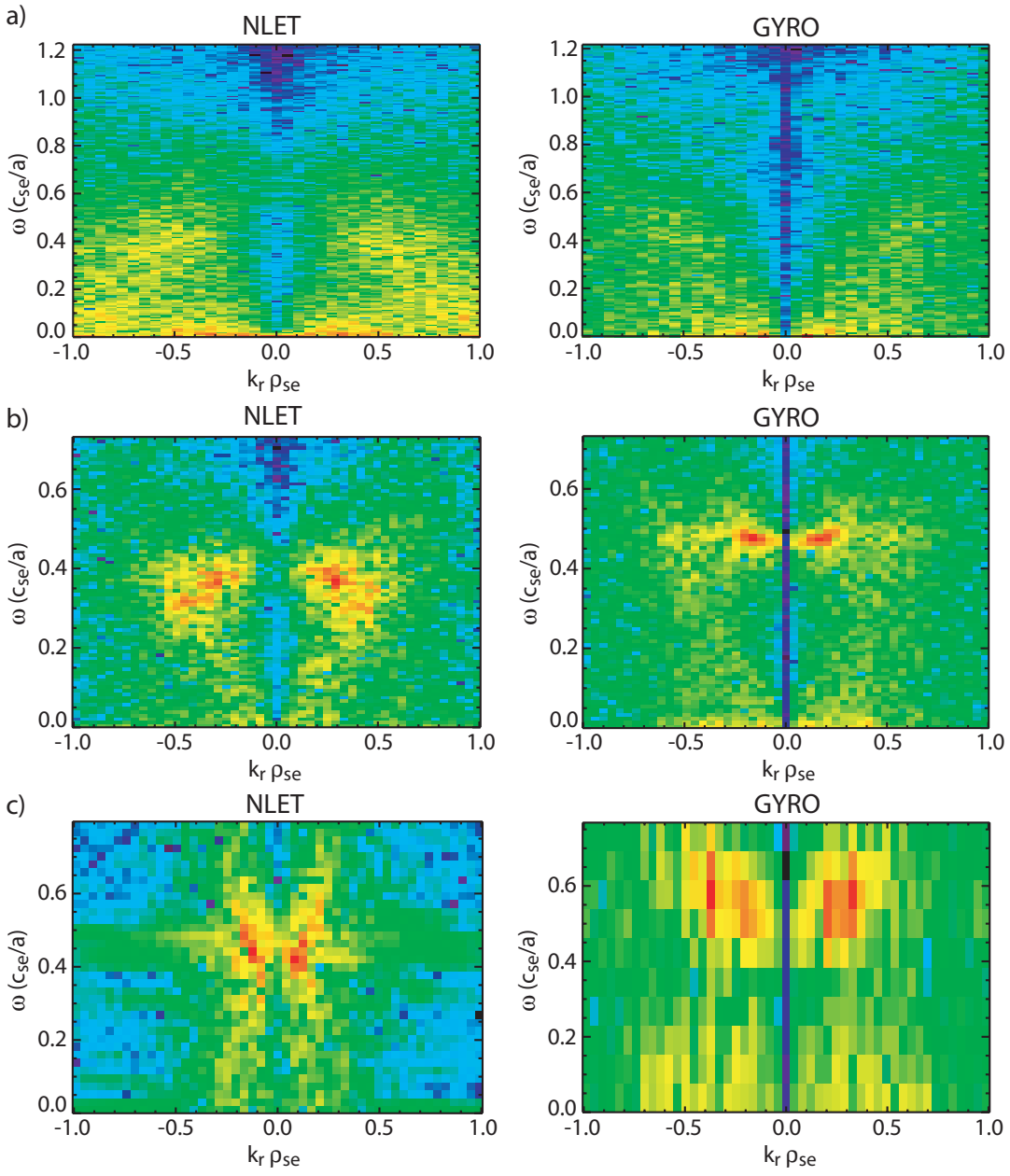

Figure 4.4: k_r-ω-spectra of the flux-surface averaged flow velocity with logarithmic colour scale. a) Cyclone base case. b) GAM case 1. c) GAM case 2. The spectra corresponding to the flow profiles shown in Fig. 4.3 confirm the observations made before. GAMs are sub-dominant in a), most of the flow activity is located at $\omega = 0$. GAMs are dominant in b) and c) with similar frequencies. The excited wave numbers differ slightly.

12.06 and 10.16. The difference between the mean of these values and the fluid result is only 3%.

For the parameters of GAM case 2, the turbulence intensity obtained with NLET is larger than the gyrokinetic one by a factor of 3. The general trend to a significantly increased heat flux for steep gradients, however, is the same in the gyrokinetic and the two-fluid calculation. Possible reasons for the observed difference in case of edge parameters are on the one hand an overestimated collisionless damping of the geodesic mode by the fluid parameters used. On the other hand the neglect of collisions in the gyrokinetic calculation could account at least for part of the discrepancy, since collisions should usually increase the heat flux and become increasingly important the closer one approaches the separatrix. Indeed, it was found that a reduction of the parallel heat conduction coefficient for the GAM results in an enhanced RMS-amplitude (root-mean-square) and a significantly reduced heat flux.

The transition from core to edge parameters is accompanied by increasing GAM activity as is evident from Figs. 4.3 and 4.4. For the core adapted parameters of the cyclone base case the dominant zonal flow is expected to be stationary whereas GAMs should only occur sub-dominant due to collisionless damping [54]. This expectation is fulfilled and the results of GYRO and NLET agree very well in that both codes yield only sub-dominant GAMs and most of the zonal flow activity is concentrated at $\omega = 0$. However, the stationary zonal flows are weak. Strong stationary flows would form a rather stable radial mode structure with a characteristic wavenumber. Due to the local limit, which makes the flow velocities small compared to c_{se}, velocities are given in units of the magnetic inhomogeneity drift instead (see Chap. 3). The RMS flow amplitude in the stationary phase for the Cyclone base case parameters is 1.54 in GYRO and NLET.

For the parameters of GAM case 1, GAMs become the dominant zonal flow for both codes. The flow amplitudes are considerably higher than in the Cyclone base case, where the value obtained with GYRO with 24.0 is more than twice the value of NLET, 9.5. The NLET GAM spectrum is broader than the spectrum computed with GYRO, and the frequencies are slightly lower. This difference may be explained by the fluid equations implemented in NLET, in which a term which is responsible for the sign change of the GAM group velocity for increasing τ (see Sec. 3.4) is neglected. However, the neglect of this term does not distort the general physics of turbulent transport and saturation through zonal flows (as can be seen from the results of earlier studies [14, 36, 61] and from the behaviour observed in this study), it only changes the GAM dispersion. Keeping in mind that the linear GAM dispersion might also be changed to some extent by the turbulence (see Chap. 5), it is in any case safe to say that the observed differences in the equilibrium between GAMs and turbulence may be caused by the neglect of the aforementioned term in NLET. Furthermore, collisions are neglected in the GYRO runs, which may also play a role for edge turbulence simulations. Similar observations are made for the parameters of GAM case 2. The GAM frequency is slightly lower in NLET simulations, the wave numbers are similar yet not equal. The flow amplitude obtained with GYRO (45.5) is again higher than that obtained with NLET (34.5). The GAM pattern in the GYRO flow profile in Fig. 4.3 c) is much sharper than its NLET equivalent, implying that GAMs in this case are

stronger compared to the turbulence intensity in GYRO than in NLET, i.e. very coherent mode structures can be formed in the GYRO simulation.
In summary, turbulence simulations performed with GYRO and NLET for the parameters given in Tab. 4.1 display qualitatively good agreement. Especially, the increasing GAM activity during the transition from core to edge parameters is well reproduced by both codes. The quantitative differences can partly be ascribed to the individual properties of two-fluid and gyrokinetic theories, which were discussed in Sec. 2.2.3. This is, the neglect of collisions in the gyrokinetic code for edge parameters and the only approximate implementation of collisionless damping in the two-fluid code. Judging the results discussed here, it seems reasonable to assume that the exclusive use of the two-fluid code NLET in the following chapters is justified, and that the nature of the interaction between the turbulence and the GAMs is not changed drastically by kinetic effects.

Chapter 5

Nonlinear GAM dispersion

The linear dispersion relation of GAMs – or to be precise their radial group velocity – has been discussed thoroughly in Chap. 3, including the effects of the magnetic geometry. The drive of the geodesic acoustic modes, which is provided by nonlinear terms (i.e. the turbulence), was of course neglected there. It is, however, very important because, analogous to the discussion in Sec. 2.3.1, it may modify the GAM frequency and thus the dispersion relation and the group velocity. Since GAMs are excited by and interact with the turbulence, it is necessary to investigate to what extent the dispersion is changed by the turbulence.

An example for the presumable influence of the turbulence on the GAM frequency is given by Conway's GAM measurements at the ASDEX Upgrade tokamak [7, 48], which display radial regions of constant GAM frequency (in spite of the temperature gradient) taking turns with regions in which the GAM frequency scales with $T^{1/2}$. Such behaviour, a geodesic acoustic mode with spatially constant frequency despite a non-negligible temperature gradient, has been discussed by Itoh in Ref. [10]. Assuming a quadratic dispersion relation of the form $\omega_{GAM}(r, k_r) = \omega_{GAM,0}(r)(1 + \alpha k_r^2)$ for small radial wave numbers k_r, the radial amplitude dependence of a mode with $\omega(r, k_r) = \text{const.}$ was found to have the form of an Airy function. Roughly speaking, the amplitude has a maximum at a radial position close to $\omega_{GAM}(r, k_r) = \omega_{GAM,0}(r)$, from which the amplitude decays exponentially in one direction and propagates with slowly decaying amplitude in the other direction. The directions of evanescent and propagating GAM depend on the sign of the group velocity, $v_g = 2\alpha k_r \omega_{GAM,0}(r)$, as has been discussed in Chap. 3.

The sign of the group velocity as well as its magnitude depend on α, which, due to the turbulence, may in turn deviate from its linear value in Chap. 3. Furthermore, the form of the dispersion can be influenced by the magnetic geometry. Using for example an X-point geometry as discussed in Secs. 3.6 and 3.7.1, the dispersion becomes effectively linear for small k_r. The radial mode structure according to Ref. [10] is influenced by all of the aforementioned points.

Therefore, the problem of the radial mode structure will be reviewed (following Ref. [62]) in Sec. 5.1 in order to elucidate the influence of the dispersion and to introduce a method to measure the coefficient α in the quadratic dispersion defined above. In Sec. 5.2, the linear

behaviour of GAMs in such slightly nonlocal systems will be discussed. Finally, in Sec. 5.3, the nonlinear GAM dispersion is studied with nonlocal, nonlinear NLET simulations, which allows the identification of the nonlinear driving term responsible for the frequency modification.

5.1 Radial mode structure

The flow profiles in Fig. 4.3 b) and c) and the corresponding spectra in Fig. 4.4 b) and c) are typical examples for GAMs in local turbulence simulations. The GAM activity is concentrated at two points of a presumed dispersion relation, which may be close to the linear one, if the influence of the turbulence on the GAM frequency is weak. Thus, the characteristic criss-cross pattern observed in the GAM flow profiles results in principle from the superposition of the two Fourier modes $(\pm k_r, \omega_{GAM})$. If the local limit is relaxed, the radial mode structure becomes more complex because, due to the temperature gradient, a Fourier mode with a specific frequency contains contributions of various radial scales k_r.
The degree of locality in NLET simulations is described by the ratio of the turbulence- to the background-gradient scale lengths $\lambda^{-1} \equiv L_\perp / L_n$, which is proportional to $\rho^\star = \rho_{se}/a$. A ratio of $\lambda \sim 5 - 50$ is typical for the situation in the edge region. Local simulations typically use $\lambda \sim 1 \cdot 10^5$. However, with a high degree of non-locality, the plasma parameters and therefore also the characteristics of the turbulence vary drastically over the computational domain. Thus, even if GAMs might be excited everywhere in the simulation domain, it is not clear whether the turbulence alters the GAM dispersion in the same way at each radial position. For simulations intended to measure the nonlinear GAM dispersion higher values of $\lambda \sim 200$ are preferred, which implies slow parameter variation. Thus, the turbulence is kept sufficiently homogeneous while the GAM frequency varies considerably by $\Delta\omega_{GAM} \sim \omega_{GAM,0}/2$, where the subscript "0" marks the reference frequency at the centre of the computational domain.
Looking at the results of GAM measurements in Refs. [7, 48], one may be directed to the conjecture that the GAMs organise themselves in a global mode with a specific radial mode structure determined by the following condition for the mode frequency

$$\omega_{GAM}\,(r, k_r) = \text{const.} \tag{5.1}$$

According to the arguments in Chap. 3 and the numerical results of Chap. 4, GAMs are likely to be excited at small radial wave numbers. Therefore and due to the assumption of slow parameter variation, it is reasonable to approximate the dispersion relation of the GAM by

$$\omega_{GAM}\,(r, k_r) = \omega_{GAM,0}(r)(1 + \alpha k_r^\beta), \tag{5.2}$$

where $\omega_{GAM,0}(r)$ is the local GAM frequency at $k_r = 0$, which is basically proportional to the square root of the sum of the ion and electron background temperatures. The constant factor α accounts for the influence of turbulence, which may enhance or weaken the dispersion. The form of the dispersion can be controlled by the exponent β. For circular magnetic geometry, the linear dispersion has been shown to be quadratic in k_r in the vicinity of $k_r = 0$ in Chap. 3, whence the natural choice for β is $\beta = 2$. However,

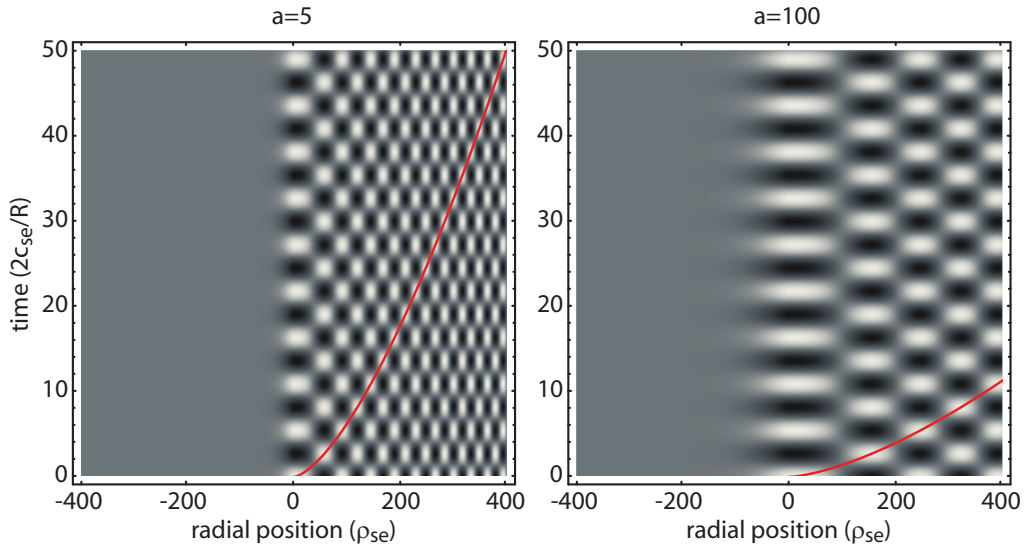

Figure 5.1: Idealised picture of the radial mode structure corresponding to the superposition of plane waves with fixed frequency, wave numbers according to Eq. (5.3) and an r-dependent phase shift assuring that the phase is constant on the curve (5.5) with $\beta = 2$. In the plot on the left, $\alpha = 5$. Group velocities comparable to those calculated in Chap. 3 correspond to $\alpha = 0.25$. The plot on the right with $\alpha = 100$ illustrates the effect of a strong dispersion. The incoming waves are reflected at $r = 0$ and form a standing wave pattern with the reflected waves. The red lines indicate a curve of constant phase.

as shown for X-point geometry in Sec. 3.7.1, the dispersion can be nearly linear for small wave numbers, which would justify the choice $\beta = 1$. As a generalisation of this approach, the GAM dispersion could be approximated by a Taylor series.
In order to satisfy the condition (5.1) with the GAM frequency given by Eq. (5.2), the wave number must vary with r:

$$k_r(r) = \left[\frac{1}{\alpha}\left(\frac{\omega_{GAM}}{\omega_{GAM,0}(r)} - 1\right)\right]^{1/\beta} \approx \left[\frac{1}{\alpha}\frac{\partial_r \omega_{GAM,0}(r_0)}{\omega_{GAM}}\,(r_0 - r)\right]^{1/\beta}, \tag{5.3}$$

where $\omega_{GAM} = \omega_{GAM,0}(r_0)$ is fixed. If the dispersion is quadratic, i.e. $\beta = 2$, Eq. (5.3) has no real solution for $\omega_{GAM,0}(r) > \omega_{GAM}$ if $\alpha > 0$ or for $\omega_{GAM,0}(r) < \omega_{GAM}$ if $\alpha < 0$. Since $\omega_{GAM,0}$ decreases towards the edge, this means that the mode is restricted to $r > r_0$ or $r < r_0$, respectively, which is in line with the result in Ref. [10]. Thus, the mode is reflected at $r = r_0$ and since the frequencies of incoming and reflected wave are equal, a standing wave pattern can form. If $\beta = 1$, however, Eq. (5.3) has a unique solution for all r. Therefore, at a given radius r at given $|k_r|$ incoming and outgoing waves have different frequencies, whence no standing wave pattern can develop.
A point moving with the phase velocity on a curve of constant phase $r(t)$ (or $t(r)$) of a mode obeying Eq. (5.1) has to fulfill the equation of motion

$$\dot{r} k_r(r) = \omega_{GAM}. \tag{5.4}$$

Substituting the approximated right-hand-side of Eq. (5.3), this can be integrated over time in order to obtain a wave front $t(r)$:

$$t(r) = \frac{1}{1+\frac{1}{\beta}} \left(-\frac{\partial_r \omega_{GAM,0}(r_0)}{\alpha \omega_{GAM}^{1+\beta}} \right)^{\frac{1}{\beta}} (r-r_0)^{1+\frac{1}{\beta}} + t_0 \tag{5.5}$$

An idealised picture of the radial mode structure corresponding to this wave front can be obtained by the superposition of plane waves with fixed frequency, wave numbers according to Eq. (5.3) and an r-dependent phase shift assuring that the phase is constant on the curve (5.5). Figure 5.1 shows examples for $\beta = 2$ for two different values of α. The reflection layer at $r = r_0$ is clearly visible, and incoming and reflected wave form a regular standing wave pattern with a radial scale that varies with r. For a weak dispersion (small α), k_r increases rapidly with increasing distance from r_0. Since, due to the resonances discussed in Chap. 3, GAMs with larger wave numbers are expected to be damped in turbulence simulations, the resulting modes are expected to have a rather small radial extent. On the contrary, if the dispersion is strong, larger radial structures are expected to be observed. By fitting the wave front (5.5), i.e. a function $t(r) = t_0 + a(r-r_0)^{1+1/\beta}$ to the frequency filtered flow profile obtained from a nonlocal nonlinear NLET run, the underlying dispersion relation can be approximated.

5.2 GAMs in linear nonlocal simulations

As a preparation for the nonlinear case, it is useful to have a look at the behaviour of GAMs in linear nonlocal simulations. The interpretation of the results of such studies thereby benefits from the fact that the linear dispersion for circular geometry is known.
The situation of a GAM that propagates radially, parallel to a temperature gradient, is completely equivalent to the propagation of a wave, e.g. an electromagnetic wave, in a dispersive medium. In a stationary situation, the frequency of the wave stays constant even if the properties of the medium (the refractive index) change. The phase velocity, however, depends on the medium. Therefore, a change of the medium goes along with a change of the wave number of the wave in order to keep the frequency constant. The effect of the temperature gradient on the GAM dispersion is basically a (radius dependent) up- or downshift of the frequency referring to some reference radius. Consider now a GAM wave packet at $r = r_0$ with wave numbers centered around an initial $k_{r,0}$. The wave packet propagates radially with its group velocity to $r = r_0 + \delta r$ into a region with temperature $T = T(r_0) + \delta T$ and a dispersion relation which is, in principle, the dispersion relation at r_0 shifted by $\delta\omega(\delta T)$. Depending on $\delta\omega$, the wave number of the initial wave packet either increases or decreases. However, it is straightforward to show that in the case $\partial_r T < 0$ – which is the case in tokamak plasmas – the wave number will always increase (including sign changes), no matter what the dispersion looks like.
Consequently, a GAM wave packet obeying the dispersion relation (5.2) with $\beta = 2$ and $\alpha < 0$ (as in the case of cold ions in circular geometry, Chap. 3) will always propagate towards higher temperatures, whereas it will propagate towards lower temperatures for $\alpha > 0$. In either case, the wave packet is accelerated by the temperature gradient. On the

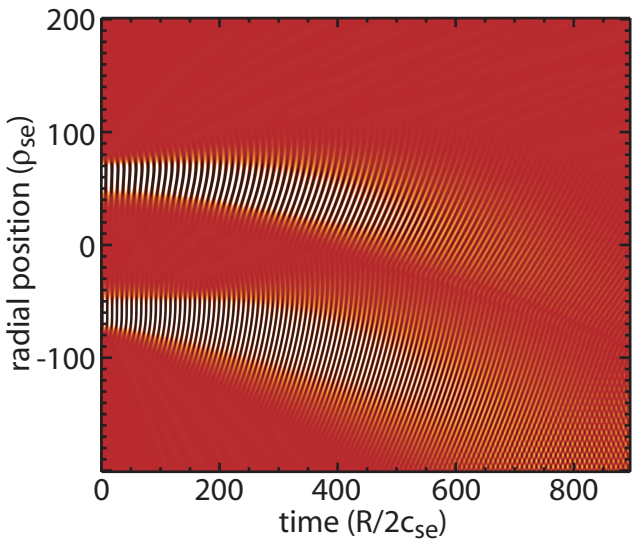

Figure 5.2: Flux-surface averaged poloidal flow velocity vs. radial position and time. The background temperature varies slowly with radius. At $t = 0$ two GAM wave packets are initialised at different radial positions, as can be seen from the differing frequencies. Since the frequency of a wave remains constant, the radial wave number has to change on radial propagation. Therefore, the wave packets are accelerated radially inward by the temperature gradient, since group and phase velocity in this case have opposite sign. If group and phase velocities had equal sign, the acceleration would be radially outward.

contrary, the propagation velocity is not influenced by the temperature gradient in case of a linear dispersion, $\beta = 1$, which applies for small k_r in a single-null geometry.

The above discussion is illustrated by Figs. 5.2 and 5.3, which show the result of a cold ion nonlocal linear run. At time $t = 0$ two GAM wave packets are initialised at different radial positions. The electron background temperature profile (normalized to $T_{e,0}/\lambda$) is given by $\lambda - 0.34r$ with $\lambda = 100$, where the radial position r is measured in ρ_{se} and $r = 0$ in the middle of the radial domain. The box size in radial and toroidal direction is $400\rho_{se} \times 400\rho_{se}$. Due to the assumption of cold ions, the GAM dispersion relation has the form of Eq. (5.2) with $\beta = 2$ and $\alpha < 0$. From the poloidal flow velocity plotted versus radius and time in Fig. 5.2, it is easily seen, that the frequencies of the two wave packets differ. Components of the wave packets with negative wave numbers initially propagate to the low temperature region. As discussed above, the temperature gradient accelerates the GAM radially inward and shifts the excited wave numbers to larger values. Therefore, the propagation radially outward is slowed down, stopped, and finally reversed. The $k_r - \omega$ spectrum is shown in Fig. 5.3 for two different time intervals. The left plot in Fig. 5.3 shows the Fourier transform of the flow profile in Fig. 5.2 in the time interval from $t = 0$ to $t = 200$, which is close to the initial state. The full time interval is covered by the right plot in Fig. 5.3. Corresponding to the acceleration up the temperature gradient, the GAM intensity in the spectrum moves at constant frequency to larger wave numbers. For

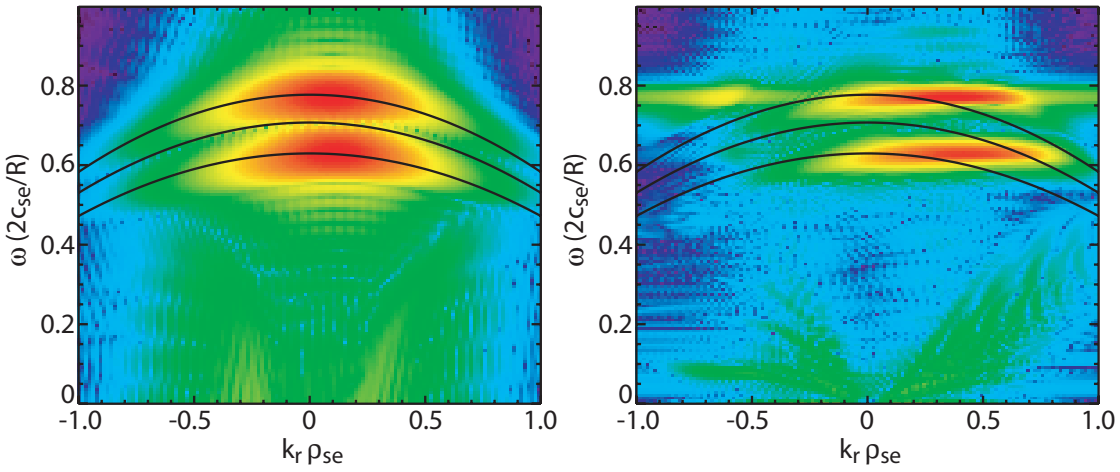

Figure 5.3: Flow spectra (with logarithmic colour scale) at two different times corresponding to the flow profile in Fig. 5.2. The approximated dispersion relations for the middle of the radial domain as well as for the initial radial positions of the GAM wave packets are indicated by the solid lines. Left: Fourier transform of Fig. 5.2 in the time interval $(0, 180)$. Right: Time interval $(0, 900)$. The excited wave numbers increase with time, corresponding to an acceleration radially inwards.

the initial phase on the left-hand side of Fig. 5.3, the excited GAMs agree with the linear dispersions, which are indicated by solid curves for $r = 0$ and $r = \pm 60$.

In another nonlocal linear NLET run, whose results are shown in Figs. 5.4 and 5.5, the temperature variation is stronger than in the case discussed before. The locality parameter λ is now 225 and $T_e(r) = \lambda - 1.13r$. Moreover, GAMs are initialised at $t = 0$ over the whole radial width of the computational domain. The resulting poloidal flow velocity is plotted against radius and time in Fig. 5.4 a). The flow velocity is seen to oscillate at each radial position essentially at the local GAM frequency, whence the observed radial wave numbers increase with time. The fact that the GAM oscillates at its local frequency is also evident from the temporal Fourier transform corresponding to the flow profile, shown in Fig. 5.4 b). The intensity follows the local GAM frequency, which is indicated by the dashed line. Only small deviations from the local frequency are observed, which is in line with the weak linear dispersion ($\alpha \approx -0.25$, Secs. 3.3 and 5.1). The radial mode structure of a GAM with a distinct frequency can be compared to the generic mode structures shown in Fig. 5.1, by extracting one frequency component from the flow profile in Fig. 5.4 a). The flow profile of the Fourier mode with the local frequency at $r = 0$ is shown in Fig. 5.5. Due to the initialisation at $t = 0$, only very small wave numbers are excited, which then increase with time. Therefore, positive k_r dominate in Fig. 5.5, and no standing wave pattern develops. Nevertheless, the observed wavenumber increases rapidly with decreasing r, which again confirms the weakness of the linear dispersion. As conjectured in Sec. 5.1, the mode is evanescent for $r > r_0$, since $\alpha < 0$.

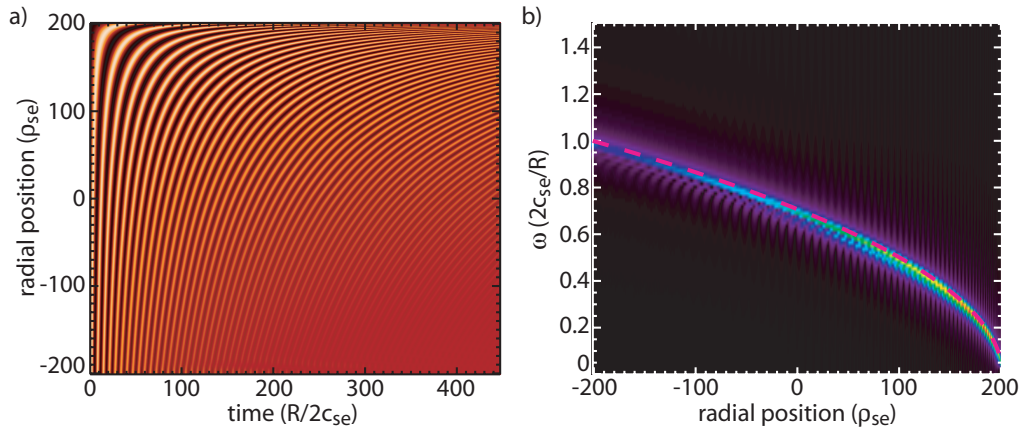

Figure 5.4: Result of a linear nonlocal NLET run, in which a GAM is initialised at $t = 0$ over the full radial domain. The electron temperature decreases linearly from the inner to the outer radial boundary. The ratio of ion to electron temperature is $\tau = 0$. a) Flux-surface averaged poloidal flow velocity vs. radial position and time. The flow velocity oscillates at each radial position with the local GAM frequency. Therefore, the excited radial wave numbers increase with time. b) Temporal Fourier transform of the flow profile on the left with linear colour scale. The dependence of the local GAM frequency on the square root of the background temperature (dashed line) is clearly visible.

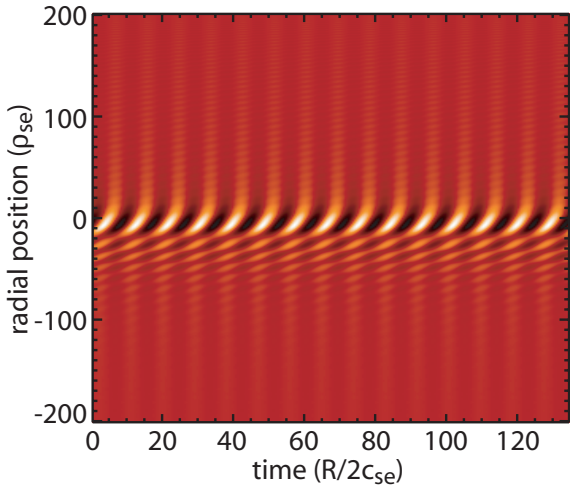

Figure 5.5: Fourier mode of the flow profile of Fig. 5.4 a). The frequency shown here is the local frequency in the middle of the radial domain, $\omega \approx 1/\sqrt{2}$. As anticipated from Fig. 5.4 a), the mode width is very small, corresponding to a weak dispersion. Apart from the fact that almost only modes with positive phase velocity are present, the observed mode structure is similar to the one in Fig. 5.1 with $\alpha = 0.25$. The faint oscillations far from $r = 0$ are remnants of the Fourier transform.

5.3 Nonlinear GAM dispersion in nonlocal simulations

Having established a basis for the investigation of the nonlocal properties of GAMs with the detailed discussion in the previous sections, the influence of the nonlinear terms in the fluid equations is considered in the following.

The results for the poloidal flow velocity of a nonlinear, nonlocal NLET code run are shown in Fig. 5.6. The computational domain extends over $800\rho_{se}$ in the radial as well as in the toroidal direction. The ratio of the density to the ion temperature gradient scale length is $\eta_i \equiv L_n/L_{T_i} = 2.4$ and $\lambda = 200$. The background density and temperature profiles are linear, and the parallel ion dynamics are neglected ($\epsilon_v = 0$). Thus, the local GAM frequency $\omega_{GAM,0}(r)$ varies by roughly $\pm 0.3\omega_{GAM,0}(r = 0)$, where $r = 0$ marks the middle of the radial domain. Furthermore, $\epsilon_n = 0.05$ and $\alpha_d = 0.5$ (for a definition, see Ref. [14]).

The corresponding flow profile is shown in Fig. 5.6 a). The frequencies at the inner and the outer boundary are seen to differ. Apart from that, the flow profile appears rather similar to, for example, the flow profiles shown in Fig. 4.3 b) and c). However, the corresponding temporal Fourier transform, shown in Fig. 5.6 b), reveals the influence of the turbulence. The local GAM frequency is indicated in the spectrum by the dashed red line. In contrast to the linear run discussed in the previous section, whose spectrum is shown in Fig. 5.4 b), the GAM activity is not concentrated in a narrow region around $\omega_{GAM,0}(r)$. Rather, the GAMs with the local frequency $\omega_{GAM,0}(r_0)$ radiate outwards considerably, starting from the radius r_0. Frequencies which are about 30% higher than the local frequency can be observed. Judged on the basis of Secs. 5.1 and 5.2, this points towards a much stronger dispersion than in the linear case.

A quantitative conclusion on the nonlinear dispersion can be drawn from the Fourier component of 5.6 a) with $\omega = 1.14$, which is slightly lower than the local GAM frequency at $r = 0$, $\omega_{GAM,0}(r = 0) = (8/6)^{1/2}$. This mode displays a very clear radial mode structure, as can be seen in Fig. 5.6 c). However, the preference of this frequency is only a statistical effect due to the finite simulation time. For very long run times, all modes are expected to be equivalent. The observed radial mode structure in the nonlinear case shows a much larger radial scale length of roughly $100\rho_{se}$ compared to the linear case shown in Fig. 5.5 with a radial scale length of about $10\rho_{se}$. Indeed, a least-squares fit to a curve of constant phase according to Eq. (5.5) with $\beta = 2$ – indicated by the solid blue line in Fig. 5.6 c) – yields $\alpha \approx 109$, which is about a hundred times the value of the linear dispersion relation.

In Fig. 5.7 a), this result is compared to the GAM spectrum obtained from an equivalent local NLET run with $\lambda = 10^4$. Analogous to the examples shown in Fig. 4.3, the GAM is excited at a preferred $|k_r|$ with the corresponding frequency. The quadratic dispersion relations according to Eq. (5.2) with $\alpha = 1$, which is roughly the linear value, and $\alpha = 109$, the result for the fitting curve, are plotted over the spectrum. The dispersion for $\alpha = 1$ is clearly much too weak to explain the excited frequencies. On the contrary, the dispersion obtained from the nonlocal run fits very well to the GAM spectrum of the local simulation.

The cause for the nonlinear frequency shift is investigated below with the two-fluid equations as implemented in the NLET code [14]. Since $\epsilon_v = 0$, all terms involving the parallel velocity are neglected as well as all terms of order $k^2\rho_i^2$. The electron response is assumed

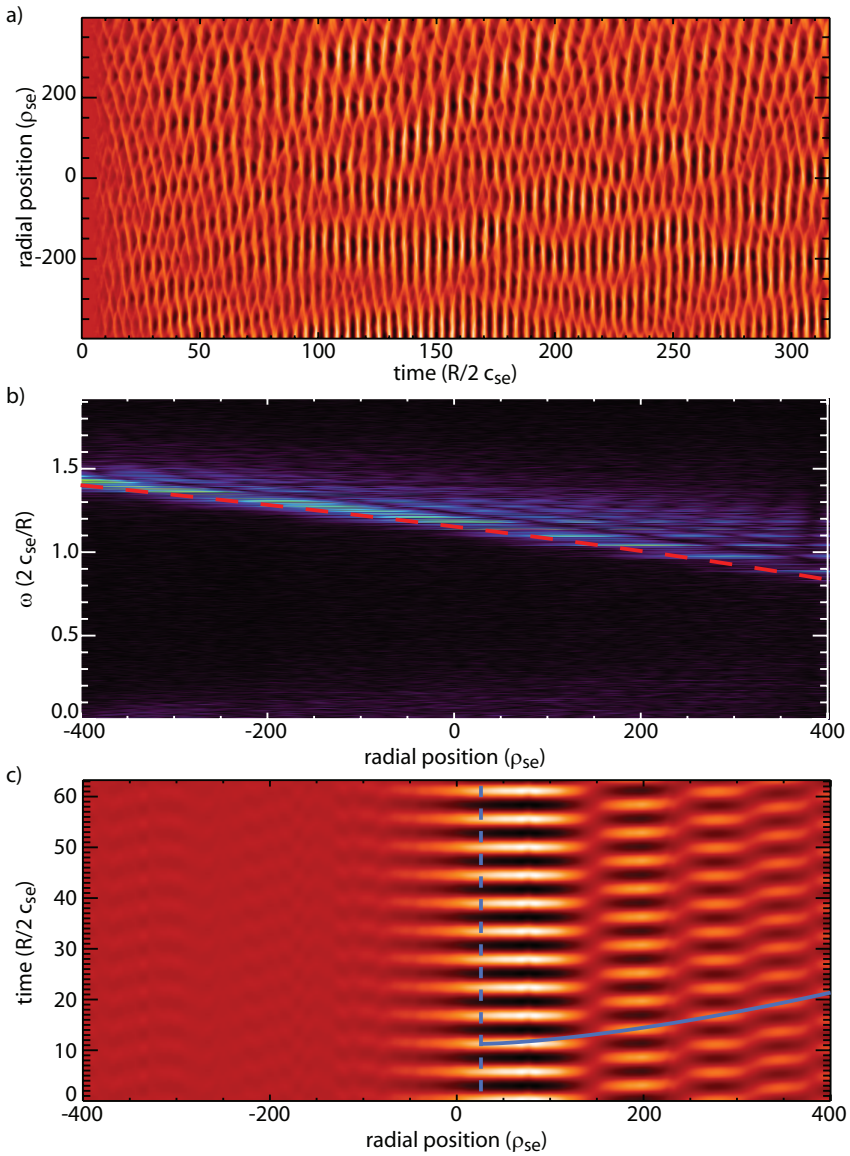

Figure 5.6: Results of a nonlinear, nonlocal NLET code run with slow parameter variation, $\lambda = 200$. a) Flow profile. b) Temporal Fourier transform (linear colour scale) of a) with the local GAM frequency indicated by the dashed line. c) Single Fourier mode of the flow profile with $\omega = 1.14$ with a fit to a curve of constant phase according to Eq. (5.5). The radial position where $\omega_{GAM,0}(r_0) = 1.14$ is indicated by the dashed line. The radially varying GAM frequency is already visible in the flow profile. The temporal Fourier transform of the flow reveals that, in contrast to Fig. 5.4 b), the GAMs are also excited by the turbulence at frequencies considerably higher ($\sim 30\%$) than the local frequency. The filtered flow profile displays a radial mode structure similar to the strong dispersion case in Fig. 5.1.

adiabatic. Therefore, the resulting fluid equations for the vorticity, the ion density and the ion temperature are given by

$$\begin{aligned}
&\nabla_\perp \cdot \frac{n}{\lambda}\frac{\mathrm{d}}{\mathrm{d}t}\left(\nabla_\perp\phi + \frac{\alpha_d\tau}{n}\nabla_\perp p_i\right) + \frac{1}{\lambda}\hat{\mathbf{C}}p_g - \partial_\parallel j_\parallel = 0,\\
&\frac{\mathrm{d}}{\mathrm{d}t}n - \epsilon_n\frac{n}{\lambda}\left(\hat{\mathbf{C}}\phi + \frac{\alpha_d\tau}{n}\hat{\mathbf{C}}p_i\right) = 0,\\
&\frac{\mathrm{d}}{\mathrm{d}t}T_i - \frac{2}{3}\epsilon_n\frac{T_i}{\lambda}\left(\hat{\mathbf{C}}\phi + \frac{\alpha_d\tau}{n}\hat{\mathbf{C}}p_i + \frac{5}{2}\alpha_d\tau\hat{\mathbf{C}}T_i\right) = 0,
\end{aligned} \tag{5.6}$$

where n is the density, T_i the ion temperature, $p_{i,e} = nT_{i,e}$ and $p_g = (p_e + \tau p_i)/(1+\tau)$. The $\mathbf{E}\times\mathbf{B}$ velocity is given by $\mathbf{v}_E \equiv \hat{\mathbf{z}}\times\nabla_\perp\phi$. The total time derivative is defined by $\mathrm{d}_t \equiv \partial_t + \mathbf{v}_\mathbf{E}\cdot\nabla$. The fluid system (5.6) contains three nonlinear terms which may either transfer energy to the GAM oscillations or modify the GAM frequency. Separating linear and nonlinear terms in the flow and the density equation yields

$$\nabla_\perp \cdot \frac{n}{\lambda}\partial_t\left(\nabla_\perp\phi + \frac{\alpha_d\tau}{n}\nabla_\perp p_i\right) + \frac{1}{\lambda}\hat{\mathbf{C}}p_g - \partial_\parallel j_\parallel + \underbrace{\nabla_\perp\cdot\frac{n}{\lambda}\mathbf{v}_E\cdot\nabla\left(\nabla_\perp\phi + \frac{\alpha_d\tau}{n}\nabla_\perp p_i\right)}_{\text{Reynolds stress}} = 0,$$

$$\partial_t n - \epsilon_n\frac{n}{\lambda}\hat{\mathbf{C}}\phi + \underbrace{\mathbf{v}_E\cdot\nabla n}_{\text{asymmetric transport}} - \underbrace{\frac{\epsilon_n\alpha_d\tau}{\lambda}\hat{\mathbf{C}}p_i}_{\text{diamagnetic drive}} = 0. \tag{5.7}$$

The flow velocity component of the GAM can exchange energy with the turbulence via the Reynolds stress. The GAM induced density fluctuation is coupled to the turbulence, on the one hand, through the up-down asymmetric component of the transport term $\mathbf{v}\cdot\nabla n$. On the other hand, the flux-surface averaged transport can modify the background gradients. Through the curvature term $\epsilon_n(n/\lambda)\hat{\mathbf{C}}p_i$, the GAM is therefore also indirectly coupled to the flux-surface averaged transport. For further reference on the nonlinear mechanisms driving the GAM see Refs. [11, 36, 63].

Setting $k_r = 0$, it is straightforward to transform the linearised Eqs. (5.6) into an eigenvalue problem for the total pressure and the flow velocity of the GAM analogous to Eq. (2.80). The corresponding eigenvalues are as in Sec. 2.4 given by the local GAM frequency $\pm i\omega_{GAM,0}(r)$. Using the notation of Sec. 2.4, the present state of the GAM oscillation is characterised by its pressure $\tilde{p}$ and its poloidal flow velocity $\tilde{v}_E$. At each r, the Fourier components of $\tilde{p}$ and $\tilde{v}_E$ with frequency $\omega_{GAM,0}(r)$ can therefore be regarded as the components of a vector $\mathbf{\Psi}$ of constant length in the $\tilde{n} - \tilde{v}_E$ plane, whose base point is at the origin and whose tip rotates with $\omega = \omega_{GAM,0}(r)$ around the origin. The length of the state vector, $\left|\mathbf{\Psi}\right|$ is defined as the energy contained in the GAM. In this picture, the linear (in the perturbations $\tilde{p}$, $\tilde{v}_E$) parts on the right-hand-side of the equations of motion $\partial_t\tilde{p} = \ldots$ and $\partial_t\tilde{v}_E = \ldots$ (see Eq. (5.7)) for density and flow correspond to differential vectors $\delta\mathbf{\Psi}_{lin}$, which are perpendicular to $\mathbf{\Psi}$ and thus rotate the tip of $\mathbf{\Psi}$ around the origin with the linear GAM frequency, keeping the energy constant. The nonlinear terms $\delta\mathbf{\Psi}_{nonlin}$, however, do not need to be perpendicular to the state vector $\mathbf{\Psi}$, since they can exchange energy between GAMs and turbulence. Thus, they have to be decomposed into their components

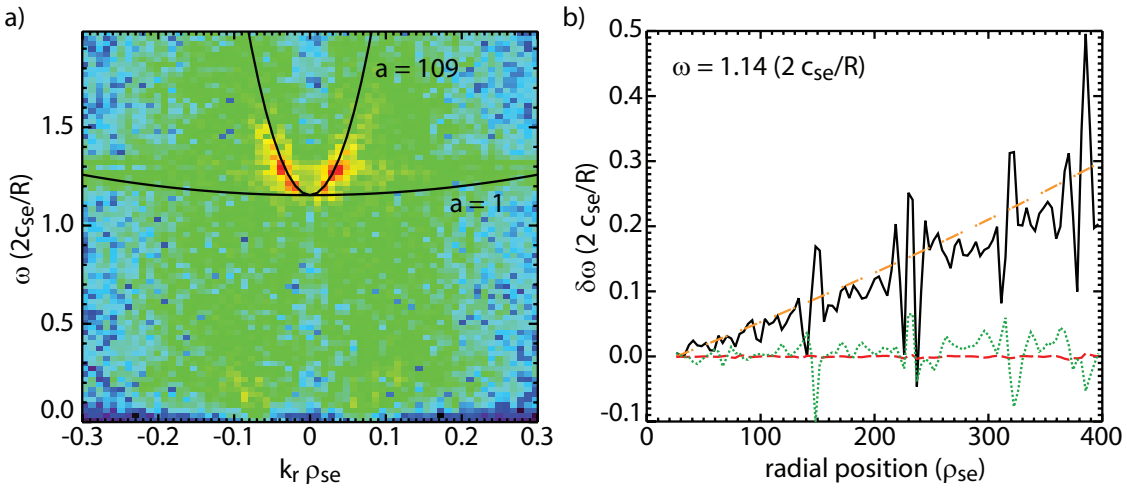

Figure 5.7: a) Flow spectrum of a local simulation ($\lambda \gg 1$) otherwise equivalent to the one shown in Fig. 5.6 (using the parameters at $r = 0$). The result of the fitting curve of Fig. 5.6 c) corresponds to $\alpha = 109$. The resulting dispersion $\omega_{GAM}(r, k_r) = \omega_{GAM,0}(r)(1+\alpha k_r^2)$ agrees well with the result of the local simulation. The dispersion relation for $\alpha = 1$ is also indicated as reference. b) Nonlinear frequency shift. The frequency shift required to explain the radial mode structure of the mode with $\omega = 1.14$ is indicated by the dashed-dotted orange line. The solid black line is the frequency shift resulting from the up-down asymmetric component of the turbulent transport. The contribution of the frequency shifts induced by the diamagnetic (dashed, orange) and the Reynolds stress (dotted, green) to the total nonlinear frequency shift is marginal.

parallel to $\mathbf{\Psi}$, which account for the energy exchange, and their components perpendicular to $\mathbf{\Psi}$. Clearly, the latter account for the nonlinear frequency shift.
These frequency shifts due to the various nonlinear terms have been computed for the nonlocal NLET run discussed above. The results for the mode with $\omega = 1.14$, shown in Fig. 5.6 c), are plotted against the radial position r in Fig. 5.7 b). The frequency shift required to explain the radial mode structure in Fig. 5.6 c) is indicated by the dashed-dotted, orange line. The frequency shift induced by the up-down asymmetric component of the nonlinear transport, represented by the solid black line, agrees well with the expected value, apart from statistical noise. The remaining nonlinear terms, the diamagnetic drive and the Reynolds stress, do not contribute to the nonlinear frequency shift in the case discussed here. However, the influence of the nonlinear terms on the GAM frequency may depend sensitively on the properties of the turbulence. The flow spectrum in Fig. 4.4 b) for example rather suggests a negative value of α, corresponding to a GAM radiating radially inward. Indeed, if λ is reduced to 100, an NLET run with otherwise equal parameters confirms this conjecture, yielding $\alpha \approx -1$. A value of $\alpha \approx +2$ is obtained in an analogous simulation for the run shown in Fig. 4.4 c). Since the only difference between those two runs are the values of $\epsilon_n \equiv 2L_n/R$ and L_n/L_T (0.2 and 0.08, and 3 and 5, respectively), one may speculate, whether the steepness of the gradients, given by ϵ_n, is one relevant

parameter controlling the nonlinear GAM dispersion. The NLET run analysed in this section (see Fig. 5.6) has an even smaller value of $\epsilon_n = 0.05$ and displays a stronger dispersion with $\alpha = 109$. Regarding the dependence of α on the plasma parameters, one is led to the conjecture that GAMs can also exist as modes which are "trapped" between reflection and absorption layers on different flux-surfaces. Within the framework of the preceding discussion, an absorption layer would occur where $\alpha = 0$. If the group velocity is zero, only GAMs at the local GAM frequency $\omega_{GAM,0}(r)$ can exist. If a GAM with different frequency approaches the absorption layer, $k_r \to \infty$, which results in strong damping by the resonance effects discussed in Chap. 3. GAMs at the local GAM frequency can be expected to be strongly damped due to phase mixing effects. This situation somewhat reminds of a GAM amplitude profile measured in TEXTOR [64], which displays a narrow amplitude dip in a region where the GAM frequency scales with the square-root of the temperature. Regarding the above result that this scaling can be due to a weak dispersion, it may well be that the dip is due to a sign change of α, i.e. due to an absorption layer.

Chapter 6

GAMs in NSTX and ASDEX Upgrade

As outlined in the introduction, GAMs are an ubiquitous phenomenon in the edge of tokamak plasmas. Naturally, the existence of experimental data demands for comparisons between theory and experiment. In this context, the following numerical studies contribute to the understanding of certain aspects of GAM measurements performed in the tokamaks ASDEX Upgrade and NSTX.

6.1 Quiet periods in NSTX – GAMs?

The GAM analysis for experimental NSTX equilibria is motivated by findings of Zweben et al. [13]. Edge turbulence structures can be measured in NSTX by the GPI diagnostic (see Ref. [13] and references therein), whose main component is a fast camera system able to record images at a frame rate of up to 285000 frames per second for a period of up to 50 ms. The cameras capture the light emitted by neutral gas, which is puffed into the plasma edge. The intensity of the emitted light depends on the plasma density and temperature, whence the captured light also reflects the turbulence intensity.
In many neutral beam injection heated discharges, the GPI data indicates that the L-H-transition is preceded by roughly periodic ($\nu \sim 3\,\mathrm{kHz}$) quiet periods, that is time intervals with suppressed turbulence activity. During these quiet periods, the intensity captured by the GPI diagnostic – though still in L-mode – is of the order of the intensity level measured after the L-H-transition. Since the quiet periods are observed to be correlated with an inversion of the poloidal flow velocity, the experimental results resemble the modulation of the turbulence intensity by geodesic acoustic modes described for example in [36]. Thus, the question arises whether the quiet periods are indeed caused by a modulation of the turbulence by GAMs.
The first step of this investigation is the calculation of the linear GAM frequency for the experimental equilibrium data, which is obtained via an EFIT equilibrium reconstruction [65]. From this data – particularly from the poloidal flux data $\Psi_P(R, Z)$ and the safety factor profile $q(\Psi_P)$ – the local magnetic geometry is computed applying the Mercier-Luc

formalism described in Sec. 2.1. Afterwards, the linear GAM frequency (in dimensionless units) at zero radial wave number, $k_r = 0$, is evaluated for the experimental equilibrium as explained in Sec. 2.4. Finally, by combining the GAM frequency data with the experimental temperature profile, a radial GAM frequency profile in SI units is obtained, which can easily be compared to experimental data. Let the dimensionless GAM frequency be denoted by G here. The sound speed is $c_s = [\gamma(T_i + T_e)/m_i]^{1/2}$, and γ is the adiabatic exponent of the system, which ranges between 1 for isothermal and 5/3 for adiabatic systems. Thus, the GAM frequency in SI units is given by

$$\nu_{GAM} = \frac{c_s}{2\pi} G. \tag{6.1}$$

In the following, when a frequency is given in SI units, it is assumed that γ is 4/3, that the ion mass m_i is the mass of deuterium, and that $T_i \approx T_e$. For comparison with results obtained with NLET, whose frequencies are measured in units of $2c_{se}/R$, the geometry factor G has to be multiplied with $(R/2) \cdot (\gamma_e + 5\tau/3)$, where $\tau = T_e/T_i$ and $\gamma_e = 1$ if electron temperature fluctuations are neglected, and $\gamma_e = 5/3$ when electron temperature fluctuations are included.

The NSTX discharges analysed this way are shot 135042[1] at $t = 232\,\text{ms}$, shot 139436 at $t = 243\,\text{ms}$, shot 139442 at $t = 289\,\text{ms}$ and shot 139448 at $t = 1630\,\text{ms}$. The corresponding separatrix shapes are shown in Fig. 6.1 e). The results for the GAM frequencies are plotted against the major radius R and the safety factor q in the upper parts of Fig. 6.1 a)-d) in the radial domain from $\Psi_P = 0.65 \ldots 0.98\,\Psi_{sep}$, which is equivalent to $\rho_{pol} = 0.81 \ldots 0.99$ with $\rho_{pol} \equiv ((\Psi_P - \Psi_{sep})/\Psi_{sep})^{1/2}$. Here, Ψ_{sep} is the poloidal flux at the separatrix. Since, as explained in Sec. 2.4, in realistic geometries there may be more than one mode that displays the characteristics of a GAM, each of the plots 6.1 a)-d) shows the frequencies of the five flow eigenmodes with the highest ratios of perpendicular to parallel kinetic energy. The corresponding energy ratios are plotted in the lower parts of Fig. 6.1 a)-d), and the mode with the highest ratio is indicated by the solid red line.

Despite the differences of the magnetic geometries of the considered discharges, the GAM frequencies close to the separatrix are comparable in all cases, ranging between 3 and 17 kHz. It is interesting to note here, that the variation of the shown frequencies is mainly due to the temperature profile. In dimensionless units, i.e. in terms of the geometry factor G, the frequency of the strongest GAM candidate hardly varies with R. Each discharge exhibits three eigenmodes with comparable energy ratios of $E_\perp/E_\parallel \sim 1$ at $\Psi_P = 0.98\Psi_{sep}$, which are therefore classified as GAMs. Since the parallel kinetic energy dominates in case of the remaining eigenmodes, those modes can at this stage be classified as sound waves.

In case of shot 135042, the eigenmode with the lowest frequency – which is actually only the fifth GAM candidate with $E_\perp/E_\parallel = 0.02$ – is interesting due to the poloidal amplitude structure of the corresponding parallel flow velocity, which corresponds to what is the "$m = 1$ up-down antisymmetric" soundwave in circular geometry. The $(n = 0, m = 1)$-sound

[1] For shot 135042, no temperature profile was at hand. The T_e profile was therefore estimated (with T_e in eV and R in m) as $T_e(R) \approx 250 - (250/0.14) \cdot (R - 1.39)$ based on a plot of T_e vs. major radius in Ref. [13]. In the radial interval covered by the spectra in Fig. 6.1 a)-d), this approximation fits the real temperature profile reasonably well.

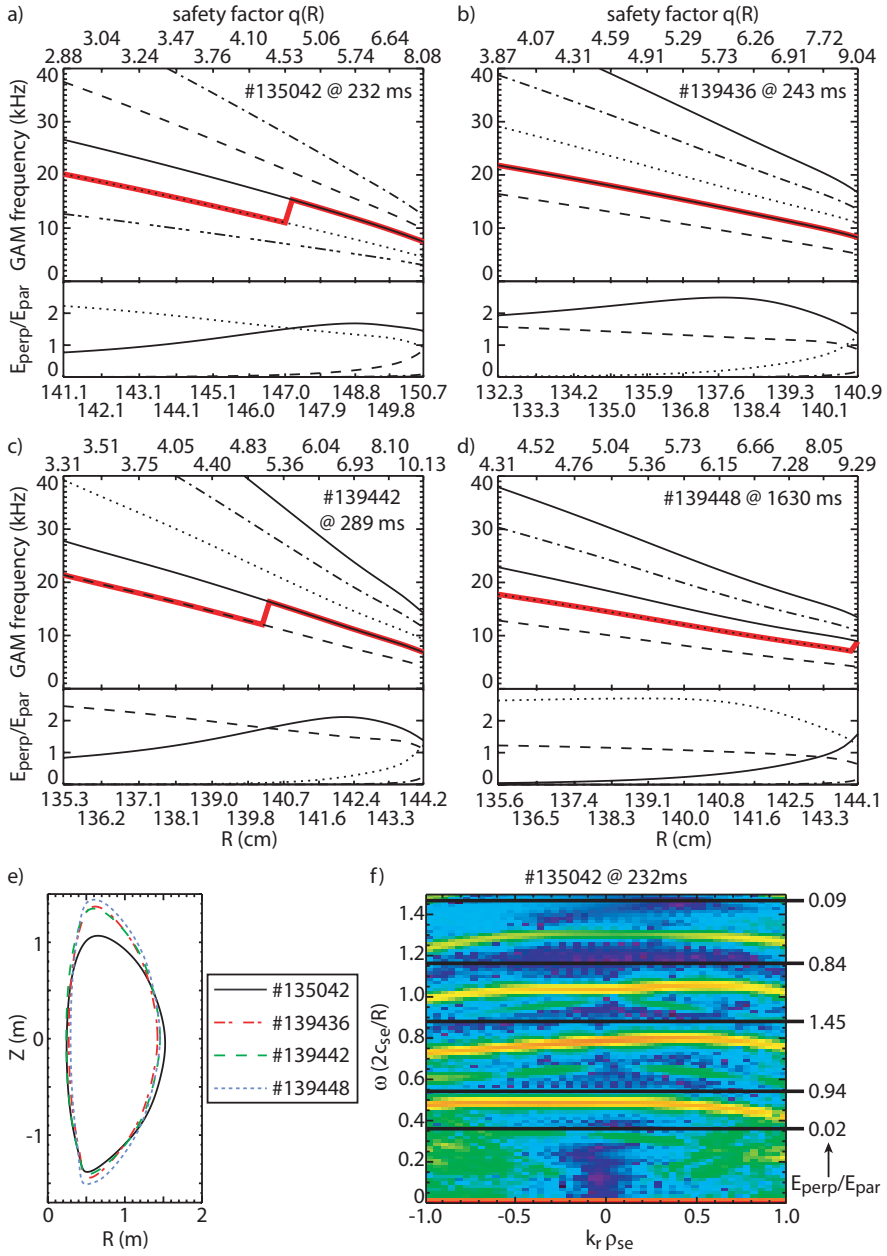

Figure 6.1: a)-d) Eigenfrequencies and corresponding ratios of perpendicular to parallel kinetic energy of the corresponding flow eigenmodes of the linear GAM eigenproblem for NSTX equilibria plotted against major radius and the safety factor. The GAM candidate with the highest ratio of $E_\perp/E_\parallel$ is marked by a thick red line. e) Separatrix shapes of the analysed NSTX discharges. f) Linear NLET computed GAM spectrum for NSTX shot 135042 with the frequencies obtained from the GAM eigenproblem for $k_r = 0$ indicated by the solid lines. The difference between the NLET spectrum and the eigenfrequencies is readily explained by the reduction of γ_e from 5/3 to 1 by the parallel heat conductivity.

Shot	R	d_{sep}	T_e	G_1	ν_1	G_2	ν_2	G_3	ν_3	G_{low}	ν_{low}
135042	150.7	0.8	42	0.64	7.47	0.39	4.6	0.85	9.86	0.26	3.06
139436	140.9	0.7	70	0.55	8.24	0.73	10.93	0.34	5.12	0.22	3.33
139442	144.2	0.7	55	0.51	6.87	0.7	9.3	0.32	4.25	0.21	2.87
139448	144.1	0.6	50	0.7	8.94	0.54	6.86	0.32	4.11	0.21	2.63

Table 6.1: GAM candidates obtained by solving the GAM eigenproblem for $k_r = 0$ for different NSTX shots. Lengths are measured in cm, temperatures in eV and frequencies ν in kHz. Frequencies G are in dimensionless units.

mode has two polarisation directions, which in circular geometry would consist of a $\sin(\theta)$ pressure perturbation with a $\cos(\theta)$ parallel velocity perturbation, and a $\cos(\theta)$ pressure perturbation with a $\sin(\theta)$ parallel velocity perturbation, respectively. The former couples to the poloidal $\mathbf{E} \times \mathbf{B}$-flow and results in the GAM, whereas the latter does not interact with the GAM at all and therefore has $E_\perp/E_\parallel = 0$. Nevertheless, the corresponding mode appears with a non-vanishing ratio $E_\perp/E_\parallel$ in the GAM spectrum of shot 135042, which can be attributed to the lack of up-down symmetry in the experimental NSTX equilibria. Indeed, calculating the flow eigenmodes using an up-down symmetric Miller type equilibrium (see Sec. 2.1.3 and [12]) with parameters similar to those of the actual discharge, i.e. $R = 0.85$, $a = 0.65$, elongation $\kappa = 2$, triangularity $\delta = 0.5$, $q = 8$, $s_\kappa = 0.5$, and differential Shafranov shift $\partial_r R_0 = -0.4$, yield $E_\perp/E_\parallel = 0$. However, adding a small vertical shift of the flux-surfaces in order to break up-down symmetry – as in Sec. 3.7.1 – increases $E_\perp/E_\parallel$ to $4 \cdot 10^{-4}$. Checking shots 139436, 139442 and 139448 explicitly for the mode discussed before, shows that in all three cases, the energy ratio $E_\perp/E_\parallel$ of the mode is only slightly too low (0.01,0.01 and 0.003, respectively) to be included in the plots in Fig. 6.1.

The three most probable GAM candidates at $\Psi_P = 0.98\Psi_{sep}$ and, in addition, the low frequency mode are listed in Tab. 6.1 together with the reference radius of the corresponding flux-surface, the distance to the separatrix, and the electron temperature. Since the numerical solution of the GAM eigenproblem is based on the same equations as the NLET code, linear NLET runs, in which all damping terms such as parallel heat conduction or viscous damping are deactivated (analogous to the linear simulations discussed in the previous chapters), can be expected to agree exactly with the spectra shown in Fig. 6.1 for $k_r = 0$. Nonetheless, linear simulations are useful, since they allow to check for the influence of parallel electron heat conduction on the GAM frequency. As no artificial GAM driving mechanism is implemented in NLET, ion heat conduction cannot be considered in such simulations due to the corresponding high GAM damping rate.

The linear GAM spectrum for shot 135042, including electron heat conduction, is shown in Fig. 6.1 f). For a summary of the parameters used for the NLET simulations discussed here as well as in the following section, see App. D. While the frequencies at zero radial wave number are identical to those shown in Fig. 6.1 a) and listed in Tab. 6.1 for zero heat conductivity κ_e, the frequencies computed with $\kappa_e = 0.174$ are reduced by about 10 %.

This reduction is readily explained by the reduction of the electron adiabatic coefficient from 5/3 to 1, implying that the GAMs behave as in the case of isothermal electrons. However, this does not mean that the electron temperature fluctuations can be neglected in nonlinear NLET runs, since they can be important for the turbulence.
The 'GAM-ness" of the various eigenmodes excited in Fig. 6.1 f) is well reflected in the intensity of the corresponding spectral lines. The GAM frequencies for shot 135042 display only weak dispersion. However, the up-down asymmetry of the magnetic configuration causes an non-vanishing group velocity at $k_r = 0$ in case of GAM candidate 1 with $G_1 = 0.64 \leftrightarrow \omega_{GAM} = 0.88$.
Based on the results of the linear calculations discussed above, it is indeed possible that the phenomenology of the quiet periods observed in NSTX is caused by GAMs and their ability to modulate the turbulence intensity. The three strongest GAM candidates for shot 135042 with $\gamma = 1 \ldots 5/3$ and $T = 42\,\mathrm{eV}$ suggest a frequency interval from $\nu \approx 4 \ldots 11\,\mathrm{kHz}$ in which GAMs are most likely to be observed. Taking into account the frequency reduction by the electron heat conduction, the lower bound of this interval can be lowered to 3.6 kHz, which is close to the frequency measured in NSTX. Another factor that has to be discussed here is the temperature profile. For the calculation of the aforementioned frequencies the temperature on the flux-surface under consideration was used. On the one hand, temperature measurements are not completely accurate and allow the calculated frequencies to vary within the error bars of the temperature diagnostic. On the other hand, it has been shown in Chap. 5 that GAMs may radiate in the radial direction, such that it may well be that the measured frequency belongs to a GAM excited on a flux-surface with lower temperature. The fact that in case of shot 135042 the temperature within $\pm 2\,\mathrm{cm}$ around the separatrix varies between 10 and 100 eV allow for a variation of the frequencies by a factor of roughly 1.5. In addition, there exists a low frequency mode, which in case of shot 135042 has a frequency of rather accurately 3 kHz. Despite its low ratio of perpendicular to parallel kinetic energy, it may nevertheless be excited and modified by the turbulence and thus account for the behaviour observed in experiment.
Therefore, it is indispensable to compare the results obtained from linear calculations with nonlinear turbulence simulations. The computational domain used in these studies is $274\rho_{se} \times 274\rho_{se}$ in radial-toroidal direction and one magnetic connection length in parallel direction. The simulations are fully electromagnetic and include the effects of ion and electron heat conduction, electron inertia, and viscous stresses. The most important parameters are $R = 1.507m$, $\epsilon_n = 0.08$, reflecting the steep gradients in the edge, $\alpha_d = 0.82$, $\epsilon_v = 9 \cdot 10^{-3}$, $\alpha_m = 0.55$, and $\eta_i = \eta_e = 3$. The global shear is $s_g = 8.48$. Figure 6.2 a) shows the resulting poloidal flow profile and the corresponding flow spectrum. A coherent pattern of outward propagating flows oscillating at a low frequency is observed. In contrast to the results presented in the previous chapters, e.g. in Fig. 4.3, no criss-cross flow pattern is excited by the turbulence, which is reflected in the asymmetry of the flow spectrum for this NLET run. The oscillations of the flux-surface averaged poloidal flow in Fig. 6.2 a) is well correlated with the up-down antisymmetric component of the pressure fluctuations as well as the up-down antisymmetric and in-out antisymmetric component of the parallel flow velocity, and the flux-surface averaged heat transport. The correlation with the pressure fluctuations and the modulation of the turbulent heat transport is typical for a

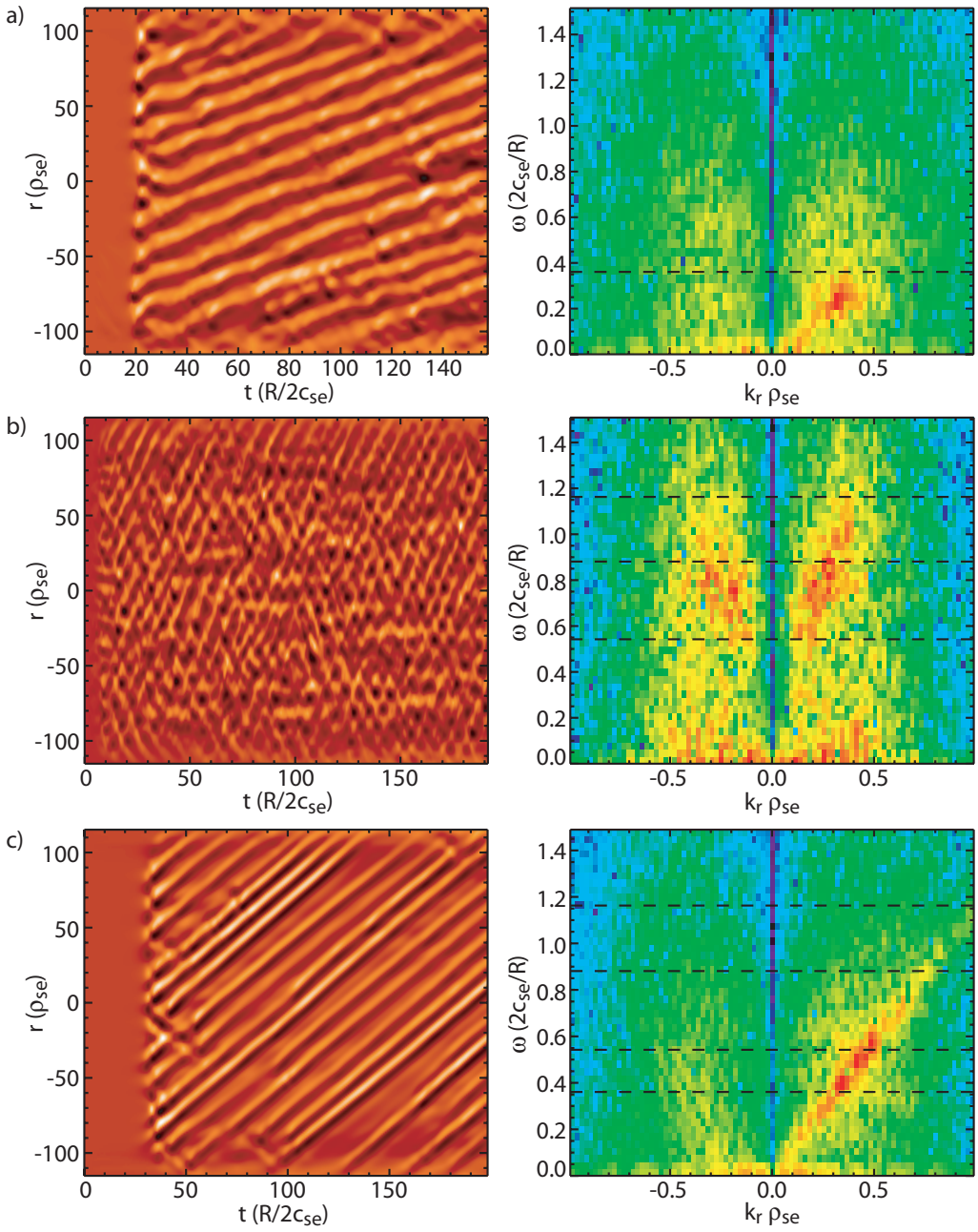

Figure 6.2: Nonlinear NLET runs for NSTX shot 135042. Left: flow profiles. Right: flow spectra. a) A slow GAM oscillation of the flow is observed that may be attributed to the low frequency GAM candidate. The corresponding heat flux profile is strongly modulated by the flow. b) Same parameters as a) but with electron heat conduction disabled. Higher frequency GAMs are excited, which can be ascribed to the strongest GAM candidates instead of the low frequency eigenmode. c) Same parameters as a) but with reduced global shear.

GAM. The RMS amplitudes of the poloidal flow (in the units defined in Chap. 3) and the flux-surface averaged heat flux (in gyro-Bohm units) in the stationary turbulent state are $\bar{v}_E = 7.2$ and $\bar{Q} = 30.6$. Thus, in physical units the average flow velocity is roughly 2 % of the sound speed, i.e. $\bar{v}_E \sim 1\,\mathrm{km/s}$, which is the same order of magnitude as the poloidal flow velocities observed in NSTX [13]. The flow spectrum in Fig. 6.2 a) shows that the frequency of the observed flows is slightly lower than that of the low frequency mode given in Tab. 6.1. However, keeping in mind that this frequency was calculated for $k_r = 0$, that electron heat conduction may lower the GAM frequencies, and that turbulence generally broadens the linear spectra and can influence the dispersion relation, it is plausible to assign the observed oscillation to the low frequency mode. However, the poloidal flow is much stronger than it could be expected to be from the linear value of $E_\perp/E_\parallel$.
In a subsequent NLET run shown in Fig. 6.2 b), the electron heat conduction was deactivated. As a result, GAMs are excited at higher frequencies. The flow spectrum shows activity in a broad range around the three strongest GAM candidates, which are indicated by dashed lines. The RMS flow amplitude is $\bar{v}_E = 21.3$, corresponding to $\bar{v}_E \sim 3\,\mathrm{km/s}$. The RMS heat-flux is $\bar{Q} = 61.5$. As in the NLET run with activated electron heat conduction, the heat-flux is modulated by the flow oscillations. The GAM spectrum in Fig. 6.2 b) is equivalent to that of a corresponding NLET run which neglects the electron temperature fluctuations completely, except for a lower RMS flow of $\bar{v}_E = 12.1$ and an increased heat-flux of $\bar{Q} = 111.7$. In this case, finite electron heat conduction leads to a qualitative change of the observed GAM spectrum, while the electron temperature fluctuations alone cause only quantitative changes.
In another NLET run, the global shear was reduced to $s_g = 3$. The effect is shown in Fig. 6.2 c). The GAM oscillations are very coherent, the spectrum is asymmetric, positive radial wave numbers are preferred. The major part of the intensity in the flow spectrum is concentrated around the low frequency mode and GAM candidate 2 with $G_2 = 0.39$ (see Tab. 6.1). The RMS amplitudes of poloidal flow and heat-flux are lower than in the cases discussed before, $\bar{v}_E = 4.0$ and $\bar{Q} = 9.6$. In contrast to the NLET run shown in Fig. 6.2 a) and b), electron heat conduction is of minor importance. Neglecting electron temperature fluctuations completely does not change the results qualitatively.
Interestingly, the the asymmetry of the flow spectra seems to be a systematic feature of the magnetic geometry. In order to test this statement, the run shown in Fig. 6.2 c) was started with initial noise generated with a modified random seed. Although GAMs with negative k_r are excited in the beginning, the modes with positive k_r always dominate the long term evolution. NLET runs using a high aspect ratio single-null geometry as discussed in Sec. 3.7.1 yield preferred growth of negative k_r if the ion curvature drift is directed towards the X-point and preferred growth of positive k_r if the curvature drift is in the opposite direction (Fig. 6.3 a)). The latter case applies to the results shown in Fig. 6.2.
This behaviour has consequences for non-Boussinesq studies. According to the discussion in Sec. 5.2, the wave number of a GAM wave packet propagating on a significant background temperature gradient increases with time. When a GAM excited at a positive wave number $k_{r,0}$ is shifted to a higher wave number $k_{r,0} + \delta k_r$, the GAM induced shearing rate increases. As a result, the turbulence intensity will be reduced due to the enhanced shearing, which

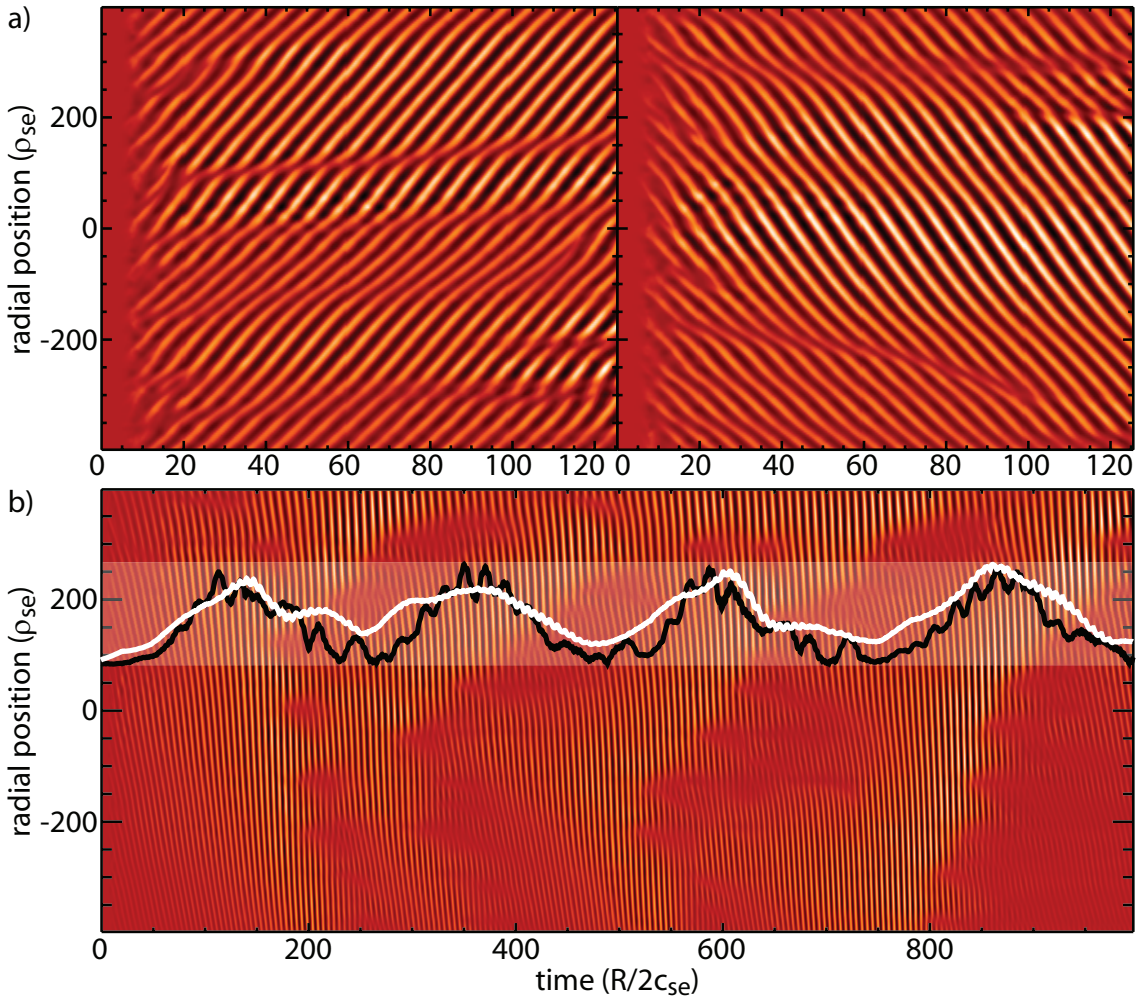

Figure 6.3: Flow profiles of NLET turbulence simulations using the same parameters as in Fig. 5.6 but with a single-null geometry as discussed in Sec. 3.7.1. a) Boussinesq simulation with $\lambda = 10^5$. With the magnetic inhomogeneity drift $\mathbf{v}_d$ pointing away from the X-point (left) only GAMs with positive group velocity are excited. The situation is reversed with $\mathbf{v}_d$ pointing towards the X-point (right). b) Non-Boussinesq simulation with $\lambda = 200$ and $\mathbf{v}_d$ towards the X-point. The negative wave number GAMs excited predominantly by the turbulence are not stable but are shifted towards $k_r = 0$. Where the radial GAM scale approaches $k_r = 0$, GAM activity and turbulent transport are enhanced, which manifests in b) as a slow modulation of the GAM activity. This modulation is correlated to a modulation of the turbulent heat-flux, which is shown by the black and white curves. The black curve is the (scaled) amplitude of the $k_r = 0$ component of the $\mathbf{E} \times \mathbf{B}$ flow within the shaded region. The white curve represents the (scaled) RMS heat-flux within the shaded region, where the modulation of the RMS heat-flux at the GAM frequency has been averaged out.

also means that the GAM drive is reduced. Thus, the GAM amplitude will decrease with increasing shift δk_r. On the contrary, if a GAM excited at $k_{r,0} < 0$ is shifted to higher k_r, the shearing rate decreases until $k_r = 0$, implying that both, the GAM and the turbulence amplitude, increase. As soon as k_r crosses $k_r = 0$, the shearing rate due to the GAM increases again thereby reducing the turbulent heat-flux.
Non-Boussinesq runs of the NLET calculations shown in Fig. 6.3 b) support this consideration. If $\mathbf{v_d}$ is directed away from the X-point, i.e. GAMs are excited predominantly at $k_r > 0$, the system evolves to a stable equilibrium between GAM activity and turbulence level. The flux-surface and radially averaged GAM amplitude and heat-flux are basically constant after an initial phase. However, if $\mathbf{v_d}$ is directed towards the X-point and GAMs are excited at $k_r < 0$, modulations of the GAM activity correlated to oscillations of the turbulent heat flux are observed (Fig. 6.3 b)). The initial GAM pattern displaying a characteristic radial wave number persists only until $t \approx 50$. After this time, the increase of k_r and the GAM activity becomes obvious. The flow profile in Fig. 6.3 b) shows, that the GAM amplitude increases until $k_r = 0$ and then quickly drops. The GAM activity at $k_r > 0$ is negligibly small. In this study, the GAMs not only modulate the turbulence intensity directly (which has been averaged out to obtain the curves in Fig. 6.3 b)) but also indirectly via their radial scale length, which is time-dependent in nonlocal simulations.
The results presented in this section support the hypothesis that the quiet periods in NSTX may be caused by a transport modulation due to geodesic acoustic modes. Linear calculations of the GAM frequency NSTX discharges yielded various GAM candidates, which were classified according to their ratio of perpendicular to parallel kinetic energy. Among the three modes with the highest values of $E_\perp/E_\parallel$, there was one with a frequency between 4 and 5 kHz. This is close to the 3 kHz oscillation observed in the experiment if one keeps in mind that the temperature within the radial window observed by the GPI diagnostic varies strongly. In case of shot number 135042, for example, the temperature ranges from 10 eV to 100 within ± 2 cm around the separatrix [13]. However, one has to be aware of the fact that the observed GAM frequencies depend strongly on the properties of the turbulence, i.e. on the plasma parameters, which are not known accurately.
Additionally, a low frequency mode with $\nu \approx 3$ kHz but lower values of $E_\perp/E_\parallel$ was found for each of the considered discharges. A nonlinear NLET study for discharge 135042 showed, that the low frequency mode can be excited by the turbulence and that it strongly modulates the turbulence level. Furthermore, a mechanism able to modulate the turbulent heat-flux in non-Boussinesq studies was found. But since the modulation observed in the corresponding NLET calculation was much slower than the GAM oscillations, it would be subject to further studies whether this effect could be important for NSTX. However, the numerical observation displays some similarity to the I-phase in ASDEX Upgrade [47], a state in which the turbulence intensity oscillates about five times slower than the GAM.

6.2 GAMs in ASDEX Upgrade

In contrast to the observation of quiet periods in NSTX, whose origin is not finally clear, the observations made in ASDEX Upgrade using Doppler reflectometry can rather cer-

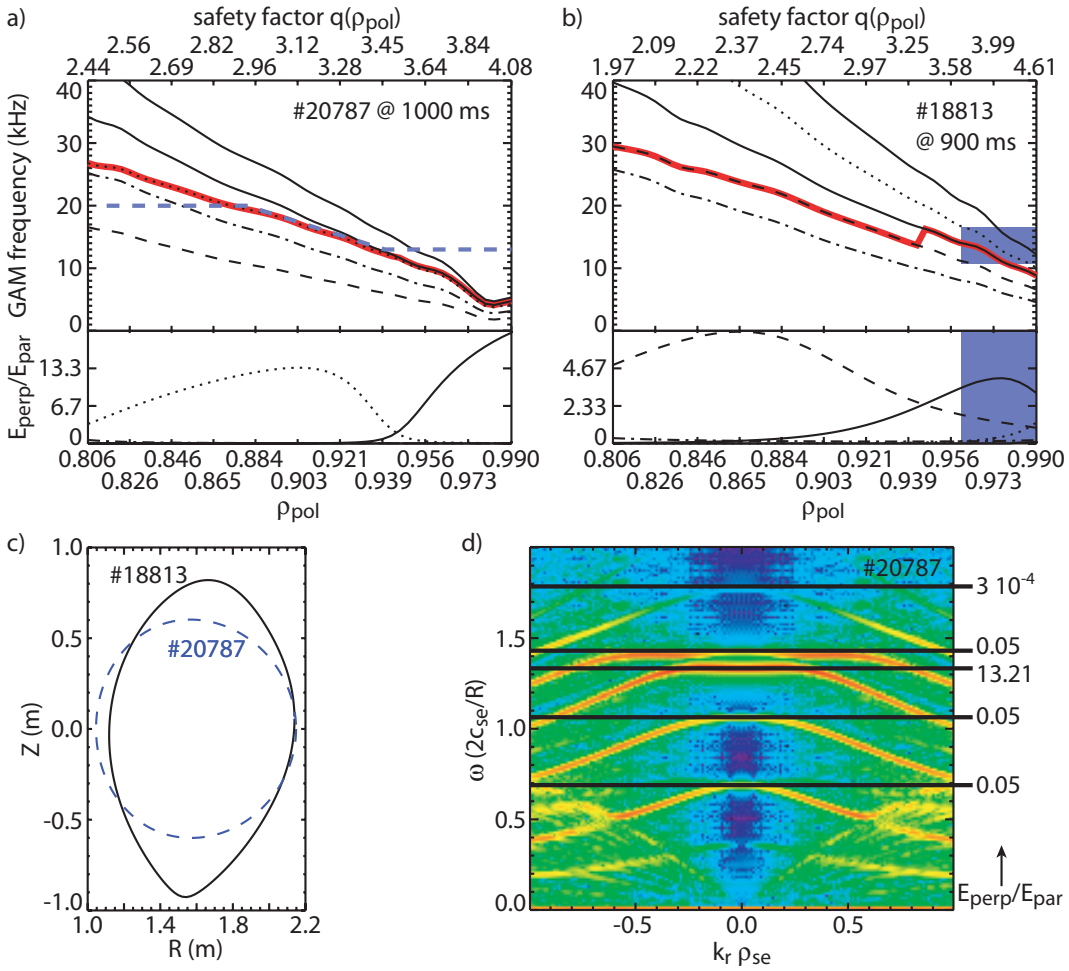

Figure 6.4: a) and b) Eigenfrequencies and corresponding ratios of perpendicular to parallel kinetic energy of the corresponding flow eigenmodes of the linear GAM eigenproblem for ASDEX Upgrade equilibria plotted against ρ_{pol} and the safety factor. The GAM candidate with the highest ratio of $E_\perp/E_\parallel$ is marked by a thick red line. The results of the GAM measurements of Ref. [7] are marked by the dashed blue line in a) and highlighted in blue in b). c) Flux-surface shapes of the analysed ASDEX Upgrade discharges at $\rho_{pol} = 0.995$. d) Linear NLET computed GAM spectrum for ASDEX Upgrade discharge 20787 with the frequencies obtained from the GAM eigenproblem for $k_r = 0$ indicated by the solid lines.

tainly be attributed to geodesic acoustic modes [7, 48]. However, some aspects of those measurements require further theoretical consideration.

First, the measured frequencies deserve some attention. A comparison between experimental GAM frequencies in ASDEX Upgrade and linear GAM frequencies can be found in Ref. [11]. This study applied a Miller type equilibrium [12] with parameters chosen such that the model geometry approximately fitted the real magnetic configuration. The frequencies obtained this way, however, deviated from the experimental results by a factor of up to 2. Of course, this mismatch could be ascribed to the influence of turbulence, where the observations in the previous section may serve as an example, or to inaccuracies of the temperature profiles. On the other hand, an experimental equilibrium exhibits more features that can be covered by the parametrisation proposed by Miller and co-workers in Ref. [12]. Thus, using the data from the equilibrium reconstruction code Cliste [66] for the computation of the linear GAM frequency can be expected to result in a better agreement between theory and experiment.

Another experimental finding concerns the effect of the density pedestal on the GAM activity. According to Ref. [48], discharges with X-point divertor configuration display a steep edge density pedestal whereas the pedestal is much less pronounced in limiter discharges. In the latter case, GAMs are observed within a radial range from $\rho_{pol} \sim 0.75$ to the edge. The inner cut-off can be ascribed to the safety factor, which decreases towards the core implying increasing Landau damping. In the former case, the GAM activity vanishes for $\rho_{pol} \lesssim 0.94$. At this radius, the safety factor in case of shot number 18813 is approximately 3, a value at which GAMs can actually be expected to be excited.

In this context, for the discharges 20787 at $t = 1\,\mathrm{ms}$ and 18813 at $t = 0.9\,\mathrm{ms}$, the linear GAM frequencies are computed and analysed analogous to the previous section by solving the GAM eigenproblem for $k_r = 0$ and by linear NLET simulations. Whether GAMs are excited or not depends in the end on the properties of the turbulence. Therefore, nonlinear NLET runs with parameters based on the experimental data are also analysed.

The shapes of the flux-surfaces at $\rho_{pol} = 0.995$ of the two discharges under consideration are shown in Fig. 6.4 c). Shot 20787 is an inner limiter discharge, shot 18818 a lower single-null divertor discharge. In dimensionless units, the GAM frequency can be expected to be smaller in shot 18813 than in shot 20787 due to the influence of the elongation [11, 7, 39]. However, the more pronounced pedestal of the density and temperature profile in the divertor shot make up for the elongation effect, such that the frequencies in SI units predicted by linear theory are actually higher in the edge for the divertor discharge as is obvious in the spectra shown in Fig. 6.4 a) and b).

The experimental results for shot 20787 are indicated by the dashed, blue line in Fig. 6.4 a), which roughly interpolates the data points shown in Ref. [7]. In the region between the frequency plateaus, around $\rho_{pol} \sim 0.91$, where the GAM frequency was found to scale with the square-root of the temperature, the experimental data agrees very well with the linear prediction. However, in the plateau regions, the frequency deviates from the frequency of the strongest GAM candidate. It is smaller than the linear value at the inner plateau and larger at the outer plateau. Taking into account that the density and temperature profiles become steeper towards the edge, reflected in ϵ_n decreasing from 0.187 at $\rho_{pol} = 0.84$ to

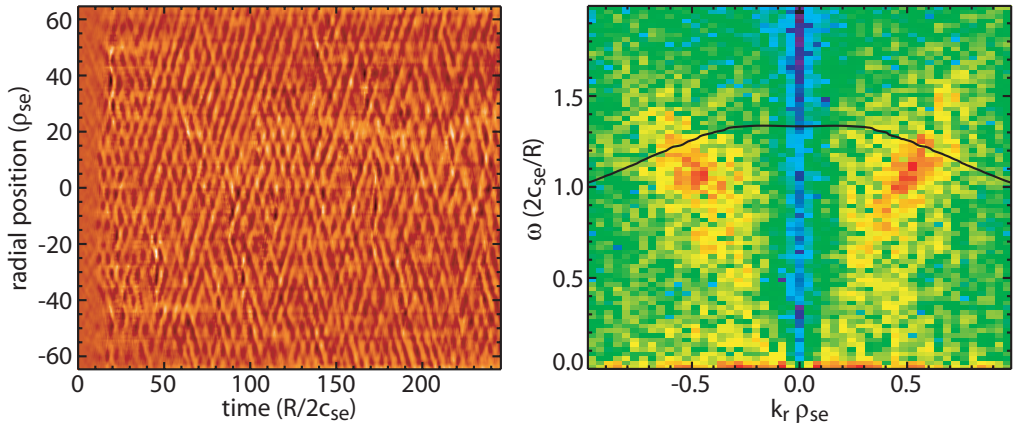

Figure 6.5: Results of a nonlinear NLET run for ASDEX Upgrade discharge 20787 at $\rho_{pol} = 0.91$. Left: flow profile. Right: flow spectrum. Coherent GAM activity is observed in the flow profile. The corresponding spectrum displays two symmetric, broad but still clear GAM activity peaks. The corresponding frequency is 13.7 kHz. The linear frequency of the strongest GAM candidate, shown in Fig. 6.4 d), is indicated by the solid line in the flow spectrum.

0.026 at $\rho_{pol} = 0.97$, this behaviour might be caused by the nonlinear effects on the GAM dispersion discussed in the Chap. 5.

However, there is more than one GAM candidate that can be excited by the turbulence and could therefore account for the experimental observations, though $E_\perp/E_\parallel$ for the main GAM candidate is at least a factor 100 higher than for all other GAM candidates, which makes the first hypothesis seem more plausible. The flow spectrum obtained by a linear NLET run for shot 20787 at $\rho_{pol} = 0.91$ is shown in Fig. 6.4 d) with the frequencies obtained from the GAM eigenproblem for $k_r = 0$ indicated by solid lines. As discussed in the previous section, electron heat conduction in this case makes the GAM behave as in a system with isothermal electrons.

In case of shot 18813 the experimental GAM frequencies are distributed in the highlighted region in Fig. 6.4 b). Again, the experimental results show good agreement with the linear predictions. This, however, does not explain the suppression of the GAM for $\rho_{pol} \lesssim 0.94$. This has to be investigated in nonlinear NLET runs.

Coherent GAMs with intensities well above the turbulent background are found in a nonlinear NLET run for shot 20787 at $\rho_{pol} = 0.91$, shown in Fig. 6.5. The observed frequency corresponds to 13.7 kHz, which is 17 % lower than the frequency of the strongest GAM candidate. From the nonlinear simulation, it is not clear, to which GAM candidate the observed GAM can be ascribed. The linear frequency of the strongest GAM candidate indicated by the solid line in the flow spectrum in Fig. 6.5 could serve to explain the intensity obtained from the simulation.

In any case, the nonlinear NLET runs for shot 20787 at $\rho_{pol} = 0.84$, 0.91 and 0.97 largely agree with the linear predictions. The corresponding GAM frequencies are 17.8, 13.7, and

9.4 kHz, where the first two values are smaller and the last one is larger than the frequencies predicted by linear theory. The RMS amplitudes of the poloidal flow are 0.3, 0.5, and 2.4 km/s, where the first two values are of the same order as the GAM amplitudes given in Ref. [7].
The nonlinear runs for shot 18813 at $\rho_{pol} = 0.88$, 0.97, and 0.99 – except at $\rho_{pol} = 0.97$ – show weak GAM activity. Nevertheless the observed frequencies agree reasonably with the linear values. At $\rho_{pol} = 0.88$, weak GAMs with intensities of the order of the turbulent background are found at a frequency between 15 and 20 kHz. At $\rho_{pol} = 0.97$, GAMs with $\nu \approx 10$ kHz are found, and at $\rho_{pol} = 0.99$ $\nu \approx 3 \ldots 7$ kHz. The RMS flow velocities are of order 0.5 km/s. The GAMs observed in the nonlinear NLET run at $\rho_{pol} = 0.88$ are weak. The low intensity can be traced back to the viscous stress term in the vorticity equation (see [14]), which can counteract the coupling of the poloidal flow to the $m = 1$ pressure sideband. The coefficient γ_p of the viscous stress mainly depends on the background temperature and ϵ_n. Since the gradients in case of shot 18813 are much steeper than those of shot 20787, γ_p at $\rho_{pol} = 0.88$ is 1.75 whereas for shot 20787 γ_p is only 0.68 at $\rho_{pol} = 0.84$. In order to verify this hypothesis, two nonlinear NLET runs have been started – for simplicity neglecting electron temperature fluctuations – one with $\gamma_p = 1.75$ and one with $\gamma_p = 0$. In the former case, no GAM activity is found. However, with deactivated viscous stress, strong, coherent GAMs are excited by the turbulence at a frequency of 20.8 kHz.
Concluding, the linear as well as the nonlinear results obtained with NLET two-fluid simulations show, overall, good agreement with ASDEX Upgrade data. However, one has to be aware of the sensitive dependence of the observed GAM frequencies and intensities on the properties of the turbulence, which in turn depend on the applied parameters. Since the simulation parameters are calculated from experimental data, which is subject to measurement errors (especially the gradient scale lengths), the numerical studies discussed here cannot reproduce exactly the experimental results. However, in conjunction with the characteristics of the GAMs discussed in Chaps. 3 to 5, the above results reflect the behaviour observed in experiment relatively well.

Chapter 7

Summary and conclusions

Their ability to control the turbulent transport of heat and particles out of the confinement region makes GAMs an interesting topic for magnetic confinement fusion research. The key issue of this thesis, was the radial propagation of GAMs, which is important for the interpretation of the experimental GAM frequency profiles in ASDEX Upgrade and TEXTOR. Furthermore, GAM propagation and its implications on the existence and position of reflection and absorption layers might be a relevant factor for the excitation of GAMs by externally applied electromagnetic fields (see Refs. [8, 9]).

In Chap. 3 (see also Refs. [41, 42]), an elegant way of calculating the radial group velocity of the GAM via its free energy or Poynting flux was developed, which provides theoretical insight into the mechanisms of GAM propagation. Considering the GAM as a wave packet, whose energy is transported with its group velocity, the radial propagation velocity was computed as the ratio of the energy-flux of the GAM to its total energy. In the first step, the GAM energy-flux was calculated in a two-fluid framework for cold ions, infinite safety factor and circular flux-surfaces, and two kinds of transport mechanisms have been identified. The curvature energy-flux, which represents the advection of the free energy of the fluctuations with the magnetic inhomogeneity drift, $\langle v_{d,r} E_{fluc} \rangle$, is always parallel to the phase velocity. However, the polarisation energy flux, $\langle -k_r^2 \rho_{se}^2 v_p E_{fluc} \rangle$, is always antiparallel to the phase velocity. Therefore, the one of the two fluxes which is dominant controls the propagation direction of the GAMs, and thus the form of the dispersion relation. This result has been generalised to include ion temperature and parallel flows and to a gyrokinetic model, in which equivalent energy transport mechanisms have been found.

In the second step, the group velocity, which is given by the ratio of the Poynting flux to the total free energy, has been evaluated for circular high aspect ratio flux surfaces and estimated for elliptic plasmas. The results agree with NLET and GYRO computations and alternative analytical calculations of the GAM dispersion. For cold ions, group and phase velocity have been found to be opposite. For $\tau \gtrsim 0.2$ or $\kappa \gtrsim 1.5$, they are parallel. The magnetic inhomogeneity energy-flux requires an up-down asymmetry of E_{fluc} to give non-zero values. In case of up-down symmetric flux surfaces, the asymmetry is of order $k_r \rho_{se} E_{fluc}$, which makes the curvature energy-flux comparable to the polarisation energy-

flux. Therefore, the group velocity $v_{g,r} = \langle S_r \rangle / \langle E_{fluc} \rangle$ is of order $k_r \rho_{se} v_d$, i.e. much smaller than the magnetic inhomogeneity drift.
Due to resonances with magnetic drift modes (not drift waves) and sound waves, the propagation speed of GAMs is limited. Close to such a resonance, the poloidal rotation becomes negligible compared to the remaining degrees of freedom, as the amplitudes of density and temperature, or parallel flow velocity diverge. The characteristics of the resulting mode are completely determined by the resonant mode, and it should not be called GAM any longer. The resonances restrict GAMs to $k_r \ll 1$ and $q \gg 1$ and limit the group velocity.
Since the GAM induced pressure fluctuations are drastically reduced at the X-point of single-null configurations, which are common in today's experiments, the curvature energy-flux becomes of order $v_d E_{fluc}$ and outweighs the other energy-fluxes. Therefore, GAMs can be expected to propagate at the magnetic drift velocity. Because usually v_d is directed towards the X-point, GAMs would propagate radially inward in this case.
However, a generalisation of the two-fluid expression for the Poynting-flux of GAMs in the cold ion and infinite safety factor limit with large aspect ratio circular flux-surfaces to arbitrary toroidal geometries, furthermore, yielded an additional component of the polarisation energy-flux of order $v_d E_{fluc}$. Together with the curvature energy-flux of the same order – discussed above – it generally leads to a non-vanishing group velocity at $k_r = 0$, whose sign and magnitude depend on the ratio of ion to electron temperature τ and the magnetic geometry. Analogous terms have been found in the generalised gyrokinetic expression of the GAM Poynting flux.
The geometry and temperature dependencies of $v_g(k_r = 0)$ have been studied numerically using the two-fluid code NLET, and the gyrokinetic codes GS2 and GYRO as well as analytically by deriving a group velocity estimate for arbitrary τ in a two-fluid framework. By means of the estimate, it was found that it is important for the energy transport at large aspect ratios, whether the vertical magnetic forces on the flux-surfaces balance or not. While in the former case, the energy of GAMs is transported essentially by the magnetic inhomogeneity drift – which confirms the conjecture made before, that in single-null geometry $v_g(k_r = 0)$ has the sign of $v_{d,r}$ at the position opposite to the X-point – the polarisation energy-flux might become important in the latter case.
In order to achieve a high GAM group velocity ($\sim v_d$), the magnetic geometry should be up-down asymmetric and have a maximum of the poloidal magnetic field – corresponding to the flux-surfaces being close to each other – at a poloidal position where the magnetic inhomogeneity drift has a significant radial component. By adding an indentation coil – with a current opposite to the elongation currents – to the single-null geometry used in Sec. 3.7.1, which pushes the flux-surfaces closer together opposite to the X-point, the observed group velocities increased by a factor of three. In a real device, such a configuration could be generated by appropriately combining the plasma shaping coils, for example in DIII-D, where the shaping system is located close to the plasma [67].
Altering the direction and speed of the GAM propagation might be used to search for its potential influence on the confinement and even on the H-mode. For example, it would be interesting to determine whether the dependence of the H-mode power-threshold on the magnetic drift direction [45] is really due to its relation to the X-point or possibly rather due to its influence on the GAM propagation direction.

Calculating the group velocity by means of the Poynting flux turns out to be advantageous compared to a direct calculation of the GAM dispersion relation because only lowest order approximations of the fluctuations are required to gain insights into effects induced by ion temperature, sound waves or magnetic geometry. Requiring relatively little effort, the energy approach allowed for a rather accurate calculation of the group velocity for circular high aspect ratio geometry and for the derivation of estimates for elliptic Miller equilibria and even for single-null configurations. The radial propagation of GAMs due to their linear dispersion relation was found to be slow compared to the typical velocity scale of the turbulent motions, the diamagnetic velocity, in all considered cases. However, much higher group velocities are possible in turbulent systems, which was discussed in Chap. 5.
Due to the additional two dimensions in gyrokinetic theory, fluid simulations can be much more economic for problems requiring highly resolved computational grids. In order to check for a potential influence of kinetic effects and to justify the use of a two-fluid code for the succeeding numerical turbulence studies, the results obtained in linear and nonlinear studies with the two-fluid code NLET and the gyrokinetic code GYRO were compared for three parameter sets in Chap. 4. The Cyclone base case parameters, which represent the tokamak core plasma, and two parameter sets, which are better adapted to the situation in the plasma edge, allowed for studying the transition from stationary zonal flows in the core to GAMs in the edge.
First, the growth rate of the fastest growing instability was calculated. In case of the two edge parameter sets the gyrokinetic and two-fluid growth rates agreed very well for small poloidal wave numbers up to about $k_y\rho_{se} \sim 0.5$. For higher wave numbers, the two-fluid growth rates break down as a consequence of the fluid approximation, which excludes small scale fluctuations at the scale of the gyro radius and below. In case of the cyclone base case, the two-fluid growth rates agree with the gyrokinetic results only up to $k_y\rho_{se} \sim 0.2$ but increase to larger values than in the gyrokinetic case for $k_y\rho_{se} > 0.2$. This may, however, be explained by an underestimation of the collisionless damping effects by the parameters used to model collisionless damping in the NLET code.
Good qualitative agreement was observed in the turbulence simulations. In case of the Cyclone base case parameters, especially due to the low safety factor and the corresponding Landau damping, GAMs are suppressed in the gyrokinetic and the two-fluid codes. The $\mathbf{E}\times\mathbf{B}$ flow spectrum was dominated by stationary flows. The turbulent heat-fluxes agreed reasonably well, where the fluid heat-flux was about 26 % smaller than the gyrokinetic one, which confirmed the result of an earlier comparison [61]. In case of the two edge parameter sets, GAMs were dominant in the flow spectrum. The excited radial wave numbers and frequencies were similar. The average fluid heat-flux for the first edge parameter set deviated by only 8 % from the gyrokinetic value. In case of the second edge parameter set, which corresponds to steeper edge background profiles than the first one, the fluid heat-flux was roughly a factor of 3 higher than the gyrokinetic heat-flux. The observed differences, however, could be attributed to collisionless damping effects, which are not retained in the two-fluid approximation. A modification of the parallel heat conductivities in NLET in order to model collisionless damping, which is more important in the core than in the edge plasma, the heat-flux could be reduced considerably.
In summary, the turbulence studies with GYRO and NLET display good quantitative

agreement. The increasing GAM activity during the transition from core to edge parameters is well reproduced by both codes and the quantitative differences between the results can be ascribed to the differences between the gyrokinetic and the fluid approach, which have been discussed in Sec. 2.2.3. The interaction between the turbulence and the GAMs does not seem to be changed drastically by kinetic effects.

Geodesic acoustic modes are driven by the turbulence. However, the turbulent drive is not only the energy source for the GAM; it can also modify its frequency. An experimental example for such behaviour is given by GAM measurements in ASDEX Upgrade and also in TEXTOR [7, 48, 64], where the GAM frequency was observed to be constant over a certain radial range instead of scaling with the square-root of the background temperature. Taking up a theoretical discussion by Itoh [10] of such behaviour – which was referred to as GAM eigenmodes – the radial mode structure of GAMs on a strongly varying temperature background was studied analytically and numerically applying the NLET code in Chap. 5. The radial mode structure and its dependence on the GAM dispersion relation was discussed analytically on the basis of an approximate dispersion relation of the form $\omega_{GAM}(r, k_r) = \omega_{GAM,0}(r)(1 + \alpha k_r^{\beta})$ for $k_r \rho_{se} \ll 1$. The strength of the dispersion relation, i.e. the radial group velocity, is determined by α, the form of the dispersion is given by β. As discussed in Chap. 3, for up-down symmetric flux surfaces, the GAM frequency can be assumed to depend quadratically on k_r whereas the frequency depends linearly on the radial wave number in case of up-down asymmetric magnetic configurations. The distance a GAM can propagate radially before being damped is equivalent to the radial mode width of a GAM fulfilling the condition $\omega_{GAM}(r, k_r) = \text{const}$. In case of a weak dispersion ($\alpha \sim 0.1\rho_{se}$), as obtained in the linear GAM calculations in Chap. 3, the mode width of such a mode is small (several gyro radii, depending on the background temperature gradient). However, the factor α can be enhanced significantly by the turbulence.

Therefore, a method to measure the nonlinear GAM dispersion using the results of non-Boussinesq turbulence calculations was developed. The approximate dispersion relation was used to derive an expression for the wave front of a GAM with a specific frequency, i.e. a curve of constant phase. By fitting this expression to a wave front obtained from a non-local numerical calculation, the strength and form of the dispersion relation can be measured.

Nevertheless, since the linear GAM dispersion relation is known, the propagation of GAMs was studied first with linear NLET calculations to develop a basic understanding of the influence of the non-constant temperature background. In case of a quadratic dispersion relation ($\beta = 2$), the temperature gradient was shown to accelerate the radial motion of the GAMs by shifting their radial wave number to higher values while the frequency remained constant. The temperature gradient is, therefore, able to induce a reflection layer for the GAMs. Depending on the dispersion relation (here: the sign of α), it is possible that GAMs can, overall, propagate only radially outward or only radially inward. If group and phase velocity are in the same direction, the GAM propagates radially outward and vice versa.

The method for measuring the nonlinear GAM dispersion was then applied for a non-Boussinesq, nonlinear NLET run which displayed a very strong dispersion. The observed group velocity was much higher than the linear one ($\alpha = 109$) resulting in GAM frequen-

cies deviating by up to 30 % from the frequencies predicted by the $\sqrt{T}$ scaling. The corresponding dispersion relation was verified with a turbulence study applying the Boussinesq approximation. The nonlinear term responsible for the modification of the linear dispersion was identified as the up-down asymmetric component of the density transport. The nonlinear dispersion was measured additionally for the two GAM simulations discussed in Chap. 4. The finding that eigenmodes propagate radially inward in case of shallow gradients of the background density and temperature and radially outward in case of steep gradients, suggests a possible dependence of the direction of the GAM group velocity on the parameter $\epsilon_n = 2L_n/R$, which controls the steepness of the background density and temperature profiles. Thus, the results of Chap. 5 can provide an explanation of the frequency plateaus observed in ASDEX Upgrade. Another conclusion can be drawn from the parameter dependence of the GAM dispersion relation. If the sign of α changes, an absorption layer at the radial position where $\alpha = 0$ results, close to which GAMs are expected to be strongly damped due to resonance and phase mixing effects. This reminds of a GAM amplitude profile measured in TEXTOR, which displayed a sharp amplitude drop in a radial region, where the measured GAM frequency scaled with $\sqrt{T}$, i.e. in a region with weak dispersion, where a sign change of α is possible.

Finally in Chap. 6, linear and nonlinear NLET studies using experimental equilibrium data were compared to experimental results of NSTX and ASDEX Upgrade. The study for NSTX was motivated by the observation of periodically appearing quiet periods, in which the turbulence intensity during the L-mode was reduced to the turbulence level usually observed during the H-mode. Since GAMs are likely to modulate the turbulence intensity given they are strong enough, the question arose, whether the quiet periods could be attributed to geodesic acoustic modes. Complicated magnetic configurations as in NSTX, due to the complex coupling of the poloidal flow to the sound wave spectrum, allow for the existence of more than one mode displaying the character of a GAM. Which one of these modes is excited in the end depends on the properties of the turbulence. Indeed, the results discussed in Chap. 6.1 would be consistent with a GAM oscillation at the frequency of the quiet periods. Each of the analysed NSTX discharges exhibited a low frequency mode, whose frequency is close to the frequency of the quiet periods. Nonlinear NLET runs further showed, that this mode can be excited by the turbulence and is able to modulate the turbulent heat flux. However, slight changes of the simulation parameters can result in the excitation of a different GAM mode. Thus, being aware of the strong dependence of GAM excitation on the turbulence properties and on the simulation parameters, which cannot be measured exactly in experiment, it can be summarised that the quiet periods observed in NSTX may be caused by GAMs. However, further experiments are needed to give the final answer to this question.

Another mechanism leading to a modulation of the turbulent heat-flux was identified. The GAM spectra for the experimental NSTX equilibria – lower single-null divertor discharges – displayed an asymmetry between positive and negative k_r, which was found to be independent of the random seed used for the initialisation of the NLET simulations. GAMs with negative k_r were nearly completely suppressed. Local NLET turbulence studies using the simple single-null model introduced in Chap. 3 showed that the asymmetry in the GAM amplitudes for positive and negative radial wave numbers were related to the direc-

tion of the magnetic inhomogeneity drift relative to the position of the X-point. When the magnetic inhomogeneity drift was directed towards the X-point, relaxing the local limit resulted in a slow (compared to the GAM period) modulation of the turbulent heat-flux which was related to the change of the radial scale length of the GAMs due to their propagation (see the discussion in Chap. 5). Since the magnetic drift was, indeed, directed towards the X-point in all NSTX discharges analysed in Ref. [13], the observed nonlocal effect might also be relevant for the quiet periods. The numerical observation also displays some similarity to the I-phase in ASDEX Upgrade [47], a state in which the turbulence intensity oscillates about five times slower than the GAM.

Being aware of the strong dependence of GAM excitation on the turbulence properties and thus on the simulation parameters, which cannot be measured exactly in experiment, it can be summarised that the quiet periods observed in NSTX may be caused by GAMs. However, further experiments are needed to give the final answer to this question.

The study for ASDEX Upgrade was intended on the one hand to check whether agreement between theory and experiment concerning the observed GAM frequencies can be obtained using experimental equilibrium data. An earlier comparison of numerical and experimental frequencies using a Miller type geometry for the calculation of the two-fluid GAM frequency yielded significant differences [11]. Another question concerned the experimental observation that the radial range in which GAMs can be measured is reduced to a narrow region in the edge in case of pronounced density and temperature pedestals, while GAMs can be measured in a wide radial domain if the edge pedestals are less pronounced. The linear frequencies agreed very well with the experimental values within the limitations set by the accuracy of the equilibrium data and the temperature profiles. An explanation for the aforementioned frequency plateaus can be seen in the nonlinear modifications to the GAM dispersion relation discussed in Chap. 5. A continuous change of the dispersion parameter α with the plasma parameters from $\alpha > 0$ in the edge to $\alpha < 0$ in the core can result in a similar frequency profile. Nonlinear, local NLET runs displayed no significant differences concerning the observed GAM frequencies. An explanation for the narrow region of GAM activity in case of a pronounced profile pedestal could be given, considering the results obtained with NLET, by studying effect of viscous stresses, which increases for steeper profiles and higher temperature. Thus, viscous damping of the GAM becomes important relatively close to the last closed flux surface in case of a pronounced pedestal whereas in the absence of a pedestal, this damping term becomes relevant only further inside the plasma. Nonlinear NLET runs with the viscous stress deactivated indeed yielded considerable GAM activity.

In summary, the propagation properties of the GAM in linear as well as in turbulent systems were extensively discussed including also magnetic geometry and non-Boussinesq effects. It was shown that GAM propagation can be relevant in experiments, e.g. concerning the origin of the frequency plateus observed in ASDEX Upgrade [7], especially in cases in which the turbulence strongly enhances the radial GAM group velocity. This finding as well as the observed wavenumber dependence of the nonlinear GAM growth rate, which requires the use of precise magnetic geometry data, are of special interest for further research due to the possible consequences for experiments, e.g. for the quiet periods in NSTX [13] or the I-phase in ASDEX Upgrade [47].

Appendix A

Metric coefficients of Mercier-Luc geometry

The Mercier-Luc coordinate system $(\xi^i) = (\rho, l, \zeta)$ and its relation to cartesian coordinates is given by

$$\begin{aligned} R &= x^2 + y^2 = R_s(l) + \rho\sin(\vartheta(l)), \\ Z &= z = Z_s(l) + \rho\cos(\vartheta(l)), \\ \phi &= -\zeta = \arctan\left(\frac{y}{x}\right). \end{aligned} \tag{A.1}$$

The Jacobi matrix is

$$J^{ij} = \left(\frac{\partial\xi^i}{\partial x^j}\right) = \begin{pmatrix} \cos(\zeta)\sin(\vartheta) & -\sin(\zeta)\sin(\vartheta) & \cos(\vartheta) \\ \frac{\cos(\zeta)\cos(\vartheta)}{1-\rho/R_c} & -\frac{\sin(\zeta)\cos(\vartheta)}{1-\rho/R_c} & -\frac{\sin(\vartheta)}{1-\rho/R_c} \\ -\frac{\sin(\zeta)}{R} & -\frac{\cos(\zeta)}{R} & 0 \end{pmatrix}, \tag{A.2}$$

where $1/R_c = \mathrm{d}\vartheta/\mathrm{d}l$. The calculation of the metric tensor results in

$$g_{ij} = \left(\frac{\partial x^k}{\partial\xi^i}\frac{\partial x^k}{\partial\xi^j}\right) = \begin{pmatrix} 1 & 0 & 0 \\ 0 & (1-\rho/R_c)^2 & 0 \\ 0 & 0 & R^2 \end{pmatrix}. \tag{A.3}$$

Thus, the Jacobian $J = \det(J^{ij}) = (\det(g_{ij}))^{-1/2}$ is

$$J = \frac{1}{\sqrt{g}} = -\frac{1}{R(1-\rho/R_c)}. \tag{A.4}$$

Finally, with $(\nabla f)^i = g^{ij}(\partial f/\partial\xi^j)$ and $\nabla\cdot\mathbf{A} = J(\partial/\partial\xi^i)(A^i/J)$ the Grad-Shafranov operator becomes

$$R^2\nabla\cdot(R^{-2}\nabla\chi) = JR^2\frac{\partial}{\partial\xi^i}\left(\frac{g^{ij}}{JR^2}\frac{\partial\chi}{\partial\xi^j}\right), \tag{A.5}$$

which after substitution of the metric coefficients results in the left-hand-side of Eq. (2.19).

Appendix B

Calculations for chapter 2.2

B.1 Equations of motion in gyrokinetic theory

The equations of motion of the phase-space variables $\mathbf{X}$, U, μ and γ used in the derivation of the gyrokinetic equation (2.53) have been given in Eqs. (2.44)-(2.47) without proof. The derivation of those equations as well as of their gyroaverages is demonstrated in the following.
The necessary equations of motion can be obtained as

$$\frac{\mathrm{d}A}{\mathrm{d}t} = \left.\frac{\mathrm{d}A}{\mathrm{d}t}\right|_{\mathbf{v}} + \frac{\mathrm{d}\mathbf{v}}{\mathrm{d}t}\cdot\frac{\partial A}{\partial \mathbf{v}}, \tag{B.1}$$

where the first term on the right hand side is the total time derivative at fixed velocity and the total time derivative of the velocity $\mathbf{v}$ is given by the Lorentz force Eq. (2.28), which can be expressed as

$$\frac{\mathrm{d}\mathbf{v}}{\mathrm{d}t} = \frac{q}{m}\mathbf{E} - \Omega s\hat{\boldsymbol{\rho}} + \frac{q}{mc}\mathbf{v}\times\mathbf{B}_1. \tag{B.2}$$

The partial time derivative of $\mu = mv_\perp^2/2B_0 = m(v^2 - v_\parallel^2)/2B_0$ at fixed velocity is zero since the unperturbed quantities are assumed stationary. The partial velocity derivative of μ is $\partial\mu/\partial\mathbf{v} = m\mathbf{s}/B_0$. Therefore,

$$\begin{aligned}\left.\frac{\mathrm{d}\mu}{\mathrm{d}t}\right|_{\mathbf{v}} &= \mathbf{v}\cdot\left(-\frac{mv_\perp^2}{2B_0^2}\nabla B_0 - \frac{m}{2B_0}\nabla(\mathbf{b}\cdot\mathbf{v})\right)\\ &= -\frac{\mu}{B_0}\mathbf{v}\cdot\nabla B_0 - \frac{mu}{B_0}\mathbf{s}\cdot((\mathbf{v}\cdot\nabla)\mathbf{b}).\end{aligned} \tag{B.3}$$

Combining the results above, Eq. (2.44) is obtained:

$$\begin{aligned}\frac{\mathrm{d}\mu}{\mathrm{d}t} &= \dot{\mu}_0 + \dot{\mu}_1 \sim \omega_t\mu + \Delta\Omega\mu,\\ \dot{\mu}_0 &= -\frac{\mu}{B_0}\mathbf{v}\cdot\nabla B_0 - \frac{mu}{B_0}\mathbf{s}\cdot(\mathbf{v}\cdot\nabla)\,\mathbf{b} + \frac{q}{B_0}\mathbf{s}\cdot\mathbf{E}_0,\\ \dot{\mu}_1 &= \frac{q}{B_0}\left(\mathbf{s}\cdot\mathbf{E}_1 - \frac{us}{c}\hat{\boldsymbol{\rho}}\cdot\mathbf{B}_1\right).\end{aligned} \tag{B.4}$$

For $\partial\gamma/\partial\mathbf{v}$ one has

$$\frac{\partial\hat{\mathbf{s}}}{\partial\mathbf{v}} = \frac{1}{s} \tag{B.5}$$

and

$$\frac{\partial\hat{\mathbf{s}}}{\partial\mathbf{v}} = \frac{\partial}{\partial\mathbf{v}}\left(\cos(\gamma)\hat{\mathbf{e}}_2 - \sin(\gamma)\hat{\mathbf{e}}_3\right) = -\hat{\boldsymbol{\rho}}\frac{\partial\gamma}{\partial\mathbf{v}}. \tag{B.6}$$

Thus, $\partial\gamma/\partial\mathbf{v} = -\hat{\boldsymbol{\rho}}/s$. For the calculation of $(\mathrm{d}\gamma/\mathrm{d}t)|_{\mathbf{v}}$, it is recalled that at fixed velocity $\mathrm{d}\mathbf{v}/\mathrm{d}t = 0$. Therefore,

$$0 = \hat{\boldsymbol{\rho}}\cdot\frac{\mathrm{d}}{\mathrm{d}t}(\mathbf{u}+\mathbf{s}) = -\left.\frac{\mathrm{d}\gamma}{\mathrm{d}t}\right|_{\mathbf{v}} + \hat{\mathbf{e}}_3\cdot(\mathbf{v}\cdot\nabla)\hat{\mathbf{e}}_2, \tag{B.7}$$

and the equation of motion of γ results in

$$\begin{aligned}
\frac{\mathrm{d}\gamma}{\mathrm{d}t} &= \omega_0 + \omega_1 \sim (\Omega+\omega_t) + \Delta\Omega,\\
\omega_0 &= \Omega + \hat{\mathbf{e}}_3\cdot(\mathbf{v}\cdot\nabla)\,\hat{\mathbf{e}}_2 + \frac{u}{s}\hat{\boldsymbol{\rho}}\cdot(\mathbf{v}\cdot\nabla)\,\mathbf{b} - \frac{q}{ms}\hat{\boldsymbol{\rho}}\cdot\mathbf{E}_0,\\
\omega_1 &= -\frac{q}{ms}\hat{\boldsymbol{\rho}}\cdot\mathbf{E}_1 + \Omega\left(\mathbf{b} - \frac{u}{s}\hat{\mathbf{s}}\right)\cdot\mathbf{B}_1.
\end{aligned} \tag{B.8}$$

The straightforward calculation of $\mathrm{d}U/\mathrm{d}t$ yields

$$\frac{\mathrm{d}U}{\mathrm{d}t} = q\frac{\partial\Phi_1}{\partial t} - \frac{q}{c}\mathbf{v}\cdot\frac{\partial\mathbf{A}_1}{\partial t} \sim \Delta\omega_t U. \tag{B.9}$$

Some care has to be taken when calculating the guiding centre motion

$$\frac{\mathrm{d}\mathbf{X}}{\mathrm{d}t} = \mathbf{v}\cdot\nabla\mathbf{X} + \frac{\mathrm{d}\mathbf{v}}{\mathrm{d}t}\frac{\partial\mathbf{X}}{\mathbf{v}}, \tag{B.10}$$

where $\mathbf{X}$ can be replaced by $\mathbf{x}-\boldsymbol{\rho}$ with $\boldsymbol{\rho} = (\mathbf{b}\times\mathbf{s})/\Omega = \boldsymbol{\rho} = (\mathbf{b}\times\mathbf{v})/\Omega$. Thus, one obtains in cartesian coordinates

$$\begin{aligned}
\mathbf{v}\cdot\nabla\mathbf{X} = v_\alpha(\nabla\mathbf{X})_{\alpha\beta} &= v_\alpha\left(\delta_{\alpha\beta} - \epsilon_{\beta\gamma\delta}s_\delta\left(\frac{1}{\Omega}\frac{\partial b_\gamma}{\partial x_\alpha} - \frac{b_\gamma}{\Omega^2}\frac{\partial\Omega}{\partial x_\alpha}\right)\right)\\
&= \mathbf{v} + \frac{1}{\Omega}\mathbf{v}\times(\mathbf{v}\cdot\nabla\mathbf{b}) + \boldsymbol{\rho}\frac{\mathbf{v}\cdot\nabla B_0}{B_0}
\end{aligned} \tag{B.11}$$

and

$$\begin{aligned}
\left(\frac{\mathrm{d}\mathbf{v}}{\mathrm{d}t}\right)_\alpha\left(\frac{\partial\mathbf{X}}{\partial\mathbf{v}}\right)_{\alpha\beta} &= \left(\frac{q}{m}E_\alpha - \Omega s\hat{\rho}_\alpha + \frac{q}{mc}\epsilon_{\alpha\kappa\lambda}v_\kappa B_{1\lambda}\right)\left(-\frac{1}{\Omega}\epsilon_{\alpha\beta\gamma}b_\gamma\right)\\
&= \mathbf{v}_E - \mathbf{s} - \mathbf{v}\frac{\mathbf{b}\cdot\mathbf{B}_1}{B_0} + \frac{u}{B_0}\mathbf{B}_1.
\end{aligned} \tag{B.12}$$

Combining both of the above results, one obtains Eq. (2.47)

$$\begin{aligned}
\frac{\mathrm{d}\mathbf{X}}{\mathrm{d}t} &= \mathbf{v}_0 + \mathbf{v}_1 \sim (\omega_t + \delta v_t) + \Delta v_t,\\
\mathbf{v}_0 &= \mathbf{u} + \mathbf{v}_{E,0} + \frac{1}{\Omega}\mathbf{v}\times(\mathbf{v}\cdot\nabla)\,\nabla\mathbf{b} + \boldsymbol{\rho}\frac{(\mathbf{v}\cdot\nabla)\,B_0}{B_0},\\
\mathbf{v}_1 &= \mathbf{v}_{E,1} - \mathbf{v}\frac{\mathbf{b}\cdot\mathbf{B}_1}{B_0} + \frac{u}{B_0}\mathbf{B}_1.
\end{aligned} \tag{B.13}$$

The gyrokinetic equation needs the gyroaverages of $\mathrm{d}\mathbf{X}/\mathrm{d}t$, $\mathrm{d}\mu/\mathrm{d}t$ and $\mathrm{d}U/\mathrm{d}t$. Note, that the average of an unperturbed quantity, which varies on a spatial scale much larger than a gyroradius, is the quantity itself plus order δ^2 corrections which are neglected in the current approximation. A potential complication arises from the use of the guiding centre position $\mathbf{X}$ as coordinate in position space because the exact gyroradius vector is calculated at fixed particle position $\mathbf{x}$ while the gyroaverage is carried out at fixed guiding centre. However, for the current approximation the lowest order term in δ of $\boldsymbol{\rho}(\mathbf{X})$ is sufficient. It is given by

$$\boldsymbol{\rho}(\mathbf{X}) = \frac{1}{\Omega(\mathbf{X}}\mathbf{b}(\mathbf{X}) \times \mathbf{s}. \tag{B.14}$$

The average of the time derivative of the particle energy U is simply

$$\frac{\mathrm{d}U}{\mathrm{d}t} = \dot{U} = q\left(\langle\frac{\partial\Phi_1}{\partial t}\rangle - \frac{1}{c}\langle\mathbf{v}\cdot\frac{\partial\mathbf{A}_1}{\partial t}\rangle\right). \tag{B.15}$$

The particle drifts are given by the average $\langle\mathrm{d}\mathbf{X}/\mathrm{d}t\rangle = \langle\mathbf{v}_0 + \mathbf{v}_1\rangle$. The first term of the average of the unperturbed guiding centre velocity is $\langle\mathbf{u}\rangle = \mathbf{u}$, the second is $\langle\mathbf{v}_{E0}\rangle = \mathbf{v}_{E0} + \mathrm{O}(\delta^2)$. The nonvanishing components of the third term in $\langle\mathbf{v}_0\rangle$ are

$$\langle\frac{1}{\Omega}\mathbf{v}\times(\mathbf{v}\cdot\nabla\mathbf{b})\rangle = \frac{u^2}{\Omega}\mathbf{b}\times\boldsymbol{\kappa} + \frac{1}{\Omega}\langle\mathbf{s}\times(\mathbf{s}\cdot\nabla\mathbf{b})\rangle = \frac{u^2}{\Omega}\mathbf{b}\times\boldsymbol{\kappa} + \frac{1}{\Omega}\mathbf{b}(\mathbf{b}\cdot\nabla\times\mathbf{b}), \tag{B.16}$$

where the first term is the curvature drift and $\boldsymbol{\kappa}$ the curvature vector, and the last term, a parallel guiding centre drift, will be neglected against the thermal parallel motion $\mathbf{u}$ (see also [21]). Finally

$$\langle\boldsymbol{\rho}\frac{\mathbf{v}\cdot\nabla B_0}{B_0}\rangle = \frac{\mu}{\Omega m}\mathbf{b}\times\nabla B_0 \tag{B.17}$$

is the ∇B drift. Altogether, one obtains

$$\langle\mathbf{v}_0\rangle = \mathbf{u} + \mathbf{v}_{D0} = \mathbf{u} + \mathbf{v}_{E0} + \frac{1}{\Omega}\mathbf{b}\times\left(\frac{\mu}{m}\nabla B_0 + u^2\boldsymbol{\kappa}\right). \tag{B.18}$$

Since the average $\langle\mathbf{v}_1\rangle$ involves the field components varying on the gyroradius scale, it cannot be simplified further. As an effect of the approximate invariance of μ, the average $\langle\dot{\mu}_0\rangle$ vanishes. To be more explicit, $\langle(q/B_0)\mathbf{s}\cdot\mathbf{E}_0\rangle = 0$ and $\langle -(\mu/B_0)\mathbf{v}\cdot\nabla B_0 - (mu/B_0)\mathbf{s}\cdot(\mathbf{v}\cdot\nabla\mathbf{b})\rangle = 0$. Therefore,

$$\langle\dot{\mu}_0 + \dot{\mu}_1\rangle = \langle\dot{\mu}_1\rangle = \frac{qs}{B_0}\left(\langle\mathbf{s}\cdot\mathbf{E}_1\rangle - \frac{u}{c}\langle\hat{\boldsymbol{\rho}}\cdot\mathbf{B}_1\rangle\right). \tag{B.19}$$

B.2 Some identities in fluid theory

The divergence of the $\mathbf{E}\times\mathbf{B}$ drift can be expressed as

$$\nabla\cdot\mathbf{v}_E = -c\mathbf{E}_\perp\cdot\nabla\times\frac{\mathbf{b}}{B} = c\nabla_\perp\Phi\cdot\nabla\times\frac{\mathbf{b}}{B}. \tag{B.20}$$

The curl of $\mathbf{b}/B$ can then be written as

$$\nabla \times \frac{\mathbf{b}}{B} = \frac{4\pi}{cB^2}\mathbf{j} - \frac{2}{B^4}\nabla_\perp \frac{B^2}{2}, \tag{B.21}$$

where the last perpendicular gradient can be simplified using the equilibrium condition $\mathbf{F}_m = \nabla p$. The Lorentz force $\mathbf{F}_m$ is given by the divergence of the magnetic Maxwell stress tensor,

$$\begin{aligned}\mathbf{F}_m &= -\nabla \cdot \mathbf{T}_m = \frac{1}{4\pi}\nabla \cdot \left(\mathbf{I}\frac{B^2}{2} - \mathbf{BB}\right) \\ &= -\frac{1}{4\pi}\left(\nabla \frac{B^2}{2} - B^2\boldsymbol{\kappa} - \nabla_\parallel \frac{B^2}{2}\right) \\ &= -\frac{1}{4\pi}\left(\nabla_\perp \frac{B^2}{2} - B^2\boldsymbol{\kappa}\right) = \nabla p. \end{aligned} \tag{B.22}$$

Therefore, one obtains

$$-\nabla_\perp \frac{B^2}{2} = 4\pi\nabla p - B^2\boldsymbol{\kappa}. \tag{B.23}$$

Noting that $\nabla p = (1/c)\mathbf{j} \times \mathbf{B}$, one finds that

$$\nabla \times \frac{\mathbf{b}}{B} = \frac{4\pi}{cB^2}\left(\mathbf{j} - \mathbf{j}_\perp\right) + \left(\frac{4\pi\nabla p}{B^2} - 2\boldsymbol{\kappa}\right) \times \frac{\mathbf{b}}{B} = \frac{4\pi}{cB^2}\mathbf{j}_\parallel - (\boldsymbol{\kappa} + \nabla(\ln B)) \times \frac{\mathbf{b}}{B}, \tag{B.24}$$

and therefore

$$\nabla \cdot \mathbf{v}_E = c\frac{\mathbf{b}}{B} \times (\boldsymbol{\kappa} + \nabla(\ln B)) \cdot \nabla_\perp \Phi \equiv -\hat{C}\Phi. \tag{B.25}$$

Since in low β plasmas $\boldsymbol{\kappa} \approx \nabla(\ln B)$, the operator $\hat{C}$ is called curvature operator. The divergence of the particle flux due to curvature and ∇B drifts is found to be

$$\nabla \cdot (n(\mathbf{v}_\kappa + \mathbf{v}_{\nabla B})) \approx \frac{c}{q}\frac{\mathbf{b}}{B} \times (\boldsymbol{\kappa} + \nabla(\ln B)) \cdot \nabla p = -\hat{C}\frac{p}{q}, \tag{B.26}$$

where $p = nT$ is the pressure and the divergence of $(\mathbf{b}/B) \times (\boldsymbol{\kappa} + \nabla(\ln B))$ can be neglected.

Appendix C

Calculations for chapter 3

C.1 Gyrokinetic commutators as divergences

The brackets defined in Eq. (3.32) in Sec. 3.5 can always be written as a divergence. Consider the expression

$$C = a\,(K * b) - b\,(K * a) \tag{C.1}$$

where $a(x)$ and $b(x)$, $K\,(x) = K\,(-x)$ is a symmetric convolution kernel and $*$ indicates the convolution operation. Because of this symmetry one may express equation (C.1) as

$$\partial_z J \equiv C = \partial_z \int\int L\,(z-x, z-y)\,a\,(x)\,b\,(y)\,\mathrm{d}x\,\mathrm{d}y \tag{C.2}$$

with $L\,(x,y) = [\theta\,(x) - \theta\,(y)]\,K\,(x-y)$. For purely harmonic waves $a\,(x)\,, b\,(x) = \Re\,\{(A,B)\exp\,(ikx - i\omega t)\}$, the resulting flux J is given by

$$J = (\partial_z)^{-1}\,\{a,b\}_{\hat{K}} = \Im\,\{A^* B\}\,\partial_k \hat{K}\,(k) \tag{C.3}$$

where $\hat{K}$ is the Fourier transform of K. The application of this theorem to, for instance, the first bracket in Eq. (3.31) yields the corresponding free energy flux

$$J_{\mathrm{FLR}} = \int J_1\,(k_\perp)\,\frac{\mathbf{k}\cdot\mathbf{v}_{\mathrm{d}}}{\tau}\Re\,\{n^*\,(\tau f + F_0 J_0 n)\}\,\mathrm{d}^3 v. \tag{C.4}$$

C.2 Individual Poynting fluxes

Evaluating Eq. (3.26) for circular flux surfaces by using estimates of the up-down symmetric and antisymmetric fluctuation amplitudes (as described in Sec. 3.3.1) the individual Poynting fluxes result up to order $O[k_r^3]$,

$$\left\langle \frac{\boldsymbol{v}_d}{2}\,(n+\tau p_i)^2 \right\rangle = \frac{k_r^3 \phi_0^2}{6\sqrt{6\,(3+5\tau)}}\left[9 + 30\tau + 55\tau^2 + \frac{1}{4q^2}\left(81 + 342\tau + 455\tau^2\right)\right], \tag{C.5}$$

$$\left\langle \frac{5\boldsymbol{v}_d}{4}\,(\tau T_i)^2 \right\rangle = \frac{5\tau^2 k_r^3 \phi_0^2}{3\sqrt{6}\,(3+5\tau)^{3/2}}\left[3 + 20\tau + \frac{\left(81 + 387\tau + 500\tau^2\right)}{4q^2\,(3+5\tau)}\right], \tag{C.6}$$

$$\left\langle \boldsymbol{v}_d \tau v_\parallel^2 \right\rangle = \frac{\tau k_r^3 \phi_0^2 \left(9 + 39\tau + 50\tau^2\right)}{q^2 \sqrt{6} \left(3 + 5\tau\right)^{3/2}} \tag{C.7}$$

$$\left\langle \tau \boldsymbol{v}_d \left[-\frac{\Delta}{2} \left(\alpha c^2 + 2\beta cd + \gamma d^2 \right) + \phi_0 \Delta a + \frac{3}{2} \left(\alpha \left(\nabla c \right)^2 + 2\beta \nabla c \nabla d + \gamma \left(\nabla d \right)^2 \right) - \right.\right.$$
$$\left.\left. - \tau \left(\Delta v_\parallel^2 - 3 \left(\nabla v_\parallel \right)^2 \right) \right] \right\rangle = \left(1 + \frac{1}{4q^2} \right) \frac{11 \tau k_r^3 \phi_0^2 \left(3 + 7\tau\right)}{3\sqrt{6} \left(3 + 5\tau\right)^{1/2}}, \tag{C.8}$$

$$\left\langle - \left(n + \tau p_i\right) \nabla \left(\dot{n} + \tau \dot{p_i} \right) \right\rangle = - \left(1 + \frac{1}{4q^2} \right) \frac{k_r^3 \phi_0^2 \left(3 + 5\tau\right)^{3/2}}{3\sqrt{6}}, \tag{C.9}$$

$$\left\langle -\frac{5}{2} \tau^2 T_i \nabla \dot{T}_i \right\rangle = - \left(1 + \frac{3}{4q^2} \right) \frac{10 \tau^2 k_r^3 \phi_0^2}{3\sqrt{6} \left(3 + 5\tau\right)^{1/2}}, \tag{C.10}$$

$$\left\langle -\tau T_i \nabla \dot{\phi_0} \right\rangle = - \left(1 + \frac{1}{4q^2} \right) \frac{10 \tau^2 k_r^3 \phi_0^2}{3\sqrt{6} \left(3 + 5\tau\right)^{1/2}}, \tag{C.11}$$

$$\left\langle -\tau v_\parallel \nabla \dot{v}_\parallel \right\rangle = - \frac{\tau k_r^3 \phi_0^2 \left(3 + 5\tau\right)^{1/2}}{2\sqrt{6} q^2}. \tag{C.12}$$

For the gyrokinetic framework, Eq. (3.31), the individual fluxes are

$$\left\langle \int \frac{\boldsymbol{v}_d}{\tau} \frac{K^2}{2F_0} \, \mathrm{d}^3 v \right\rangle = \frac{k_r^3 \phi_0^2}{4\sqrt{2} \left(4 + 7\tau\right)^{3/2}} \left[16 + 140\tau + 481\tau^2 + 747\tau^3 + \right.$$
$$\left. + \frac{1}{q^2 \left(4 + 7\tau\right)^2} \left(576 + 6576\tau + 36068\tau^2 + 130144\tau^3 + 317687\tau^4 + 293067\tau^5 \right) \right], \tag{C.13}$$

$$\left\langle \nabla^{-1} \left(- \int \left\{ \frac{\boldsymbol{v}_d}{\tau} \cdot \nabla K, n \right\}_{J_0} \mathrm{d}^3 v \right) \right\rangle = 0, \tag{C.14}$$

$$\left\langle \nabla^{-1} \left(- \int \left\{ \frac{\boldsymbol{v}_\parallel}{\tau} \cdot \nabla \tau f, n \right\}_{J_0} \mathrm{d}^3 v \right) \right\rangle = - \frac{\sqrt{2} \tau k_r^3 \phi_0^2 \left(2 + 5\tau\right)}{q^2 \left(4 + 7\tau\right)^{3/2}}, \tag{C.15}$$

$$\left\langle \nabla^{-1} \left(\int \left\{ \tau f, \frac{\boldsymbol{v}_d}{\tau} \cdot \nabla \phi_0 \right\}_{J_0} \mathrm{d}^3 v \right) \right\rangle = - \frac{\tau^2 k_r^3 \phi_0^2}{2\sqrt{2} \left(4 + 7\tau\right)^{1/2}} \left[13 + \frac{28 + 196\tau + 163\tau^2}{q^2 \left(4 + 7\tau\right)^2} \right], \tag{C.16}$$

$$\left\langle \nabla^{-1} \left(\int \left\{ n F_0, \frac{\boldsymbol{v}_d}{\tau} \cdot \nabla \phi_0 \right\}_{J_0^2} \mathrm{d}^3 v \right) \right\rangle = - \frac{\tau k_r^3 \phi_0^2}{2\sqrt{2} \left(4 + 7\tau\right)^{1/2}} \left[12 + \frac{48 + 168\tau + 60\tau^2}{q^2 \left(4 + 7\tau\right)^2} \right], \tag{C.17}$$

$$\left\langle \nabla^{-1} \left(\frac{1}{2} \left\{ \phi, \dot{\phi} \right\}_{\frac{1-\Gamma_0}{\tau}} \right) - \phi_0 \hat{\chi} \dot{\boldsymbol{E}}_0 \right\rangle = \frac{k_e^3 \phi_0^2}{8\sqrt{2} \left(4 + 7\tau\right)^{1/2}} \times$$
$$\times \left[-16 + 12\tau + 21\tau^2 + \frac{1}{q^2 \left(4 + 7\tau\right)^2} \left(-192 + 656\tau - 252\tau^2 + 612\tau^3 + 483\tau^4 \right) \right]. \tag{C.18}$$

Appendix D

NLET parameters for experimental equilibrium data

Machine	NSTX	AUG	AUG	AUG	AUG	AUG	AUG
Shot #	135042	20787	20787	20787	18813	18813	18813
Time (ms)	232	1000	1000	1000	900	900	900
ρ_{pol}	0.99	0.84	0.91	0.97	0.88	0.97	0.99
R_{ref} (m)	1.507	2.05	2.09	2.13	2.06	2.12	2.14
n_0 (10^{19}m^{-3})	0.75	1.75	1.3	0.7	2.1	1.25	0.9
$T_{e,0}$ (eV)	50	280	140	42	443	167	87
B_T magn. axis (T)	0.43	1.94	1.94	1.94	1.94	1.94	1.94
$B_T(R_{ref})$ (T)	0.29	1.56	1.53	1.50	1.55	1.51	1.50
ρ_{se} (cm)	0.34	0.22	0.16	0.09	0.28	0.18	0.13
L_n (cm)	6	19.2	12.4	2.8	30.7	4.0	2.8
L_T (cm)	2.0	7.8	4.0	2.1	8.5	3.0	1.4
$L_\parallel$ (m)	23.6	26.0	30.0	35.3	25.1	38.9	47.0
$\eta_i = \eta_e$	3.0	2.45	3.13	1.33	3.6	1.33	2.0
s_g	9.1	1.46	1.64	1.98	2.25	4.26	8.34
ϵ_n	0.08	0.19	0.12	0.026	0.30	0.04	0.03
ϵ_v	0.009	0.017	0.012	0.005	0.022	0.006	0.004
α_d	0.82	3.73	1.87	0.73	5.37	2.23	1.11
α_m	0.55	0.07	0.06	0.06	0.08	0.30	0.26
μ	0.36	2.14	0.92	0.34	3.44	2.22	1.09
κ_i	0.005	0.10	0.002	0.001	0.29	0.012	0.002
κ_e	0.017	3.69	0.78	0.047	10.2	0.41	0.087
γ_p	0.05	0.68	0.19	0.015	1.75	0.16	0.049

Table D.1: Parameters used for the calculation of the dimensionless NLET parameters and dimensionless NLET parameters. For a definition see Ref. [14].

Appendix E

List of publications in peer-reviewed journals

Parts of this thesis have been published in peer-reviewed journals in the following articles.

1. R. Hager and K. Hallatschek. Radial Propagation of geodesic acoustic modes. *Physics of Plasmas, 16(7):072503, 2009.*
2. R. Hager and K. Hallatschek. Radial Propagation of geodesic acoustic modes in up-down asymmetric magnetic geometries. *Physics of Plasmas, 17(3):032112, 2010.*
3. S. J. Zweben, R. J. Maqueda, R. Hager, K. Hallatschek, S. M. Kaye, T. Munsat, F. M. Poli, a. L. Roquemore, Y. Sechrest, and D. P. Stotler. Quiet periods in edge turbulence preceding the L-H transition in the National Spherical Torus Experiment. *Physics of Plasmas, 17(10):102502, 2010.*

Bibliography

[1] W. Horton. Drift waves and transport. *Reviews of Modern Physics*, 71(3):735–778, 1999.

[2] A. Hasegawa, C. G. Maclennan, and Y. Kodama. Nonlinear behavior and turbulence spectra of drift waves and Rossby waves. *Physics of Fluids*, 22(11):2122–2129, 1979.

[3] N. Winsor, J. L. Johnson, and J. M. Dawson. Geodesic acoustic waves in hydromagnetic systems. *Physics of Fluids*, 11(11):2448–2450, 1968.

[4] P. W. Terry. Suppression of turbulence and transport by sheared flow. *Reviews of Modern Physics*, 72(1):109–165, 2000.

[5] H. Biglari, P. H. Diamond, and P. W. Terry. Influence of sheared poloidal rotation on edge turbulence. *Physics of Fluids B*, 2(1):1–4, 1990.

[6] T. S. Hahm. Physics behind transport barrier theory and simulations. *Plasma Physics and Controlled Fusion*, 44:A87–A101, 2002.

[7] G. D. Conway, C. Troster, B. Scott, K. Hallatschek, and the ASDEX Upgrade Team. Frequency scaling and localization of geodesic acoustic modes in ASDEX Upgrade. *Plasma Physics and Controlled Fusion*, 50(5):055009, 2008.

[8] J. W. Connor, A. Fasoli, C. Hidalgo, A. Kirk, V. Naulin, A. G. Peeters, and T. Tala. 13th EU-US Transport Task Force Workshop on transport in fusion plasmas. *Nuclear Fusion*, 49:047001, 2009.

[9] D. Reiser and D. Chandra. Plasma currents induced by resonant magnetic field perturbations in tokamaks. *Physics of Plasmas*, 16:042317, 2009.

[10] K. Itoh, S.-I. Itoh, P. H. Diamond, A. Fujisawa, M. Yagi, T. Watari, Y. Nagashima, and A. Fukuyama. Geodesic acoustic eigenmodes. *Plasma Fusion Research*, 1:037, 2006.

[11] K. Hallatschek. Nonlinear three-dimensional flows in magnetized plasmas. *Plasma Physics and Controlled Fusion*, 49(12B):B137–B148, 2007.

[12] R. L. Miller, M. S. Chu, J. M. Greene, Y. R. Lin-Liu, and R. E. Waltz. Noncircular, finite aspect ratio, local equilibrium model. *Physics of Plasmas*, 5(4):973–978, 1998.

[13] S. J. Zweben, R. J. Maqueda, R. Hager, K. Hallatschek, S. M. Kaye, T. Munsat, F. M. Poli, a. L. Roquemore, Y. Sechrest, and D. P. Stotler. Quiet periods in edge turbulence preceding the L-H transition in the National Spherical Torus Experiment. *Physics of Plasmas*, 17(10):102502, 2010.

[14] K. Hallatschek and A. Zeiler. Nonlocal simulation of the transition from ballooning to ion temperature gradient mode turbulence in the tokamak edge. *Physics of Plasmas*, 7(6):2554–2564, 2000.

[15] J. Candy and R. E. Waltz. An eulerian gyrokinetic-Maxwell solver. *Journal of Computational Physics*, 186(2):545 – 581, 2003.

[16] J. R. Lumby. Current systems of the North Atlantic and the North Sea. *Journal of Ecology*, 20(2):314–325, 1932.

[17] V. P. Starr. An essay on the general circulation of the earth's atmosphere. *Journal of Meteorology*, 5(2):39–43, 1947.

[18] E. T. Eady. The cause of the general circulation of the atmosphere. *Centen. Proc. Roy. Meteor. Soc.*, pages 156–172, 1950.

[19] Hsiao-Lan Kuo. Dynamical aspects of the general circulation and the stability of zonal flow. *Tellus*, 3(4):268–284, 1951.

[20] C. C. Porco, R. A. West, A. McEwen, A. D. Del Genio, A. P. Ingersoll, P. Thomas, S. Squyres, L. Dones, C. D. Murray, T. V. Johnson, J. A. Burns, A. Brahic, G. Neukum, J. Veverka, J. M. Barbara, T. Denk, M. Evans, J. J. Ferrier, P. Geissler, P. Helfenstein, T. Roatsch, H. Throop, M. Tiscareno, and A. R. Vasavada. Cassini Imaging of Jupiter's Atmosphere, Satellites, and Rings. *Science*, 299(5612):1541–1547, 2003.

[21] R. D. Hazeltine and J. D. Meiss. *Plasma Confinement*. Dover, Mineola, 1. edition, 2003.

[22] R. J. Goldston and P. H. Rutherford. *Introduction to Plasma Physics*. Taylor and Francis, New York, 1. edition, 1995.

[23] T. S. Hahm. Rotation shear induced fluctuation decorrelation in a toroidal plasma. *Physics of Plasmas*, 1(9):2940–2944, 1994.

[24] T. S. Hahm and K. H. Burrell. Flow shear induced fluctuation suppression in finite aspect ratio shaped tokamak plasma. *Physics of Plasmas*, 2(5):1648–1651, 1995.

[25] T. S. Hahm, M. A. Beer, Z. Lin, G. W. Hammett, W. W. Lee, and W. M. Tang. Shearing rate of time-dependent $E \times B$ flow. *Physics of Plasmas*, 6(3):922–926, 1999.

[26] M. Jakubowski, R. J. Fonck, and G. R. McKee. Observation of coherent sheared turbulence flows in the DIII-D tokamak. *Physical Review Letters*, 89(26):265003, 2002.

[27] G. R. McKee, R. J. Fonck, M. Jakubowski, K. H. Burrell, K. Hallatschek, R. A. Moyer, W. Nevins, D.L. Rudakov, and X. Xu. Observation of radially sheared zonal flows in DIII-D. *Plasma Physics and Controlled Fusion*, 45:A477–A485, 2003.

[28] G. D. Conway, B. Scott, J. Schirmer, M. Reich, A. Kendl, and the ASDEX Upgrade Team. Direct measurement of zonal flows and geodesic acoustic mode oscillations in ASDEX Upgrade using doppler reflectometry. *Plasma Physics and Controlled Fusion*, 47:1165–1185, 2005.

[29] Y. Hamada, A. Nishizawa, T. Ido, T. Watari, M. Kojima, Y. Kawasumi, K. Narihara, K. Toi, and JIPP T-IIU Group. Zonal flows in the geodesic acoustic mode frequency range in the JIPP T-IIU tokamak plasmas. *Nuclear Fusion*, 45:81–88, 2005.

[30] A. V. Melnikov, L. G. Eliseev, A. V. Gudozhnik, S. E. Lysenko, V. A. Mavrin, S. V. Perfilov, L. G. Zimeleva, M. V. Ufimtsev, L. I. Krupnik, and P. M. Schoch. Investigation of the plasma potential oscillations in the range of geodesic acoustic mode frequencies by heavy ion beam probing in tokamaks. *Czechoslovak Journal of Physics*, 55(3):349–360, 2005.

[31] A. Krämer-Flecken, S. Soldatov, H. R. Koslowski, O. Zimmermann, and TEXTOR Team. Properties of geodesic acoustic modes and the relation to density fluctuations. *Physical Review Letters*, 97(04):045006, 2006.

[32] K. J. Zhao, T. Lan, J. Q. Dong, L. W. Yan, W. Y. Hong, C. X. Yu, A. D. Liu, J. Qian, J. Cheng, D. L. Yu, Q. W. Yang, X. T. Ding, Y. Liu, and C. H. Pan. Toroidal symmetry of the geodesic acoustic mode zonal flow in a tokamak plasma. *Physical Review Letters*, 96(25):255004, 2006.

[33] Z. Gao, K. Itoh, H. Sanuki, and J. Q. Dong. Eigenmode analysis of geodesic acoustic modes. *Physics of Plasmas*, 15(7):072511, 2008.

[34] F. Zonca and L. Chen. Radial structures and nonlinear excitation of geodesic acoustic modes. *Europhysics Letters*, 83(3):35001, 2008.

[35] X. Q. Xu, E. Belli, K. Bodi, J. Candy, C. S. Chang, R. H. Cohen, P. Colella, A. M. Dimits, M. R. Dorr, Z. Gao, J. A. Hittinger, S. Ko, S. Krasheninnikov, G. R. McKee, W. M. Nevins, T. D. Rognlien, P. B. Snyder, J. Suh, and M. V. Umansky. Dynamics of kinetic geodesic-acoustic-modes and the radial electric field in tokamak neoclassical plasmas. *Nuclear Fusion*, 49:065023, 2009.

[36] K. Hallatschek and D. Biskamp. Transport control by coherent zonal flows in the core/edge transitional regime. *Physical Review Letters*, 86(7):1223–1226, 2001.

[37] Z. Gao, P. Wang, and H. Sanuki. Plasma shaping effects on the geodesic acoustic mode in toroidally axisymmetric plasmas. *Physics of Plasmas*, 15(7):074502, 2008.

[38] A. Kendl and B. D. Scott. Flux-surface shaping effects on tokamak edge turbulence and flows. *Physics of Plasmas*, 13(1):012504, 2006.

[39] L. Villard, P. Angelino, a. Bottino, R. Hatzky, S. Jolliet, B. F. McMillan, O. Sauter, and T. M. Tran. Plasma shape effects on geodesic acoustic oscillations. *AIP Conference Proceedings*, pages 424–429, 2006.

[40] G. R. McKee, D. K. Gupta, R. J. Fonck, D. J. Schlossberg, M. W. Shafer, and P. Gohil. Structure and scaling properties of the geodesic acoustic mode. *Plasma Physics and Controlled Fusion*, 48(4):S123–S136, 2006.

[41] R. Hager and K. Hallatschek. Radial propagation of geodesic acoustic modes. *Physics of Plasmas*, 16(7):072503, 2009.

[42] R. Hager and K. Hallatschek. Radial propagation of geodesic acoustic modes in up-down asymmetric magnetic geometries. *Physics of Plasmas*, 17:032112, 2010.

[43] T. Watari, Y. Hamada, T. Notake, N. Takeuchi, and K. Itoh. Geodesic acoustic mode oscillation in the low frequency range. *Physics of Plasmas*, 13(6):062504, 2006.

[44] Z. Gao, K. Itoh, H. Sanuki, and J. Q. Dong. Multiple eigenmodes of geodesic acoustic mode in collisionless plasmas. *Physics of Plasmas*, 13(10):100702, 2006.

[45] J. W. Connor and H. R. Wilson. A review of theories of the L-H transition. *Plasma Physics and Controlled Fusion*, 42:R1–R74, 2000.

[46] W. Dorland, F. Jenko, M. Kotschenreuther, and B. N. Rogers. Electron temperature gradient turbulence. *Physical Review Letters*, 85(26):5579–5582, Dec 2000.

[47] G. D. Conway, C. Angioni, E. Poli, F. Ryter, P. Sauter, B. Scott, T. Happel, J. Vicente, and the ASDEX Upgrade Team. Behaviour of mean and oscillating $\mathbf{E}\times\mathbf{B}$ plasma flows and turbulence interactions during confinement mode transitions. *IAEA Conference Proceedings*, pages EXC/7–1, 2010.

[48] G. D. Conway and the ASDEX Upgrade Team. Amplitude behaviour of geodesic acoustic modes in the ASDEX Upgrade tokamak. *Plasma Physics and Controlled Fusion*, 50(8):085005, 2008.

[49] D. G. Swanson. *Plasma Kinetic Theory*. CRC Press, 2008.

[50] A. J. Brizard and T. S. Hahm. Foundations of nonlinear gyrokinetic theory. *Reviews of Modern Physics*, 79(2):421–468, 2007.

[51] A. Zeiler. *Tokamak Edge Turbulence*. habilitation thesis, Max-Planck-Institut für Plasmaphysik, 1999. http://edoc.mpg.de/display.epl?mode=do&id=271253.

[52] S. I. Braginskii. Transport processes in a plasma. *Reviews of Plasma Physics*, 1:205–311, 1965.

[53] K. H. Spatschek. *Theoretische Plasmaphysik*. Teubner, Stuttgart, 1. edition, 1990.

[54] M. N. Rosenbluth and F. L. Hinton. Poloidal flow driven by ion-temperature-gradient turbulence in tokamaks. *Physical Review Letters*, 80(4):724–727, 1998.

[55] K. Hallatschek. Thermodynamic potential in local turbulence simulations. *Physical Review Letters*, 93(12):125001, 2004.

[56] R. E. Waltz and C. Holland. Numerical experiments on the drift wave–zonal flow paradigm for nonlinear saturation. *Physics of Plasmas*, 15(12):122503, 2008.

[57] E. A. Frieman and Liu Chen. Nonlinear gyrokinetic equations for low-frequency electromagnetic waves in general plasma equilibria. *Physics of Fluids*, 25(3):502–508, 1982.

[58] H. Sugama and T.-H. Watanabe. Collisionless damping of zonal flows in helical systems. *Physics of Plasmas*, 13:012501, 2006.

[59] A. J. Redd, A. H. Kritz, G. Bateman, G. Rewoldt, and W. M. Tang. Drift mode growth rates and associated transport. *Physics of Plasmas*, 6(4):1162–1167, 1999.

[60] A. M. Dimits, B. I. Cohen, N. Mattor, W. M. Nevins, D. E. Shumaker, S. E. Parker, and C. Kim. Simulation of ion temperature gradient turbulence in tokamaks. *Nuclear Fusion*, 40(3Y):661–666, 2000.

[61] K. Hallatschek. Turbulent saturation of tokamak-core zonal flows. *Physical Review Letters*, 93(6):065001, 2004.

[62] K. Hallatschek and R. Hager. Control of turbulent transport by gams. *IAEA Conference Proceedings*, page THC/P804, 2010.

[63] K. Itoh and S.-I. Itoh. Excitation of geodesic acoustic mode in toroidal plasmas. *Plasma Physics and Controlled Fusion*, 47:451–458, 2005.

[64] A. Krämer-Flecken, S. Soldatov, D. Reiser, M. Kantor, and H. R. Koslowski. Investigation of geodesic acoustic modes and related zonal flows at TEXTOR. *Plasma Physics and Controlled Fusion*, 51:015001, 2009.

[65] L. L. Lao, J. R. Ferron, R. J. Groebner, W. Howl, H. St. John, E. J. Strait, and T. S. Taylor. Equilibrium analysis of current profiles in tokamaks. *Nuclear Fusion*, 30(6):1035, 1990.

[66] P. J. Mc Carthy. Analytical solutions to the Grad–Shafranov equation for tokamak equilibrium with dissimilar source functions. *Physics of Plasmas*, 6(9):3554–3560, 1999.

[67] J.L. Luxon. A design retrospective of the DIII-D tokamak. *Nuclear Fusion*, 42(5):614–633, 2002.